FINITE ELEMENT STUDIES OF ORTHOGONAL MACHINING OF ALUMINUM ALLOY A2024-T351

by

Jaimeen P. Patel

A thesis submitted to the faculty of
The University of North Carolina at Charlotte
in partial fulfillment of the requirements
for the degree of Master of Science in
Mechanical Engineering

Charlotte

2018

Approved by:

_____
Dr. Harish P. Cherukuri

_____
Dr. Tony Schmitz

_____
Dr. Miguel Pando

ABSTRACT

JAIMEEN P. PATEL. Finite Element Studies of Orthogonal Machining of Aluminum Alloy A2024-T351. (Under the direction of DR. HARISH P. CHERUKURI)

In this work, a new machining model using the commercial finite element software ABAQUS is developed. The model regards material separation, chip serration and breakage as ductile fracture processes where energy is required to form new surfaces. The main hypothesis is that the critical energy release rate for chip separation is different from the critical energy release rate for chip serration. The Johnson-Cook damage model is used to account for damage initiation in the workpiece material. The damage evolution leading to chip separation, serration and possible breakage is assumed to be governed by Hillerborg's fracture model. Two separate forms of Hillerborg fracture model are investigated and the appropriate forms for chip separation and serration are identified. A unique feature of the model is that the threshold value for the critical energy release rate for chip separation is determined from the existing experimental results. In addition, the model also uses a novel stress-based method for accounting for the frictional characteristics of the tool-chip interface.

The model is verified and validated using the data available in the open literature. Various parametric studies involving cutting speed, uncut chip thickness and rake angles have been carried out to study their effect on cutting force, mechanical and thermal fields, and the chip morphologies. Our results indicate that the model is robust and the numerical predictions are in agreement with the trends observed in experiments.

ACKNOWLEDGEMENTS

I would like to express my sincere gratitude to my advisor Dr. Harish P. Cherukuri for his continuous support and inspiration throughout my Master's degree program and research at UNC-Charlotte. His tutelage, mentoring, motivation and encouragement helped me to strive and bring the best out if my abilities.

I would also like to thank Dr. Tony Schmitz and Dr. Miguel Pando for serving on my thesis committee.

I would like to specially thank Dr. Tony Schmitz for his valuable inputs and critical review of my initial results.

I would like to thank my parents and family for their valuable support and motivation throughout my career. I am really grateful to Mihir Patel, Hardik Patel and Prexa Patel for their support and encouragement. It would not have been possible to pursue higher education and achieve this avenue with out their encouragement.

I am really grateful to Hardik Shah who always guided me to take right decision in my professional and personal life.

I would like to thank my friends Harsh Patel, Nakul Tannu, Aneesh Nabar and Dr. Mohammed Hassan for their valuable guidance during my masters.

Finally I am grateful to each and every member of out research group for their critical reviews throughout my research.

DEDICATION

With immense happiness, I dedicate my master's thesis to my family Pravinbhai Patel, Bhavanaben Patel, Yagna Patel and Urvil Patel.

TABLE OF CONTENTS

LIST OF FIGURES

LIST OF TABLES

LIST OF ABBREVIATIONS

α	Rake angle
$\bar{\epsilon}$	Equivalent plastic strain
$\bar{\epsilon}_d$	Equivalent plastic strain at onset of damage
$\bar{\epsilon}_f$	Equivalent plastic strain at fracture
$\bar{\sigma_d}$	effective stress at onset of damage
$\bar{\sigma}$	Effective mises stress or flow stress
$\bar{u}$	Equivalent plastic displacement
$\bar{u}_f$	Equivalent plastic displacement at failure
$\dot{\bar{\epsilon}}$	Equivalent plastic strain rate
$\dot{\epsilon_0}$	Reference strain rate taken as 1 s^{-1}.
ϕ	Shear plane angle
A	Initial yield stress
a_c	Uncut chip thickness or feed
a_p	Depth of cut
a_{ch}	Chip thickness
B	Hardening modulus
C	coefficient dependent on strain rate
F_c	Cutting force component
F_t	Thrust force component

G_c Critical energy release rate or fracture toughness

G_f^{sep} Threshold for chip separation criterion

G_f^{serr} Threshold for chip fracture criterion

K_{Ic} Mode-I fracture toughness

K_{IIc} Mode-II fracture toughness

m Thermal softening coefficient

n Work hardening coefficient

p Hydrostatic stress (pressure)

T Current Temperature

T_{melt} Melting Temperature of the material

T_{trans} Transition temperature

CHAPTER 1: INTRODUCTION

Understanding the mechanics of material removal processes and chip formation during machining are active areas of research. Although a significant progress has been made during the past twenty years in understanding the mechanics of material removal processes, the mechanics of material separation is not very well understood due to the fact that the material behavior under the conditions that exist during machining (high stain-rates and high temperatures) is not very well understood. This work is a small attempt to analyze orthogonal machining of ductile metals using finite element method.

Machining processes can be broadly categorized into two types namely, orthogonal machining and oblique machining. In orthogonal machining process, the cutting edge and face are perpendicular to direction of machining whereas in oblique cutting process, they are at some angle w.r.t the cutting direction. In this work, simulation of orthogonal machining of Aluminum alloy A2024-T351 using a tungsten carbide tool is presented. Orthogonal machining can be modelled as a two dimensional plane strain problem since the normal and shear strains in the lateral direction can be assumed to be zero. Such a condition arises because the uncut chip thickness a_c is very small compared to the width of cut w.

Figure 1.1 shows a schematic diagram of orthogonal machining represented as 2D plane strain model. V_c is the horizontal cutting speed of the tool with rake angle α. The tool rake angle can be positive or negative as shown in figure. a_c represents uncut chip thickness where as $a_c h$ is the thickness of chip after material separation. In machining, shearing takes place along three different shear zones as shown in fig. 1.2. ϕ is the shear plane angle corresponding to the orientation of primary shear zone

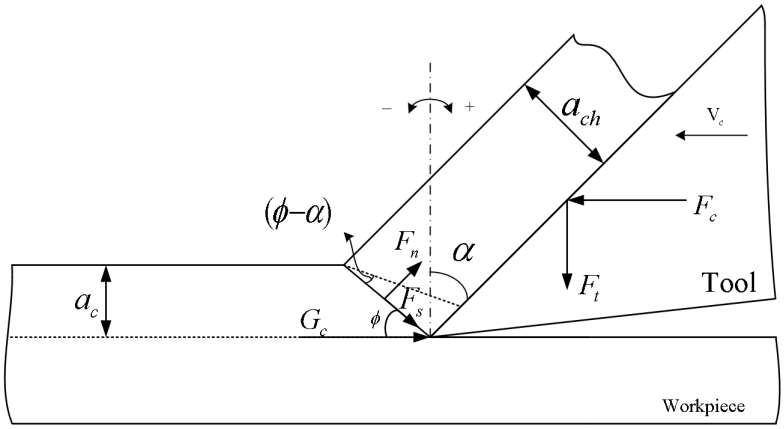

Figure 1.1: Schematic diagram of 2D (plane strain) orthogonal machining

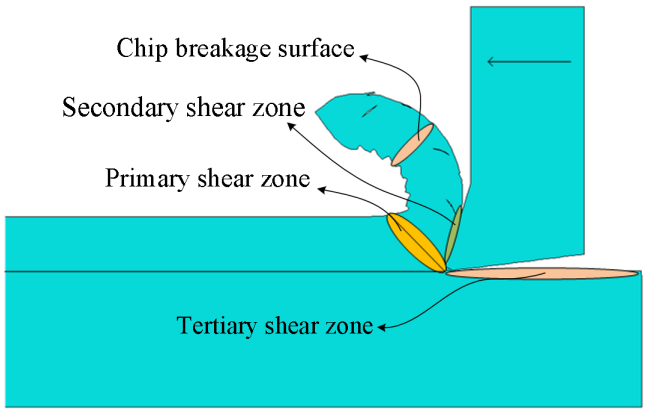

Figure 1.2: Primary, secondary and tertiary shear zones

w.r.t the horizontal direction as shown in fig. 1.1. The shearing in primary shear zone is particularly due to plastic work where as in secondary and tertiary shear zones, it is generally due to friction.

The chip shape during machining depends on various cutting parameters such as tool rake angle α, cutting speed V_c and uncut chip thickness a_c. In addition, the chip shape also depends on friction at tool-chip interface, work hardening and thermal softening of the workpiece material and other mechanical and thermal properties of the cutting tool and workpiece. The role of mechanics in machining is to show how these factors directly influence cutting force F_c, tool wear, surface finish, shear plane

angle, temperature rise and field variables such as stress and strain in primary and secondary shear zones. Chip morphology studies is important to understand the mechanics of metal cutting for various cutting parameters. For example, the chip micro-photographs presented by Ye et. al. in [3] shows that chip shape changes from continuous or smooth chips to serrated chips to discontinuous chips with increase in cutting speed V_c.

There are four main types of chip shapes:

1. Continuous chips
2. built up edge (BUE) chips
3. Serrated chips
4. Discontinuous chips

Finite element method is a very powerful technique for studying the mechanics of machining. In this work, a new machining model that draws upon the fracture mechanics concepts for material separation is presented. The main objective is to consider machining as a problem of ductile fracture with new energy-based criteria for forming new surfaces during material separation and chip serration or breakage. In addition, a new model that accounts for inhomogeneous frictional characteristics between the tool and workpiece is also proposed. The machining model including these new proposals are implemented in ABAQUS/EXPLICIT, verified, and validated. Following this, various parametric studies are conducted.

CHAPTER 2: LITERATURE REVIEW

Prior to 1940s, a craft approach was used for process planning of metal cutting performance. The approach was based on making modifications to experimental result obtained in workshops. There was no significant attempt to relate performance of metal cutting to mechanics explained by stress, strain, strain rate, localized micro-structure and temperature encountered during cutting. Cocquilhat [4] was the first one to measure the work required to remove a given volume of material by drilling. Eventually researchers started looking into mechanics of metal cutting. Time [5] showed that chip formation ahead of cutting tool is a consequence of shearing, whereas, Tresca [6] argued that the chip formation in metal cutting is produced by compression in workpiece material ahead of the tool. Tresca [7] considered visco-plastic analysis of machining and said that minute observation was inevitable for designing optimum tool and determining uncut chip thickness. He showed that material had larger plastic deformation in finer cuts as compared to larger cuts. As per Markopoulos [6], there is no contradiction between Tresca and Time. Zvorykin [8] calculated force and energy required for cutting in Tresca's model and provided a physical explanation by calculating the shear angle. Mallock [9] analyzed the action of cutting tools from theoretical point of view and quantified the work expended in cutting and tool-workpiece friction. He argued that chip formation from metal was a result of shearing and that friction between tool and chip was very important in determining the deformation in chip. However, he did not consider the visco-plastic behaviour as considered by Tresca and hence his equations gave incorrect results. Tresca was also clear that heat is generated due to plastic work, but he considered only forging process for calculating heat, where he assumed that 94% of the plastic

work is converted to heat and related it to the work of Joule. All the research and work done in 20^{th} century or before were subjected to some serious criticism, because the models were proposed without an extended knowledge of laws that govern strains in bodies subjected to large forces [9]. However, these models provided an important ground work for all the successive progress and research in subsequent years. These analytical models were intended to aim at determining cutting force requirement without carrying out any experiments. Based on derived cutting forces, other parameters could be derived to study tool wear and surface finish. A major challenge faced during development of these analytical models was to determine relationship between shear plane angle, the rake angle and coefficient of friction.

2.1 Analytical Models

A significant amount of work has been dedicated towards developing analytical models of orthogonal metal cutting in the literature. Numerous researchers have put efforts to develop models which can provide a basic understanding of mechanics near cutting tool tip and interaction between tool and chip. Piispanen [10] and Ernst-Merchant [11], made some significant contributions in applying mechanics for analysis of cutting operation. Simple models were developed using lot of assumptions to understand the machining processes. Later, plasticity, friction and fracture mechanics were eventually considered with a considerable amount of simplification to develop analytical models. Explanations for the chip formation and chip morphology under various cutting conditions or parameters has been one of the main focuses in all the developed models.

2.1.1 Single Shear Plane Models

Piispanen [10] introduced a well known "deck of cards" model to show how material shears into chip from the bulk. He considered straight chip and an infinite contact with the tool in his analysis. Moreover, the shear stress in shear plane was considered to

be the flow stress of the material. Later, Ernst and Merchant [11] proposed a single shear plane model according to which the shearing of chip from the bulk material occurs over a narrow shear zone. Ernst-Merchant model related the shear plane angle ϕ with the rake angle α and coefficient of friction μ (or friction angle γ_0). Unlike Piispanen's model, the model developed by Ernst and Merchant did not assume infinite contact between tool and chip. Merchant [12] carried out an analysis of chip geometry and force system in case of orthogonal cutting and derived equations in terms of mechanical quantities. He considered that energy required to separate chip from bulk material (energy required to form new surfaces) is of the order of j/m^2 which is negligible as compared to energy spent in plastic work and friction which are of the order KJ/m^2. The Merchant Circle force analysis assumes chip to be in rigid body equilibrium and the forces are considered to be acting at tool tip. These forces are decomposed into respective components to determine plastic work in shear plane and frictional work along tool chip interface. Merchant's models used minimum energy principle to determine shear plane angle. Merchant argued that shear plane angle ϕ adjusts itself such that the total work rate or cutting energy is minimum [11]. The relation between shear plane angle ϕ with rake angle α and coefficient of friction μ or friction angle γ_0 derived from single plane shear model is given by

$$\phi = \frac{1}{2}(\pi/2 + \alpha - \gamma_0) \tag{2.1}$$

Ernst-Merchant model gave good correlation with experimental results for machining of polymers and some steel such as SAE4340, but the results deviated for majority of steel. Moreover, they did not consider the effect of strain hardening, strain rate hardening and temperature in the analysis. Later, Merchant attempted to modify this model to consider material dependent constant C in the expression for shear

plane angle given by

$$\phi = \frac{1}{2}(C + \alpha - \gamma_0) \tag{2.2}$$

Kobayashi and Thomsen [13] developed a new angle relationship from energy consideration in Ernst-Merchant solution to find new parameters, effectiveness η and machinability factor ξ. These parameters gave a better understanding of machining process to predict machining forces and power more accurately. The literature has many other analytical models ([14], [15], [16]) that were developed based on experiments and attempted to modify and improve overly simplified Merchant model.

2.1.2 Slip Line Field Models

Slip-line field theory was a popular approach to analyze machining. Slip line fields consider plane-strain loading conditions and consist of two orthogonal directions along which shear stresses are maximum. These directions vary at every point. A slip line is a curve to which the maximum shear stress is tangential along its length and a complete set of such lines gives slip-line field. Lee and Shaffer were the first researchers to develop slip-line field models for chip formation [14]. They assumed a triangular slip-line field in the region adjacent to the cutting edge along with a rigidly perfect plastic material. It should be noted that they neglected thermal and inertial effects. The shear-plane angle determined from this model is given by

$$\phi = \pi/4 + \alpha - \gamma_0. \tag{2.3}$$

Slip-line field models were then on modified by other researchers [17] who considered curved boundaries for slip lines. However, different chip shapes and thickness resulted from same cutting conditions and parameters from these models. Dewhurst [18] constructed slip line field using a matrix method described by Dewhurst and Collins

in [19] to show that solution for orthogonal machining is not unique and it can be influenced by the initial cutting conditions and random disturbances occurring during machining.

Oxley [20] developed predictive machining theory which was known as Oxley's theory, for predicting cutting forces, cutting temperatures and stresses in orthogonal cutting. He used experimental flow fields to model an appropriate slip line field which was then altered to satisfy boundary conditions for velocity and force. These slip line fields were then used to determine shear angle, cutting forces, power and temperature using a value of flow stress for the work material that was independent of hydrostatic stress. Oxley's theory requires thermal properties (specific heat and thermal conductivity) of work material, flow stress data of the work material that depends on strain, strain-rate and temperatures, tool geometry and cutting conditions.

2.1.3 Parallel sided shear zone models

Oxley and Welsh [21] analyzed orthogonal metal cutting process by introducing parallel sided shear zone model (also known as thick shear zone model) for chip formation. They extrapolated material test results such as conventional compression, torsion and indentation to very large strain, strain rate and temperature pertaining to metal chip formation to consider the effect of strain hardening, strain rate hardening and thermal softening. They calculated shear angle from fundamental properties of material and specific cutting conditions which gave a qualitative explanation for the main trends observed in metal cutting. Most shear plane models assumed that the shear stress in the shear plane is uniform, moreover a constant or average coefficient of friction at the tool chip interface was considered along with neglecting strain hardening effects. However, in Oxley's model, based on experimental data, it was assumed that thickness of primary shear zone was one tenth of the shear zone length and plastic flow patterns were observed in this zone. The variation in velocity with respect to position in primary and secondary shear zone gave strain rates and integrating these

strain rates along the streamlines of the flow resulted in strains. This approach by Oxley became very popular among the researchers. Usui in [22] carried out a three dimensional analysis using Oxley's model which also included secondary cutting edge and nose radius effects. The shear angle according to Oxley's shear zone model is

$$\tan\phi = \frac{\cos\alpha}{\frac{a_{ch}}{a_c} - \sin\alpha} \tag{2.4}$$

where a_c is the uncut chip thickness and a_{ch} is the chip thickness obtained after machining.

2.1.4 Limitations of Analytical models

1. The results from single plane shear model did not match experimental results and hence it was criticized by researchers. Ernst-Merchant model gives incorrect velocity and force diagrams, however, they are still being used due to its simplicity

2. Single shear models predicted extremely high shear strains which were contradictory with material testing results. The material model being rigid-perfectly plastic accounts for inaccurate resistance from work-pieced material. Moreover, other assumptions such as the perfectly sharp cutting edge of the tool, neglecting the effects of strain hardening, strain rate hardening and temperature deviated the analytical results from experimental results.

3. Non-uniqueness of the solution was a significant limitation of the slip line field models resulting mainly due to assuming rigid plastic material model for work-piece. Moreover, they had poor correlation with experimental results with no strain hardening considered. Furthermore, these models do not take into account material separation.

4. Although the parallel-sided shear zone models are in good agreement with ex-

perimental results but the main drawback with these models is that they are very complex to apply and they also require stress and strain data at various strain rates and temperatures encountered in machining which is cumbersome and difficult to determine.

2.2 Finite Element Modelling of machining processes

Finite Element Method (FEM) provides a good approximate solution to continuum and damage mechanics problem using its numerical discretization scheme. It is an appropriate technique to study machining process due to its capability to model various material model and complex boundary conditions and interactions. In addition, a detailed output from the analysis of machining could be obtained from machining simulations such as flow stress, equivalent plastic strain, temperature, chip morphology, shear angle, chip thickness, cutting and thrust forces and residual stress. It is difficult to obtain such an elaborate output from analytical analysis of machining. A large collection literature is available which witnesses the development of machining models using Finite Element Analysis [23] and [24]. Using Numerical method has been proved to be a more promising approach with the development of more sophisticated finite element codes and robust hardware which are capable of doing parallel computing. One of the first FE (Finite Element) model was developed by Klamecki [25]. This was a three dimensional model, but it was limited to initial chip formation. During the same time Tay et al. [26] obtained temperature distribution for orthogonal machining for continuous chip formation by solving a steady state two dimensional energy equation using FEM. Shirakashi and Usui [27] developed a computational method called Iterative convergence Method (ICM) in which a small crack propagating in front of the tool tip was used for chip separation. This was one of the first model which used two dimensional plane strain formulation and simulated chip formation.

2.2.1 Finite Element Formulation

Researchers generally used either Eulerian, total/updated Lagrangian, or Arbitrary Lagrangian Eulerian (ALE) formulations to model and simulate machining operation using finite elements. In early years, development of finite element models using Eulerial finite element formulation was more popular. However, later on total/updated Lagrangian models became first choice for the researchers [6].

2.2.1.1 Eulerian Formulation

In Eulerian formulation, the mesh (nodes) is fixed spatially and material convects through the mesh. The finite elements do not undergo distortion due to material motion consequently the challenges for mesh distortion are removed. However, With this approach of modeling machining, the initial chip geometry without stress, strain, shear angle and contact conditions must be known a priori. These parameters and chip geometry could be determined as initial state using experimental results or assumptions.

Tay et al. [26] used Eulerian formulation for modeling orthogonal machining, similarly Akarca et al. [28] used Eulerian formulation and SPH. Strenkowski and Moon [29] used Eulerian finite element model which incorporated procedure for predicting the chip geometry and contact length. Strenkowski and Carroll [30] used Eulerial formulation and viscoplastic material model to simulate chip formation. As mentioned earlier, in this approach they used, the boundaries of chip must be known in advance and the grid was adjusted according to the chip geometry. Childs and Maekawa [31] conducted finite element analysis where they considered an initial straight chip shape defined entirely by its shear plane angle, the uncut chip thickness (feed) and tool and rake angle. The work material was assumed to obey Prandtl-Reuss flow rules and the von-mises yield criterion. The analysis gave a good prediction of tool thrust force, tool temperature and wear prediction but the cutting forces were not agreeing (lower)

with the experimental results.

2.2.1.2 Total/Updated Lagrangian Formulation

In Lagrangian formulation, the integration points are coincident with material points and the mesh deforms along with the material. Here Boundary nodes remains on material boundary and hence application of boundary conditions or defining contact interaction becomes simple. Moreover, it is possible to model segmented chips besides continuous chips. In total Lagrangian, [32] formulation, the weak form involves integrals over reference configuration and derivatives are taken with respect to the material coordinates. Whereas in updated Lagrangian formulation, the integrals in weak form are taken with respect to the deformed configuration and the derivatives are taken with respect to spatial coordinates. Both Total Lagrangian and updated Lagrangian are essentially represent same mechanical behavior (Lagrangian) and can be transformed to each other.

However, while using Lagrangian finite element formulation, severe mesh distortion is encountered. Some researchers use pre-distorted techniques [33] or re-meshing techniques [34] to overcome mesh distortion issues. In addition, a physical chip separation criterion is required in order to model chip formation from bulk. The chip formation simulation done by Klamecki [25] used Lagrangian formulation. This approach is more popular among the researchers because that it allows chip formation from incipient. However, determining a physical chip separation criterion is still a critical research area and so far no criterion has been universally accepted. Shih developed and implemented plane strain Lagrangian finite element formulation to simulate orthogonal metal cutting for continuous chip formation. He considered a material model that included elasticity, viscoplasticity, thermal effects as well as high strain and strain rate effects. His contact model had stick-slip contact formulation and presented results for stress, strain, temperature and strain rates in primary and secondary shear zones. He also compared residual stress distribution with experi-

mental results obtained from X-ray diffraction measurements. Other researchers who used similar approach was used by Usui and Shirakashi in [35] where they used Lagrangian formulation for their FE model. Lin and Lin [36] used a coupled temperature displacement model where they considered elastic-plastic material model and a chip separation criterion based on strain energy density to model machining process. They used Lagrangian finite element method to simulate metal cutting and finite difference method was adopted to determine temperature distribution. Strenkowski and Carroll [37] used updated Lagrangian formulation and plane strain condition to model orthogonal cutting operation along with introducing a friction model and adiabatic heating model. Similar model was used to for simulating chip formation in orthogonal metal cutting by Komvopoulos and Erpenbeck [38]. Ueda and Manabe [39] used a three dimensional model of work material for analyzing oblique cutting using rigid plastic finite element method based on Lagrangian formulation. Zhang and Bagchi [40] used incremental plasticity theory and Mises stress potential function to form constitutive relationship. Other researchers who used Lagrangian formulation are Shih et. al. [41], Sashara and Shirakashi [42], etc. Marusich and Ortiz [34] developed an updated Lagrangian model of high speed orthogonal machining where they employed continuous re-meshing and adaptive meshing to overcome the difficulties of element distortion. Similarly [43] Ceretti et. al., investigated plane strain cutting problem in DEFORM 2D by employing implicit Lagrangian code and subroutines for re-meshing and smoothing and also employed a chip separation criterion based on damage accumulation.

2.2.1.3 Arbitrary Lagrangian and Eulerian Formulation

The Eulerian and Lagrangian formulations have their own advantages and disadvantages. Therefore a hybrid technique, Arbitrary Lagrangian Eulerian (ALE) formulation, which combine the advantages of Eulerian and Lagrangian method has been developed [32]. In this method user can define a part of the mesh to have La-

grangian formulation and a part can have Eulerian formulation, such that advantages of both the methods are utilized. In machining simulations with ALE formulation, the boundary nodes and nodes at the interface locations remains coincident with the material points and hence a Lagrangian formulation is considered for them. Where as the internal nodes are modeled with Eulerian formulation in order to overcome severe element distortion in primary and secondary shear zones. Olovsson et. al. [44] developed one of the first ALE models for simulation of orthogonal cutting. They used a special 'crack element' for simulating orthogonal machining process. They considered an elastic-plastic material model with isotropic hardening and Coulomb's friction model for contact between chip and tool.

Rakotomalala et. al. [45] also used ALE for simulating orthogonal machining process. Movahhedy et. al. [46] used ALE formulation without any node separation criterion to model chip formation in orthogonal cutting. Ozel and Zeren [47] ALE formulation to simulate plastic flow around the round cutting edge of the cutting tool. They used Johnson-Cook Constitutive model for work material and used Johnson-Cook Damage model for simulating segmented and discontinuous chip formation in AISI 4340 steel along with a contact model based on coulomb's model to consider effect of friction at tool-chip interface. Arrazola and Ozel [48] used FE models with ALE fully coupled thermal-stress analysis of steel AISI 4340 to study effects of FE modeling with different ALE techniques and also investigated the effect of limiting shear stress at tool workpiece contact on frictional conditions. No chip separation criterion was involved in their model.

2.2.1.4 Advantages and drawbacks of Eulerian, Lagrangian and ALE formulation

1. Although Eulerian formulation do not require any remeshing or they do not encounter mesh distortion issues, the major drawback is that it requires initial chip geometry without stress, strain, shear angle and contact conditions must be known a priori. These parameters and chip geometry could be determined

as initial states using experimental results or assumptions. The treatment of constitutive equations and updates is complicated due to the convection of materials through the elements. Moreover, treatment of moving boundaries and interfaces is difficult with Eulerian formulation [32]. The strains are calculated by integrating strain rates over streamlines, hence this cannot be used to model discontinuous chips.

2. When using Eulerian or ALE formulation to model chip formation in machining, they do not consider the mechanics of fracture involved in cutting which is an established fact [49]. Moreover, modeling discontinuous chips is also not possible by using these formulation.

3. ALE and Eulerian formulations uses remapping of the state variables which may be inaccurate and leading to incorrect results. In addition, the need of complete remeshing in ALE increases computational cost considerably.

4. Total/Updated Lagrangian formulations can simulate chip breakage and can model chip separation without knowing the initial chip shape which is a major advantage in this formulation. This formulation gives more physical results for chip thickness and shape, it can even model discontinuous or segmented chips, the results highly depend on the chip separation criterion used and the physics associated to it. mesh distortion is another major challenge faced with this method and using adaptive meshing to overcome this challenge at the expense of computational costs. However, results with adaptive meshing are still controversial and needs further study [6].

5. However, if an appropriate chip separation criterion, which reflects the physics and mechanics of chip formation accurately, is used in Lagrangian finite element formulation accurate results for analysis of machining process could be achieved.

However, mesh distortion should be controlled with various techniques such as hour glass control.

2.2.2 Constitutive Models

Constitutive models are very crucial for achieving accurate results from finite element simulation of machining processes. A lot of work has been dedicated in literature, pertaining to using an appropriate constitutive model such as rigid-plastic, elastoplastic, rigid-viscoplastic and elastic-viscoplastic [50]. Different models considered in literature have varying degree of accuracy according to the dependence of flow stress considered on various physical parameters. Researchers modified Oxley's theory to develop models with various constitutive equations to study cutting force, temperature, stresses in primary and secondary shear zones. It is an established fact that the flow stress in machining is a function of strain ϵ, strain rate $\dot{\epsilon}$ and temperature T.

2.2.2.1 Oxley's Constitutive Model

Macgregor and Fisher [51] considered power law for hardening of work material of the form shown in equation 2.5, where the constants σ_1 and n depended on velocity modified temperature as given in equation 2.6. They used the model originally developed by Oxley in [20].

$$\bar{\sigma} = \sigma_1 \bar{\epsilon}^n \tag{2.5}$$

$$T_{mod} = T[1 - 0.09log(\dot{\bar{\epsilon}})] \tag{2.6}$$

2.2.2.2 Usui, Shirakashi and Maekawa's Constitutive Model

Shirakashi et. al. in [52] and Usui et. al. in [53] were amongst the first researcher to use a constitutive model in which flow stress was function of strain ϵ, strain rate $\dot{\epsilon}$

and temperature T given by:

$$\bar{\sigma} = B\left[\frac{\dot{\bar{\epsilon}}}{1000}\right]^{M} e^{-kT}\left[\frac{\dot{\bar{\epsilon}}}{1000}\right]^{m}\left[\int_{Path} e^{-kT}/N\left[\frac{\dot{\bar{\epsilon}}}{1000}\right]^{-\frac{m}{N}} d\bar{\epsilon}\right] \tag{2.7}$$

Here B is the strength factor, M strain rate sensitivity and n is strain hardening index and all these parameters are function of temperature T whereas k and m are constants. The last tern in Equation 2.7 considers history of strain and temperature in relation to strain rate [6].

Zerilli and Armstrong [54] considered dislocation theory and derived two constitutive model, one for Face centered cubic (FCC) lattice and another for Body centered cubic (BCC) lattice materials as given by

$$\bar{\sigma} = C_0 + C_2\bar{\epsilon}^{(1/2)}\exp[-C_3T + C_4Tln(\dot{\bar{\epsilon}})] \tag{2.8}$$

$$\bar{\sigma} = C_0 + C_1\exp[-C_3T + C_4Tln(\dot{\bar{\epsilon}})] + C_5\bar{\epsilon}^{n} \tag{2.9}$$

In Above equations, T is the absolute temperature, C_1 to C_5 and n are material constants derived from experiments such as SHPB test. C_0 is an additional component of stress which considers original dislocation density and solute of flow stress. Zerilli and Armstrong considered flow stress being function of strain such that strain is not affected by temperature and strain rate in BCC material lattice and in contrary for FCC, temperature and strain rate do affect strain. They considered strain hardening coefficient n to be fixed value for all FCC materials. however, some researchers considered a more general value n for FCC materials

The most popular constitutive model in Machining is Johnson Cook Constitutive model given by Equation 2.10. Huang and Liang [55] modified Oxley's predictive machining theory by analytically modeling the thermal behaviors of the primary and the secondary moving heat sources which gave the temperature distribution in primary

and secondary shear zones. They applied modified Johnson cook Constitutive model to their theory to represent work material property as a function of strain, strain rate and temperature. Adibi-Sedeh et al. [56] also used Johnson cook constitutive model to modify Oxley's machining theory for predicting cutting forces and temperatures. They concluded that Johnson cook constitutive model performed best in prediction of cutting forces. Özel and Zeren [57] modified Oxley's machining theory and developed a methodology to determine flow stress at machining regimes and friction characteristics at the tool-chip interface from orthogonal cutting experiments and applying Johnson Cook constitutive model. Karpat and Özel [58] modeled heat intensity at secondary as non-uniform by utilizing modifications done by Özel and Zeren in [57] to Oxley's machining theory.

$$\bar{\sigma} = (A + B\bar{\epsilon}^n)\Big[1 + C\ln\Big(\frac{\dot{\bar{\epsilon}}}{\dot{\epsilon}_0}\Big)\Big]\Big[1 - \bar{T}^m\Big] \tag{2.10}$$

here,

$$\bar{T} = \begin{cases} 0, & T < T_{trans} \\ \dfrac{T - T_{trans}}{T_{melt} - T_{trans}}, & T_{trans} < T < T_{melt} \\ 1, & T > T_{melt} \end{cases} \tag{2.11}$$

In above Equation, A, B, C and m are material constants that depend on the material and are determined from SHPB tests. FEM results are sensitive to the value of constants selected for this constitutive model [59]. These constants are derived from experiments hence, appropriate experimental procedure and setup strongly affects their value for different materials.

2.2.3 Chip Separation Criteria

In order to consider Lagrangian finite element formulation, various chip separation criterion proposed by researchers can be divided into two categories: Geometrical and Physical. A detailed evaluation and analysis of various chip separation criterion has been carried out by Huang and Black in [60] and Zhang in [61].

2.2.4 Geometrical Chip Separation Criterion

A geometrical criterion was first developed by Usui and Shirakashi [35]. A typical example of geometrical chip separation criterion in machining simulations is using a predefined parting line where separate nodes of 'upper' and 'lower' part of the workpiece is coincident and constrained to move together. The geometrical criterion is based on some defined distance between the tool tip and nearest node ahead of it and the nodes are separated when this distance becomes less than a particular threshold value. After separation, one node becomes part of generated chip and the other remains on the open surface of machined work material. such a criterion was used by Komvopoulos and Erpenbeck [38]. Their analysis showed that the critical distance or threshold distance must be selected carefully so that numerical instability may could be avoided. They observed that a sufficient distance between the overlapping nodes and tool tip was required to overcome convergence and distortion issues. The determination of distance threshold, in their analysis, was based on trial and error method. Similarly geometrical criterion were used by other researchers (such as Shih et. al. [41] and Shih [33]) with various modification to reduce numerical instability and achieve more accurate results. Zhang and Bagchi [40] showed that the threshold value of geometric criterion should be 0.1 to 0.3 times the element characteristic length. Another geometrical chip separation criterion used by Zhang and Bagchi in [62] is based on using 2-nodes link element to simulate chip separation. The chip and workpiece were connected by these link elements along a predefined line and as

the distance between the tool tip and leading nodes becomes equal to or less that a defined threshold distance, these link elements would be separated one by one to form chip. However, in their paper, Zang and Bagchi discussed that actual physics of chip formation was still not well understood.

2.2.4.1 Physical Chip Separation Criterion

It is important to consider a good chip separation criterion that reflects physics and mechanics of machining and chip formation. For this purpose, a physical chip separation criterion based on some physical quantity is more appropriate than using geometrical criterion. Various researchers considered different physical quantities for chip separation criterion: Iwata Osakada and Terasaka [63] considered a criterion based on ductile fracture that considered stress history. Strenkowski and Carroll [37] used an updated Lagrangian formulation for plane strain condition in FE model of orthogonal cutting and considered chip separation criterion based on effective (equivalent) plastic strain at the node closest to cutting edge. Mitchum [64] developed a procedure to determine the magnitude of chip separation criterion based on effective plastic strain. Lin and Lin [36] considered a Thermo-elastic-plastic material model for simulating orthogonal cutting and used a chip separation criterion based on the critical value of the strain energy density.

As compared to geometrical criterion the physical criterion have more reliable results in literature. Moreover, the criterion could be determined using some physical quantity that drives chip formation in machining process and its value for various materials and machining parameters could be determined using experimental set up.

Huang and Black [60] and Zhang [61] did a detail analysis and study of various geometrical and physical chip separation criterion which is summarized below. A major disadvantage of all these chip separation criterion is that they are defined over a predefined parting line of nodes in front of tool tip. This is unreasonable because in real machining, the material separation does not occur along a straight

path. Moreover, during the simulation the parting line may be pushed out of position during the course of deformation and the targeted nodes upon which the defined criterion is matched, would not be positioned in front of tool tip.

1. Distance (Geometrical) criterion: The main disadvantage of using a geometry based criterion is that it is not based on physics and mechanics of chip formation. Ideally, in machining there is no physical gap between the crack tip (point from where chip separates from work material) and tool tip. Hence, if critical distance criterion is employed, the minimum threshold value for node separation should be zero or extremely small. However, using zero or extremely small value leads to numerical instability or element distortion at tool tip. Moreover, it was found that the elements within the chips distorted uniformly but the elements at the bottom of the chip distorted badly when the chip came into contact with the tool. Consequently, the maximum value of equivalent plastic strain occurred at the bottom of the chip. In addition it was observed that the maximum shear stress increased during beginning of the cutting and then reached a stable value. A major issue was also encountered when the criterion value was greater than zero, the first element ahead of tool tip was separated even before the tool began to move. Hence, the geometrical criterion did not prove to be very accurate to simulate beginning of cutting and cutting various materials at different cutting parameters.

2. Effective plastic strain criterion: Effective plastic strain is a mechanics quantity which reflects certain physical inherence of the material deformation during chip formation. However, clearly it is not the only quantity upon which material separation and chip formation depends. Strenkowski and Carroll [37], concluded that the variation in chip geometry, tool forces and mean shear stress on shear plane were insignificant for effective plastic strain at the range of 0.25 to 1.00.

However, the residual stress in the machined surface of workpiece became larger when the criterion value was increased. Zhang [61] observed that the value of effective plastic strain at a particular node in front of tool tip (at the instance of separation) keeps varying significantly as the tool advances further. Even during stable cutting conditions, the value of effective plastic strain changes as the cutting speed, cutting depth or rake angle changes. Thus to attain a reliable separation criterion for all cutting conditions, effective plastic strain must be coupled as a variable with some other mechanical or physical quantities such as strain rate, stress triaxiality and temperature. A chip separation criterion based on only effective plastic strain lacked the generality for machining simulations of a given material.

3. Strain energy density criterion: The strain energy density in an element can be expressed as:

$$\frac{dW}{dV} = \int_0^{\epsilon_{ij}} \sigma_{ij} d\epsilon_{ij} \tag{2.12}$$

for plane strain condition: the strain energy density in a given element is given by:

$$\frac{dW}{dV} = \int_0^{\epsilon_{xx}} \sigma_{xx} d\epsilon_{xx} + \int_0^{\epsilon_{yy}} \sigma_{yy} d\epsilon_{yy} + \int_0^{\epsilon_{xy}} \sigma_{xy} d\epsilon_{xy} \tag{2.13}$$

Lin et. al. [36] used a chip separation criterion based on energy point of view in simulation of chip formation. They considered that strain energy density dW/dV, is calculated at the nodes on an anticipated path along which the tool tip moves. Similar to critical distance criterion, they considered that as the value of strain energy density on the node just ahead of tool tip exceeds the

value of critical strain energy density, the node gets separated and becomes part of the chip. They even concluded that the value of critical strain energy density remains constant for different depths of cut for a given material. However, even in this approach by Lin. et.al [36], a predefined path was described for chip formation, which is not practical. In addition, Zhang [61] showed that the conclusion made by Lin et. al. about constant value of critical strain energy density criterion at different depth of cut (for a given material) was incorrect. Moreover, Zhang showed that, for a given material, the threshold value of strain energy density criterion decreased with increase of rake angle of cutting tool and velocity but increased with increasing depth of cut. In a way he showed the tendencies of strain energy density criterion is similar to effective plastic strain criterion and that both of them are not universal.

4. Stress based ductile fracture criterion: Iwata et. al. [63] Combined rigid-plastic finite element method with a ductile fracture criterion which was considered to be affected by stress and strain history. They considered that the ductile fracture strain is critically affected by stress history along with final stress state and the criterion which takes into account stress history is given by

$$\int_0^{\bar{\epsilon_f}} (\bar{\epsilon} + b_1\sigma_m + b_2)d\bar{\epsilon} = b_3 \tag{2.14}$$

Here, the constants b_1, b_2 and b_3 are given as metallurgical properties. This method gave a good correlation with experimental results for distribution of strain rate, stress and equivalent plastic strain, along with thickness and curl of the chip. They also show to have predicted location for fracture in chip. However, the model did not capture properly, the frictional condition and could not

capture temperature in primary and secondary shear zones at all. A major issue in this method was that the experimental set up required for determining the constants in Eqn. (2.14) was very complicated. Moreover, the modeling required a mesh for trial model and an initial estimate for deformed chip thickness. In trial model, the flow stress is uniformly distributed and the chip is supposed to leave the tool surface at some appropriate point. Based on the velocity field calculated from FEM trial model, the point from where the chip leaves tool is modified based on tool pressure and normal velocity component to generate new contour of chip and its mesh. The equivalent strain is calculated by integrating strain rates along the stream lines (generated based on velocity field) and the flow stress in an element was considered to be function of average equivalent strain of the element. After convergence, the occurrence of fracture over the stream lines was checked based on the ductile fracture criterion. This approach was not able to generate complete chip formation and was quite complicated. It was not possible to capture various chip morphology based in this method.

5. Cockroft and Latham damage criterion [65]: Ceretti et. al. [43] after considering several damage criterion in [66] used Cockroft and Latham damage criterion to model segmented chip formation. This was the first approach to use a damage criterion for chip formation using element deletion technique. They simulated continuous chip formation using plastic flow around the tool tip and for simulating segmented chip the damage criterion and element deletion based on that was employed.

   The Cockroft and Latham damage criterion is expressed as:

$$C_i = \int_0^{\epsilon_f} \bar{\sigma}\Big(\frac{\sigma^*}{\bar{\sigma}}\Big) d\bar{\epsilon} \tag{2.15}$$

Here, C_i is the critical damage value given by uniaxial tensile test, ϵ_f is the strain at failure, $\bar{\epsilon}$ is effective strain, $\bar{\sigma}$ is effective stress and σ^* is the maximum stress. The criterion predicts material damage when critical value of C_i is exceeded.

Ceretti et. al. [67] combined Cockroft and Latham damage criterion with criterion based on effective stress to optimize material frature in the simulation of orthogonal cutting. They defined two critical values C_i and $\bar{\sigma}_{max}$, the damage was evaluated for each element in the work piece and the elements were deleted when both the damage values were satisfied. The results obtained in their study predicted chip shapes and influence of cutting conditions on chip shapes. they also predicted cutting force and other parameters quite accurately. However, for some conditions such as negative rake angle, the damage criterion considered did not agree with the experimental results and they needed to consider 10 times smaller value for Cockroft and Latham damage criterion. They also concluded in future work that in order to predict fracture in cutting more accurately, it was necessary to determine critical value for fracture criterion by considering strain rate and temperature as well.

Using effective plastic strain and strain energy density as chip separation criterion was considered as an important avenue in Finite Element analysis of machining operation, as these criterion were more physical and were based on material property. However, since they were not universal and for each cutting condition, a different value of criterion was needed to be determined and employed. A damage criterion which is a function of equivalent plastic strain, strain rate and temperature is an appropriate approach for indicating material failure. In addition it is important that the chip separation criterion considers some process which triggers damage initiation and then damage evolution by stiffness degradation of material as in case of ductile material, the damage does not occur as a result of catastrophic failure. Coupling Johnson cook constitutive model which is quite popular for modeling machining problem with

Johnson cook damage model to evaluate damage initiation and evolution, is an appropriate approach and has been proved to be more accurate and robust as compared to other models and approached discussed earlier in this paper. The chip formation is modeled by element deletion based on critical value of fracture energy G_f.

2.3 Fracture energy view in machining: Atkin's model

Early research in analyzing machining models considered plastic work in primary shear zone and friction work at tool-workpiece interface but ignored the energy required to form new surfaces during chip separation and chip serration. MC Shaw in his research in [68] studied whether, the energy associated with chip momentum changes and that with formation of new surfaces associated with chip separation needed to be considered as significant component of total work associated with cutting or not. However, similar to his fellow researchers during that period he concluded that energy required to form new surfaces in machining was of the order J/m^2 and accepted the earlier argument that it is negligible to plastic work and frictional work. However, Atkins showed in [69], that in terms of ductile fracture mechanics, much greater values of energy required to form new surfaces of the order KJ/m^2 are observed in machining. He showed that when energy required to form new surfaces, (which is referred as fracture energy or fracture toughness in this work), is considered in Ernst-Merchant analysis, many of experimental observations for which traditional analyses had no meaning now makes sense and matches with the experimental data. The shear plane angle becomes material dependent based on this approach. Atkins showed that considering machining as a ductile fracture problem, there is a complete plastic collapse due to which chip formation occurs. Atkins also showed in his work [69], that when critical strain energy density (critical plastic work/volume) or critical Von-Mises strain is employed, the separation work/volume may be converted to work/area by multiplying size of element to which separation criterion is employed and it is of order KJ/m^2. Hence, it is important to take into account the energy required to generate

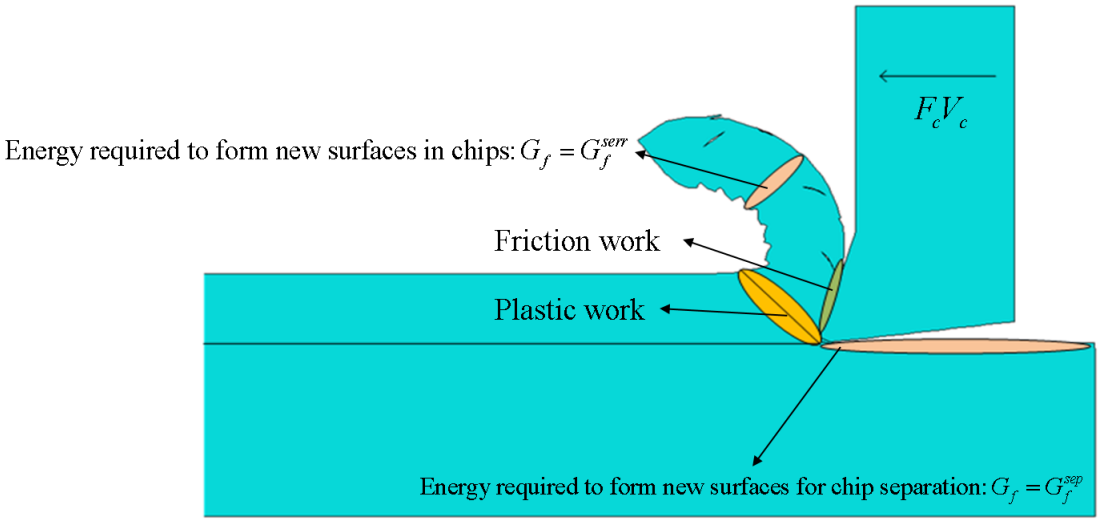

Figure 2.1: Energy balance in Atkins model

new surfaces in machining analysis. The energy required to generate new surfaces or fracture energy can be effectively expressed by fracture toughness (or critical energy release rate). However, measurement of fracture toughness is still a challenging problem for materials having high fracture toughness and low yield stress which leads to crack blunting in conventional test causing difficulties in material separation [70].

The total external work provided by cutting force component F_c is divided into three main portions or components and considering an energy balance of the system:

$$F_cV = (\tau_y\gamma)(a_cwV) + [F_c\sec(\beta-\alpha)\sin\beta]\frac{V\sin\phi}{\cos(\phi-\alpha)} + G_cwV \tag{2.16}$$

In Equation. 2.16, β is the friction angle given by $tan\beta = \mu$ and G_c is the specific fracture energy or energy per unit area required to form new surfaces. G_c can also be considered as fracture toughness of the material which is defined as critical energy release rate from fracture mechanics. The three components of the external work from Equation. 2.16 are as follows:

1. Plastic work dissipated along primary shear zone.

$$U_{plastic} = (\tau_y \gamma)(a_c w V) \tag{2.17}$$

2. Friction work dissipated along tool-workpiece interactions.

$$U_{friction} = [F_c \sec(\beta - \alpha) \sin \beta] \frac{V \sin \phi}{\cos(\phi - \alpha)} \tag{2.18}$$

3. Energy required to form new surfaces ahead of tool tip.

$$U_{friction} = G_c w V \tag{2.19}$$

The shear strain is given by

$$\gamma = \cot \phi + \tan(\phi - \alpha) = \frac{\cos(\alpha)}{\cos(\phi - \alpha) \sin \phi} \tag{2.20}$$

using γ from Equation 2.20, Equation. 2.16 can be written as:

$$\frac{F_c}{w \tau_y a_c} = \frac{\cos(\beta - \alpha)}{\sin \phi \cos(\phi + \beta - \alpha)} \left[1 + \frac{G_c \cos(\alpha - \phi) \sin \phi}{\tau_y a_c \cos \alpha} \right] \tag{2.21}$$

The second term in square brackets in Equation. 2.21 comes from considering energy required to create new surfaces. In a case, that term is omitted, the Equation. 2.21 reduces to force-balance equation from Ernst Merchant theory. Merchant proposed that during machining of any material, the shear plane angle, ϕ adjusted itself such that the total external work rate or F_c is minimum given by:

$$\phi = (\pi/4) - (1/2)(\beta - \alpha) \tag{2.22}$$

As per Merchant's theory, the subjected to different β, the Equation. 2.22 should work for all materials irrespective of their properties. However, for most ductile materials, experimental results for shear angle ϕ was below the ones predicted by Merchant's model. His model worked only for brittle materials where lumps of material were knocked out in experiments. Atkins showed in [69] that Merchant's line of attach for considering minimization of work rate was rather appropriate, but his calculated results deviated from experimental results because he did not considered energy required to form new surfaces. For brittle materials, the fracture toughness being low, as compared to ductile materials, hence without considering fracture energy in his model, Merchant achieved good results for brittle materials.

In Atkin's model, he determined the shear angle ϕ with similar approach of work minimization. Differentiating Equation. 2.21 and setting it to zero for least F_c following expression is obtained:

$$\begin{aligned}\left[1-\frac{\sin\beta\sin\phi}{\cos(\beta-\alpha)\cos(\phi-\alpha)}\right]\left[\frac{1}{\cos^2(\phi-\alpha)}-\frac{1}{\sin^2\phi}\right]=\\ -[\cot\phi+\tan(\phi-\alpha)+Z]\left[\frac{\sin\beta}{\cos(\beta-\alpha)}\left\{\frac{\cos\phi}{\cos(\phi-\alpha)}+\frac{\sin\phi\sin(\phi-\alpha)}{\cos^2(\phi-\alpha)}\right]\right.\end{aligned} \tag{2.23}$$

In the Equation. 2.23, Z is a dimensionless parameter which is material dependent given by:

$$Z=\frac{G_c}{\tau_y a_c} \tag{2.24}$$

The shear angle ϕ is calculated by solving Equation. 2.23 for ϕ, from which it is evident that due to parameter Z, involved in expression, when energy required for creating new surfaces is considered in the model, the shear plane angle ϕ becomes

material dependent. Equation. 2.21 can be reformulated as:

$$F_c = (\frac{\tau_y w \gamma}{Q}) a_c + \frac{G_c w}{Q} \tag{2.25}$$

In the equation. 2.25, Q is the friction correction factor given by:

$$Q = \left[1 - \frac{(\sin\beta \sin\phi)}{\cos(\beta - \alpha)\cos(\phi - \alpha)} \right] \tag{2.26}$$

In Equation. 2.25, at large enough uncut chip thickness a_c, it was found by Atkins in [69] that shear plane angle ϕ is constant and the shear strain γ is also constant for a given rake angle α. As such coefficient of friction is not constant in along the rake face in machining, however, for the sake of simplicity considering an average coefficient of friction μ make friction angle β to be also constant, in that case Equation. 2.25 becomes linear when cutting force F_c is plotted against uncut chip thickness a_c. The value of energy required to create new surfaces or fracture energy ahead of the tool tip can be determined from the Y-intercept of the curve. A wide range of cutting experiments for a given material would include machining test at various uncut chip thickness and accurately measuring the cutting force data corresponding to each uncut chip thickness. An algorithm from this data to measure fracture toughness or energy required to form new surfaces in machining can be determined by the algorithm described in [69].

Considering specific cutting pressure, from Equation. 2.25:

$$\frac{F_c}{w a_c} = \frac{\tau_y \gamma}{Q} + \frac{R}{Q}\left(\frac{1}{a_c}\right) = \frac{\tau_y}{Q}(\gamma + Z) \tag{2.27}$$

Atkins also showed in [69] that at very small uncut chip thickness a_c, the shear

strain γ increases, the value of Z becomes greater than threshold limit of 0.1, the overall specific cutting pressure increases remarkably resulting into "size effects" in machining.

It is very well appreciated that Atkin's model is a very robust and effective method to predict fracture toughness of materials using machining tests. However, it requires establishing friction angle β from cutting force data and initial determination of Q, the friction correction factor for given rake angle α and friction angle β. Moreover, it requires to determine various values of dimensionless parameter Z for a given material and find optimum value of shear plane angle ϕ. Further, determining fracture toughness G_c from here is an iterative process and needs to establish correct Z by matching the intercept and slope of analytical model with the experimental plots. for the purpose of this work and with the limited cutting force and other raw test data available, using Atkin's model might become difficult. Patel et. al. [71] proposed another method which is essentially based on Atkin's model, but a simpler approach to determine fracture toughness G_c using machining experiments.

CHAPTER 3: FINITE ELEMENT MODELING

The major challenges faced during finite element modeling of metal cutting are determination of an appropriate constitutive model for material response, criterion for chip separation from the bulk and an appropriate contact formulation for accurately modeling tool-chip interaction. In this work, a finite element model based on Johnson-Cook constitutive model is used simulating in analyzing orthogonal machining of Aluminum alloy A2024-T351. The tool chip interaction is based on Zorev's stick-slip contact formulation. However, unlike conventional approaches where an average coefficient of friction is used, in this work the slip zone in Zorev's model is formulated with stress based friction model. Chip separation and serration are modeled considering them as a phenomenon resulting from damage and fracture of materials.

Orthogonal machining is simulated by solving a fully coupled thermal - structural and dynamic finite element problem in Abaqus/Explicit. Ali et. al. [72] compared the results of 4 different finite element software packages i.e AdvantEdge, Abaqus/Explicit, Deform2D and Forg to simulate machining process of Titanium alloy Ti-6Al-4V. They concluded that the finite element code Abaqus/Explicit gave better results as compared to other codes.

3.1 Finite element formulation

An updated Lagrangian finite element formulation available in Abaqus is used to solve fully coupled thermo-visco-elasto-platic problem for simulating orthogonal machining of A2024-T351. The updated Lagrangian formulation is expressed in terms of Eulerian measures of stress and strain in which the derivatives and integrals are

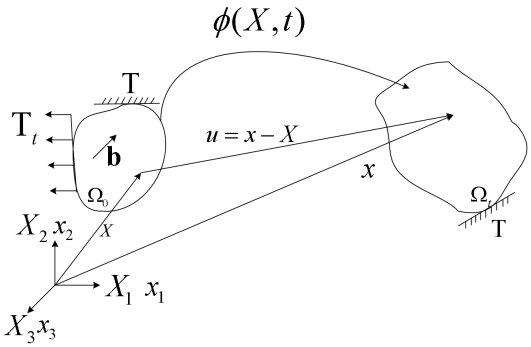

Figure 3.1: Material and spatial configuration of a body deforming due to applied load

taken with respect to spatial or current coordinates x (see fig. 3.1). [32]

3.1.1 Governing equation and weak form for dynamic structural problem

The governing equation for a dynamic structural problem is given by following generalized momentum balance,

$$\frac{\partial \sigma_{ji}}{\partial x_j} + \rho b_i = \rho \dot{v}_i \tag{3.1}$$

The boundary conditions are given by

$$n_j \sigma_{ji} = t_i \quad \text{on} \quad T_{t_i} \quad \text{and} \quad v_i = \bar{v}_i \quad on \quad T_{v_i} \tag{3.2}$$

The weak form of the governing equation is given by principle of virtual power:

$$\int_\Omega \frac{\partial(\delta v_i)}{\partial x_j} \sigma_{ji} d\Omega - \int_\Omega \delta v_i \rho b_i d\Omega - \sum_{i=1}^{n_{SD}} \int_{T_{t_i}} \delta v_i \bar{t}_i dT + \int_\Omega \delta v_i \rho \dot{v}_i d\Omega = 0 \tag{3.3}$$

Here, n_{SD} is 2 for a two dimensional problem and 3 for three dimensional problem. δv_i is the test function also known as virtual velocity. Following is the physical

interpretation of each term in the weak form

$$\text{Virtual internal power}: \quad \delta P^{int} = \int_\Omega \frac{\partial(\delta v_i)}{\partial x_j}\sigma_{ji} d\Omega = \int_\Omega \delta D_{ji}\sigma_{ji} d\Omega \tag{3.4}$$

$$\text{Virtual external power}: \quad \delta P^{ext} = \int_\Omega \delta v_i \rho b_i d\Omega + \sum_{i=1}^{n_{SD}} \int_{T_{t_i}} \delta v_i \bar{t}_i dT \tag{3.5}$$

$$\text{Virtual inertial or kinetic power}: \quad \delta P^{kin} = \int_\Omega \delta v_i \rho \dot{v}_i d\Omega \tag{3.6}$$

Here, the velocity gradient is given by:

$$L_{ij} = v_{i,j} = \frac{\partial[v_{iI}(t)N_I(X)]}{\partial x_j} = v_{iI}\frac{\partial N_I}{\partial x_j} = v_{iI}N_{I,j} \tag{3.7}$$

The velocity gradient L_{ij}, has two parts: The symmetric part known as the rate of deformation tensor $\mathbf{D}$ and its components are given by $D_{ij} = \frac{1}{2}(L_{ij} + L_{ji})$ where as the asymmetric part known as the spin tensor $\mathbf{W}$ and its components are given by $W_{ij} = \frac{1}{2}(L_{ij} - L_{ji})$.

3.1.1.1 Finite element approximation

The current domain Ω is discretized into into Ω_e elements such that the nodal coordinates are given by x_{iI}. Here, node number $I = 1$ to n_N and i corresponds to the components such that $i = 2$ for two dimension space and $i = 3$ for three dimension space.

In Lagrangian formulation, motion $x(X, t)$ is approximated using shape function $N(X)$. For a node with position vector x_I, the motion is approximated by:

$$x_i(X, t) = N_I(X)x_{iI}(t) \tag{3.8}$$

considering a node having initial position X_J, the position is given by:

$$x_i(X_J, t) = N_I(X_J)x_{iI}(t) = \delta_{IJ}x_{iI}(t) = x_{iJ}(t); \quad \text{Because} \quad N_I(X_J) = \delta_{IJ} \tag{3.9}$$

Equation 3.9 indicates that in an updated Lagrangian formulation, the node J always corresponds to material point X_J. In other words, in Lagrangian mesh, the nodes remains coincident with the material points.

The displacement field is approximated by

$$u_i(X,t) = x_i(X,t) - X_i = u_{iI}(t)N_I(X) \tag{3.10}$$

The velocity is calculated by taking material time derivative of the displacement and since shape functions are constant in time, it is given by

$$v_i(X,t) = \frac{\partial u_i(X,t)}{\partial t} = \dot{u}_{iI}(t)N_I(X) = v_{iI}(t)N_I(X) \tag{3.11}$$

Accelerations are similarly given by material time derivatives of velocities

$$a_i(X,t) = \ddot{u}_{iI}(t)N_I(X) = \dot{v}_{iI}(t)N_I(X) \tag{3.12}$$

Discrete finite element equations are formed by substituting equation 3.11 in equation 3.3. The virtual velocities must vanish wherever the velocities are prescribed i.e. $\delta v_i = 0$ on T_{v_i} (from the definition of test space for δv_i). The virtual nodal velocities for nodes not on T_{v_i} are arbitrary and hence can be isolated on LHS and taken to the denominator on RHS. The discrete finite element equations are therefore given by:

$$\int_\Omega \frac{\partial N_I}{\partial x_j}\sigma_{ji}d\Omega - \int_\Omega N_I\rho b_i d\Omega - \sum_{i=1}^{n_{SD}}\int_{T_{t_i}} N_I\bar{t}_i dT + \int_\Omega N_I\rho\dot{v}_i d\Omega = 0 \quad ; \quad \forall(I,i) \notin T_{v_i} \tag{3.13}$$

Finite elements are usually developed with shape functions expressed in terms of master or parent element coordinates (ξ, ζ) (for 2D elements). For further details on this the reader is directed to [32]. Substituting eqn. 3.12 in eqn. 3.13, we have

$$\int_{\Omega} \frac{\partial N_I}{\partial x_j} \sigma_{ji} d\Omega - \int_{\Omega} N_I \rho b_i d\Omega - \sum_{i=1}^{n_{SD}} \int_{T_{t_i}} N_I \bar{t}_i dT + \dot{v}_{iJ} \int_{\Omega} \rho N_I N_J d\Omega = 0 \quad ; \quad \forall (I,i) \notin T_{v_i} \tag{3.14}$$

It is more convenient to define each term in equation 3.14 based on their following physical interpretation.

$$\text{Internal nodal forces} : f_{iI}^{int} = \int_{\Omega} \frac{\partial N_{iI}}{\partial x_j} \sigma_{ji} d\Omega = \int_{\Omega} B_{Ij} \sigma_{ji} d\Omega; \text{where} \quad B_{jI} = \frac{\partial N_{iI}}{\partial x_j} \tag{3.15}$$

The equation 3.15 represents stresses in a body.

$$\text{External nodal forces} : f_{iI}^{ext} = \int_{\Omega} N_I \rho b_i d\Omega + \int_{T_{t_i}} N_I \bar{t}_i dT \tag{3.16}$$

$$\text{Inertial (or kinetic) nodal forces} : f_{iI}^{kin} = \dot{v}_{iJ} \int_{\Omega} \rho N_I N_J d\Omega \tag{3.17}$$

The equation 3.17 is convenient to define as a product of mass matrix and nodal accelerations. the mass matrix is defined as

$$M_{ijIJ} = \delta_{ij} \int_{\Omega} \rho N_I N_J d\Omega \tag{3.18}$$

The inertial nodal forces are then given by

$$\text{Inertial (or kinetic) nodal forces} : f_{iI}^{kin} = M_{ijIJ} \dot{v}_{jJ} \tag{3.19}$$

Finally, the discrete finite element equations or also known as semi-discrete FE equations, where they are discretized only in space is given by:

$$\text{Equation of motion (semi-discrete)} : M_{ijIJ}\dot{v}_{jJ} + f_{iI}^{int} = f_{iI}^{ext} \tag{3.20}$$

3.1.2 Finite element formulation for Transient thermal problem

The semi - discrete finite element equation for heat transfer is given by

$$C_{ij}\dot{\theta}_j + K_{ij}\theta_j = q_i \tag{3.21}$$

Heat Capacity matrix

$$C_{ab} = \int_{B_t} \rho c N_a N_b dV \tag{3.22}$$

here, c = heat capacity and ρ = Current mass density.

Heat Conductivity matrix

$$K_{ab} = \int_{B_t} k N_{a,i} N_{b,i} dV \tag{3.23}$$

Here, k is the thermal conductivity of the material.

In machining there are two sources of heat generation: a). Heat generated due to plastic work. b). Heat generated due to friction at tool - chip interface. The Heat source array is given by:

$$q_a = \int_{B_t} s N_a dV - \int_{\partial B_t} h^f N_a dS \tag{3.24}$$

where as heat generated due to plastic work is given by s which is distributed as heat

source

$$\dot{s} = \eta \sigma_{ij} \dot{\epsilon}^{p}_{ij} \tag{3.25}$$

here for heat generated due to friction on surface is given by h^f

$$\dot{h}^f = f^f \eta^f \tau \dot{\gamma} \tag{3.26}$$

3.1.3 Explicit solver: Central difference method

The central difference method is one of the most popular of explicit methods used in computational mechanics. The Abaqus/Explicit solver is also based on this method which is second order accurate in time i.e. the truncation error is of the order Δt^2 in displacements. The equation 3.20 is semi-discrete form of finite element equations which is discretized only in space. In explicit method, these equations are discretized in time and solved using central difference method. Consider t_e be the time of simulation, the time is disctretized from $0 \leqslant t \leqslant t_e$ using time step Δt^n, where $n = 1, 2, 3...n_{TS}$ is the number of increments. The central difference formula for velocity is given by:

$$\dot{d_i}^{n+1/2} = v_i^{n+1/2} = \frac{d_i^{n+1} - d_i^n}{t^{n+1} - t^n} = \frac{1}{\Delta t^{n+1/2}} (d_i^{n+1} - d_i^n) \tag{3.27}$$

For a known velocity the displacement is given by

$$d_i{}^{n+1} = d_i^n + \Delta t^{n+1/2} v_i^{n+1/2} \tag{3.28}$$

Considering time integration of the equation of motion 3.20 at time step n in matrix notation. For a known velocity the displacement is given by

$$\mathbf{M}\mathbf{a}^n = \mathbf{f}^n = \mathbf{f}^{ext}(\mathbf{d}^n, t^n) - \mathbf{f}^{int}(\mathbf{d}^n, t^n) \tag{3.29}$$

The mass matrix is computed from eqn. 3.18. For a problem with a linear damping force $\mathbf{f}^{damp} = \mathbf{C}^{damp}\mathbf{v}$, the accelerations are computed as

1. Acceleration: $\mathbf{a}^n = \mathbf{M}^{-1}(\mathbf{f}^n - \mathbf{C}^{damp}\mathbf{v})$
2. Time update: $t^{n+1} = t^n + \Delta t^{n+1/2}; t^{n+1/2} = 1/2(t^n + t^{n+1})$
3. First partial velocity : $\mathbf{v}^{n+1/2} = \mathbf{v}^n + (t^{n+1/2} - t^n)\mathbf{a}^n$
4. Enforcing boundary condition on node I on T_{v_i}: $v_{iI}^{n+1/2} = \bar{v_i}(\mathbf{x_I}, t^{n+1/2})$
5. Updating nodal displacements : $\mathbf{d}^{n+1} = \mathbf{d}^n + \Delta t^{n+1/2}\mathbf{v}^{n+1/2}$
6. compute $\mathbf{a}^{n+1}$ for velocity update: $\mathbf{v}^{n+1} = \mathbf{v}^{n+1/2} + (t^{n+1} - t^{n+1/2})\mathbf{a}^{n+1}$

Similarly, for transient heat transfer, the system of semi-discrete equations are solved using forward difference explicit scheme which is first order accurate

$$\boldsymbol{\theta}^{n+1} = \boldsymbol{\theta}^n + \Delta t(\dot{\boldsymbol{\theta}}^n) \tag{3.30}$$

$$\dot{\boldsymbol{\theta}}^n = \mathbf{C}^{-1}[\mathbf{q} - \mathbf{K}\boldsymbol{\theta}] \tag{3.31}$$

The explicit method is conditionally stable such that the time increments must satisfy following criterion

$$\Delta t = \alpha \Delta t_{crit} \quad ; \quad \Delta t_{crit} = \frac{2}{\omega_{max}} \leqslant \text{Min}\left[\frac{l_e}{c_e}\right] \tag{3.32}$$

Here, ω_{max} is the maximum frequency of linearized system, l_e is the characteristic length of the element e and c_e is the current wave speed in element e. α is the

reduction factor that accounts for destabilizing effects of non-linearity. A good choice for α is $0.8 \leqslant 0.98$. In addition, the energy conservation of the system should also be checked [32].

3.2 Finite element model set up

A 2-D plane strain model of orthogonal machining was considered in a fully coupled problem thermal-structural problem. Four node quadrilateral element with reduced integration and plane strain formulation, CPE4RT (with hourglass control) and 3 node triangular elements CPE3T were used for meshing workpiece and tool. A schematic diagram of tool and workpiece assembly and its mesh is shown in Fig. 3.2. A small control volume of work piece is considered for analysis in order to reduce computation cost. The total number of nodes and elements used for meshing the workpiece are 23411 and 23020 respectively. once the chip separation criterion was satisfied, an element deletion technique was used to allow chip separation from bulk material. The material used for workpiece is aluminum alloy A2024-T351 and a tool with tungsten carbide insert is considered. The mechanical properties for workpiece and tool are tabulated in Table 3.1.

The nodes on the edge of workpiece were constrained in displacement in x and y direction as shown in Fig. 3.2. Whereas, all the nodes of tool were constrained in y - displacement and were given a velocity V_c in negative x direction.

In machining the temperature rise is primarily due to plastic work dissipated as heat and due to frictional heat generated at tool workpiece interface. To account for temperature rise due to plastic work an inelastic heat fraction $\eta = 0.9$ is considered based on Taylor - Quinney coefficient [73]. This physically means that 90 percent of plastic work is converted to heat energy.

$$\dot{s}_p = \eta_p \sigma_{ij} \dot{\epsilon}^p_{ij} \tag{3.33}$$

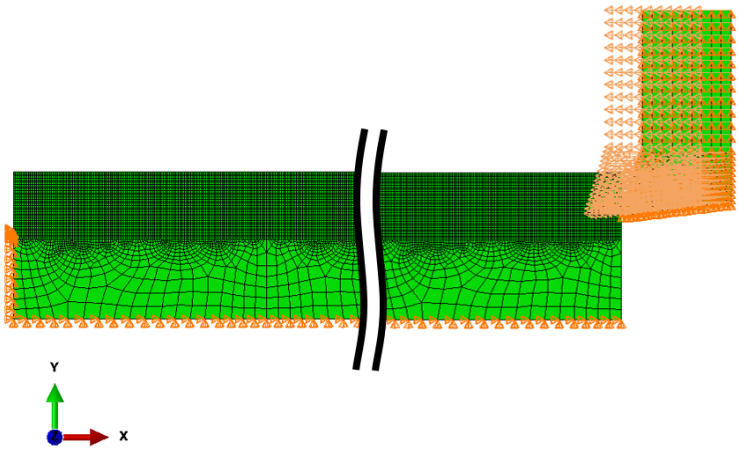

Figure 3.2: Tool and workpiece assembly with boundary conditions

Table 3.1: Material properties for workpiece and tool

Physical Property	workpiece (A2024-T351)	Tool (Tungsten carbide insert)
Density, $\rho(Kg/m^3)$	2700	11900
Young's Modulus, $E(GPa)$	73	534
Poisson's ratio, ν	0.33	0.22
Specific heat, $C_p(J/Kg/^\circ C)$	$C_p = 0.557T + 877.6$	400
Thermal expansion cff., $\alpha_d(^\circ C^{-1})$	α_d = (8.9E-3 T + 22.2)E-6	NA
Thermal conductivity, λ	$\lambda = 0.247\ T + 114.4$	
	for $25 < T < 300$	50
	$\lambda = 0.125\ T + 226$	
	for $300 < T < T_{melt}$	50

To account for heat generated due to friction, the friction work conversion factor η_f is assumed to be equal to 1. This physically means that the friction work is completely converted into heat energy. Let τ be the friction stress as defined in section 3.3, $\dot{\gamma}$ is the slip rate. The heat flux is distributed between tool and workpiece based on factor $f_f = 0.5$. The frictional heat flux at contact interface is given by:

$$\dot{h}_{\alpha f} = f_f \eta_f \tau \dot{\gamma} \tag{3.34}$$

3.3 Contact modelling

Contact modeling between tool and workpiece in finite element analysis of machining is an important aspect because the chip shape and temperature rise at tool-chip interface depends on friction. The friction at tool-chip interface is a function of normal and frictional shear stress distribution. To accurately capture the normal and shear stress distribution at the tool workpiece interface, Zorev's friction model is used.

Zorev showed in [74] that the normal stress (σ_n)at tool-chip interface is greatest at the tool tip and reduces to zero at a point on tool rake face, from where the chip loses contact with tool as shown in Figure. 3.3. For frictional (shear) stress (τ), Zorev defined stick and slip zones in the tool - workpiece contact region. The zone near the tool tip where high normal stress (σ_n) is encountered, sticking friction occurs and the zone is known as stick zone denoted by l_{stick}. In the stick zone, the shear stress is constant and given by limiting shear stress τ_y. slipping friction occurs over the remainder of tool - chip contact region and this zone is known as slip zone denoted by l_{slip} as shown in Figure. 3.3. In the slip zone, the shear stress (τ) is a function of normal stress (σ_n) and coefficient of friction (μ). In Zorev's contact model, the slip zone is essentially given by coulomb friction model. The expression for frictional shear stress (τ) is given in Equation. 3.35.

$$\begin{aligned} \text{stick zones} &: \tau = \tau_y, \quad \mu\sigma_n \geqslant \tau_y \\ \text{slip zones} &: \tau = \mu\sigma_n, \quad \mu\sigma_n < \tau_y \end{aligned} \tag{3.35}$$

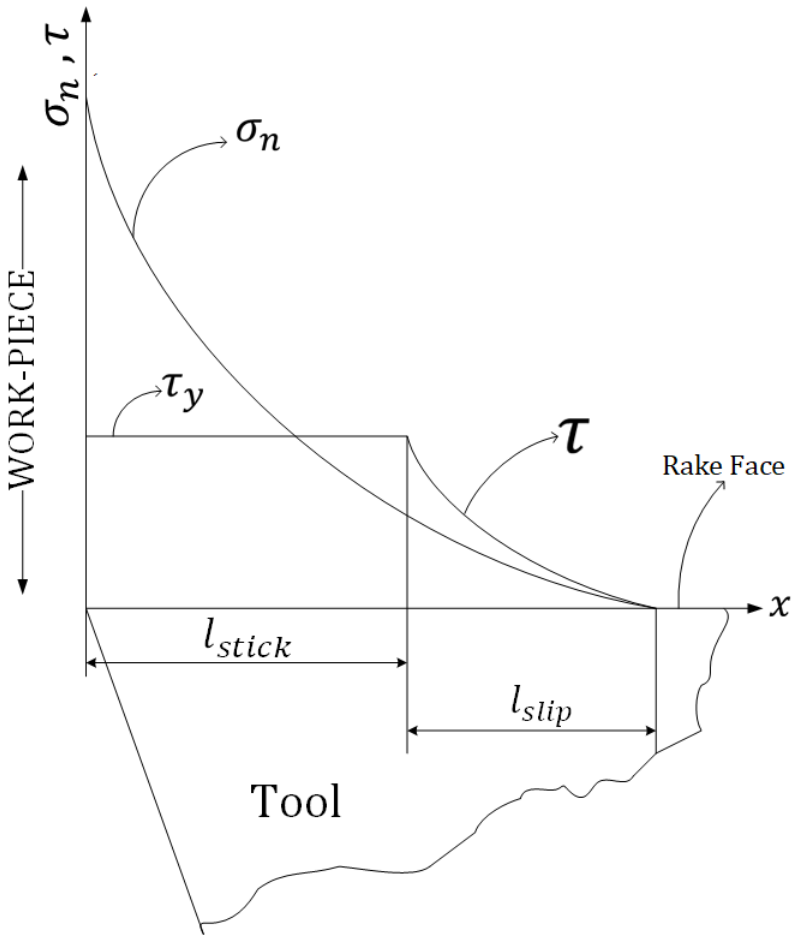

Figure 3.3: Normal stress $\sigma_n(x)$ and frictional stress τ distribution at tool rake face as per Zorev's friction model

3.3.1 Friction modeling in slip zone with a stress based model

Zorev's model has been widely used in literature to model friction on tool-chip interface. However, in slip zones (l_{slip}), the coefficient of friction (μ) is assumed to be constant and independent of normal stress (σ_n) [75].Simple Coulomb's friction model with average μ is used due to its simplicity. Such an approach for contact modeling in machining has been criticized and found to be misleading. It is worth noting that if coefficient of friction is constant over the tool rake face, as per the Coulomb's model, the curve for τ and σ_n in Fig. 3.3 should be parallel. Hence, average coefficient of friction is no longer able to accurately characterize the relationship between normal

stress and shear stress at tool-chip interface.

The core function of coefficient of friction is to map normal force (or normal stress (σ_n) with the friction shear force (or friction shear stress, τ) at the contact interface. The friction (shear) stress (τ) in the slipping zone can be considered as a function of normal stress (σ_n) as given in Equation. 3.36.

$$\tau = f(\sigma_n) \tag{3.36}$$

A stress based friction model as proposed in [76] is used to model complex frictional behaviour in slip zone. Equation. 3.36 can be expressed as a polynomial function that can represent relationship between shear stress and normal stress given by

$$\tau = \sum_{m=1}^{m=p} a_m \sigma_n^m \tag{3.37}$$

In order to construct the stress based friction model as given by Eqn. 3.37, the true stress distribution over the tool rake face must be determined using machining experiments. Two commonly used techniques to measure rake face stress distribution in metal cutting are photoelastic method [77] and split tool technique Kato et. al. [78]. In this work, the experimental data for normal and shear stress distribution over tool rake face during machining of aluminum alloy HE-10-WP is used and it is adopted from the work by Hsu in [1]. It should be noted that, that experimental data for rake face stress distribution of A2024 is not readily available and that the aluminum alloy used by Hsu in his experiments is different from what is considered for finite element analysis in this work. Hence, some degree of approximation is introduced in friction modeling. However, since experimentation is not involved in this work, the primary objective here, is to highlight the friction modeling approach to be used in finite element simulations.

To generate a stress based polynomial model, the data obtained from [1] is fitted

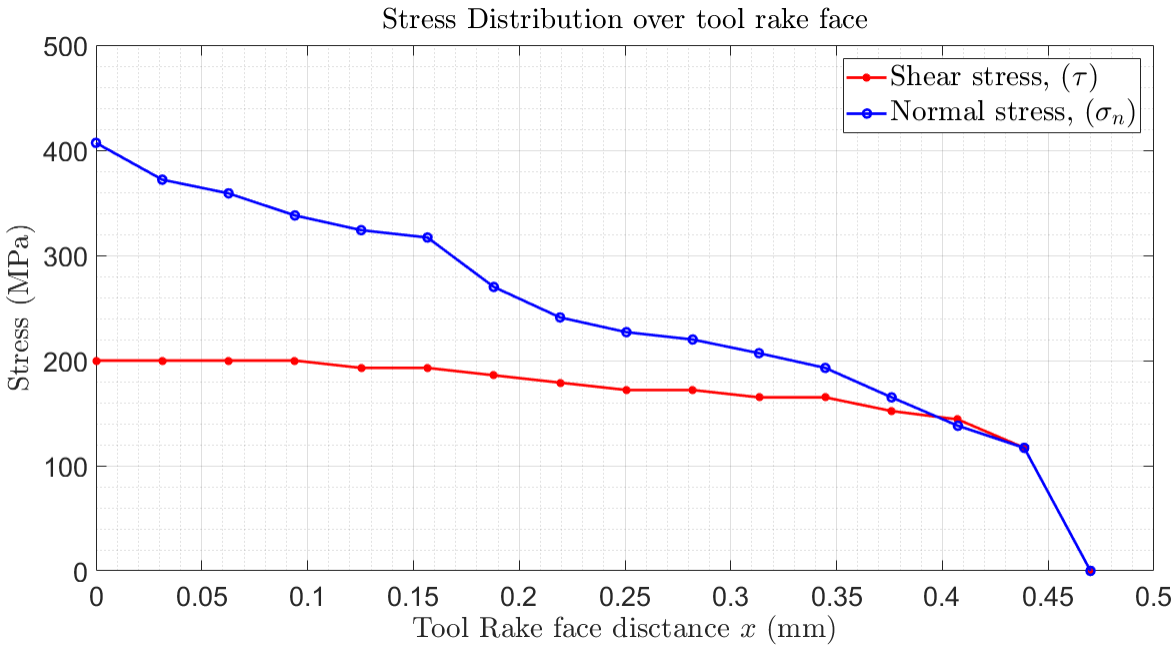

Figure 3.4: Tool rake face stress distribution with experimental data adopted from [1]

to a polynomial of degree $p = 3$ as per Eqn. 3.37. The shear stress as a function of normal stress is given by Eqn. 3.38. The Fig. 3.5 shows the stress based frictional model, where the shear stress in slip zone is not linearly related to normal stress and hence, the coefficient of friction (μ) in slip zones l_{slip} is not constant.

$$\tau = 2.795e^{-6}\sigma_n^3 - 0.003285\sigma_n^2 + 1.372\sigma_n \tag{3.38}$$

The stress based model was applied in slip zone of Zorev's friction model and in the stick zone, a limiting shear stress was considered for the frictional stress as given in Equation. 3.39.

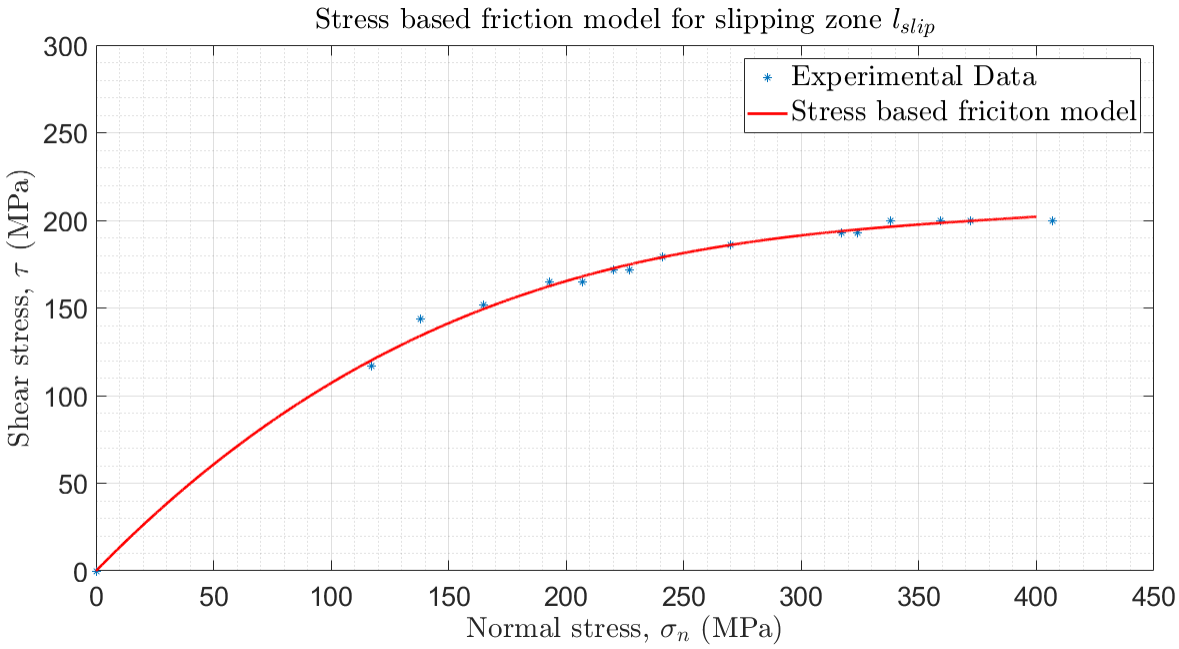

Figure 3.5: Stress based friction model in slipping zone l_{slip}

$$\begin{aligned} &\text{Stick zone} : \tau = \tau_y, && \sigma_n \geqslant 330\text{MPa} \\ &\text{Slip zone} : \tau = 2.795e^{-6}\sigma_n^3 - 0.003285\sigma_n^2 + 1.372\sigma_n, && \sigma_n < 330\text{MPa} \end{aligned} \tag{3.39}$$

The Figure. 3.5, shows that the coefficient of friction is a function of normal stress and not constant over the rake face and using an average value of coefficient of friction would result in inaccurate result.

Figure. 3.4 shows the rake face distribution of aluminum alloy obtained from [1] and it is interesting to observe that the distribution is similar to what is obtained in Zorev's friction model as shown in Fig. 3.3. This clearly indicates that the stick-slip zone model is an appropriate method to capture the tool-chip frictional interaction. The stick zone length $l_{stick} \approx 0.15$ mm, where the limiting shear stress $\tau_y \approx 203$ MPa is observed and the slip zone length $l_{slip} \approx 0.32$.

The tool-chip contact interactions were modeled in Abaqus using penalty stiffness

Table 3.2: Johnson-Cook model parameters for Al2024-T351.

A (MPa)	B (MPa)	n	C	m	$T_{transition}$ $(^{\circ}C)$	T_{melt} $(^{\circ}C)$
352	440	0.42	0.0083	1	25	520

contact formulation by defining master and slave surfaces as tool and chip respectively. In addition a self contact of chip with itself was also defined using penalty contact formulation.

3.4 Johnson-Cook Constitutive Model

Machining is a process which involves high strains, high strain rates and temperatures. In this work, such a behavior is modeled as a fully coupled Thermo-Visco-Plastic process, using Johnson-Cook (JC) constitutive model for material modeling.

The Johnson-Cook (JC) constitutive model is formulated empirically and it is based on Mises plasticity where Mises yield surface (J2 plasticity theory) is associated with flow rule. JC - constitutive equation considers isotropic hardening and can model Thermo-Visco-Plastic problem over a strain rate range of 10^2 to 10^5 s^{-1}. The flow stress is a function of strain, strain rate and temperature and is given by:

$$\bar{\sigma}(\bar{\epsilon}, \dot{\bar{\epsilon}}, T) = \underbrace{(A + B\bar{\epsilon}^n)}_{\text{Isotropic Hardening}} \underbrace{\left[1 + C \ln\left(\frac{\dot{\bar{\epsilon}}}{\dot{\epsilon}_0}\right)\right]}_{\text{Strain rate Hardening}} \underbrace{\left[1 - \bar{T}^m\right]}_{\text{Thermal Softening}} \tag{3.40}$$

here,

$$\bar{T} = \begin{cases} 0, & T < T_{trans} \\ \dfrac{T - T_{trans}}{T_{melt} - T_{trans}}, & T_{trans} < T < T_{melt} \\ 1, & T > T_{melt} \end{cases} \tag{3.41}$$

In Eqn. (3.40) the first term in the bracket accounts for isotropic hardening. The

second term accounts for strain rate hardening whereas The third term accounts for thermal softening. The Material Parameters A, B, n, C and m for the JC model must be measured below Transition temperature. These parameters are determined by empirical fit of flow stress data obtained from high strain rate testing done in compression and tension. There are various experimental methods to determine JC model parameters, one such technique is using the Split Hopkinson Pressure Bar (SHPB) test [79] and [80]. The material parameters used in this work for Johnson-Cook constitutive model as tabulated in Table 3.2, are adopted from [81] and the same parameters were also used by [82]. Other mechanical and thermal properties for work material and tool is adopted from [82].

In machining, material hardening occur due to high strain and strain rates and at the same time softening occur due to high temperatures. Moreover, thermal softening of material, in turn increases strain rates resulting in strain rate hardening. Such a behaviour is mainly encountered in the primary shear zone where viscoplastic effects are dominant and in secondary shear zone where frictional effects dominates during cutting. The figs. [3.6 - 3.9] shows stress-strain response of A2024-T351 at different temperatures for a given strain rate. The figs. [3.10 - 3.13] shows stress - strain response of A2024-T351 at different strain rates for a given temperature.

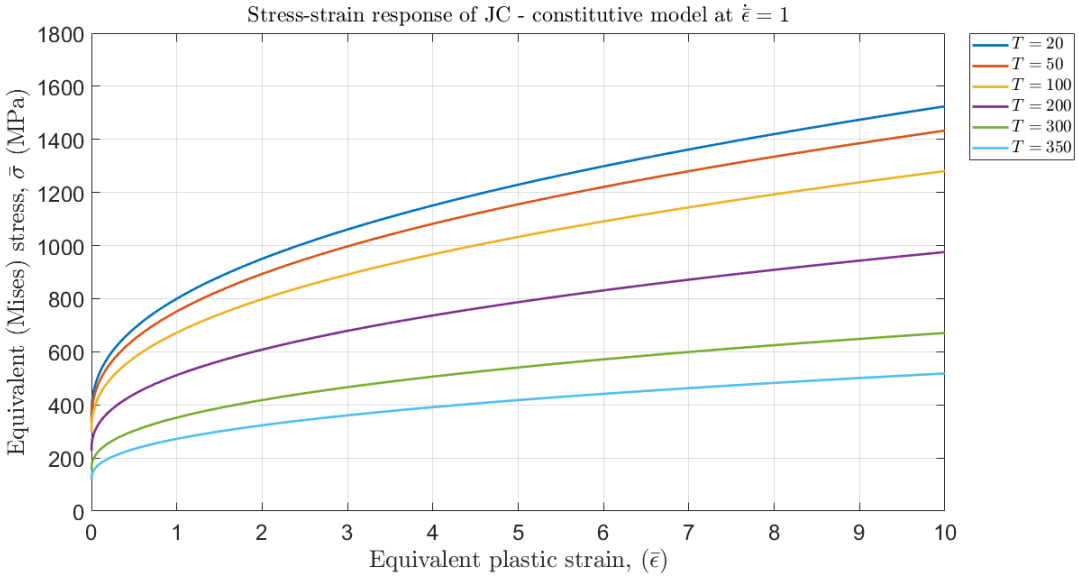

Figure 3.6: $\bar{\sigma}$ vs $(\bar{\epsilon})$ response of A2024 using JC-constitutive model at various temperature (T) for fixed $\dot{\epsilon} = 1$ s^{-1}.

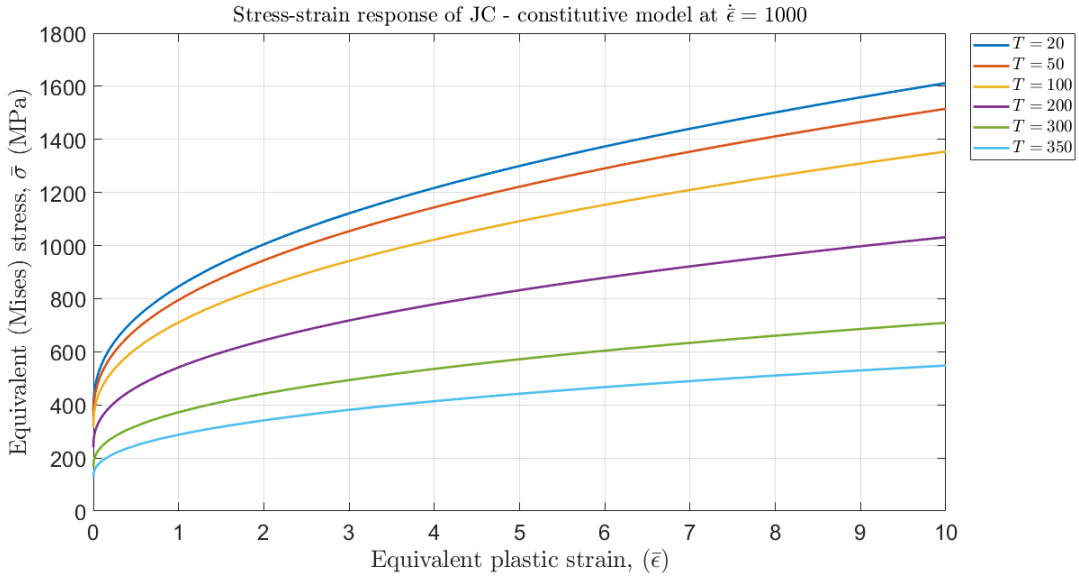

Figure 3.7: $\bar{\sigma}$ vs $(\bar{\epsilon})$ response of A2024 using JC-constitutive model at various temperature (T) for fixed $\dot{\epsilon} = 1000$ s^{-1}.

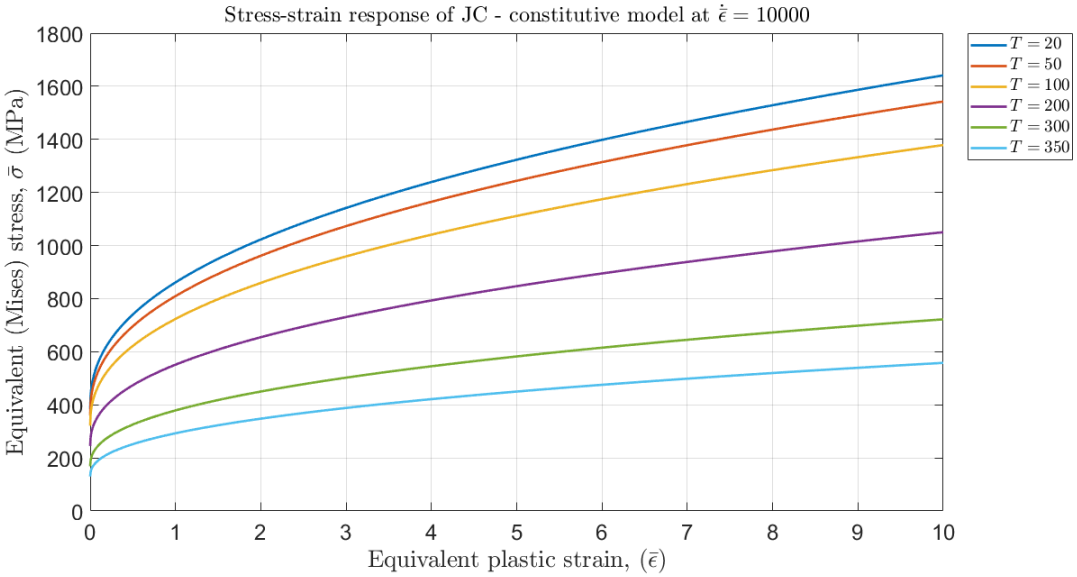

Figure 3.8: $\bar{\sigma}$ vs $(\bar{\epsilon})$ response of A2024 using JC-constitutive model at various temperature (T) for fixed $\dot{\bar{\epsilon}} = 10000$ s^{-1}.

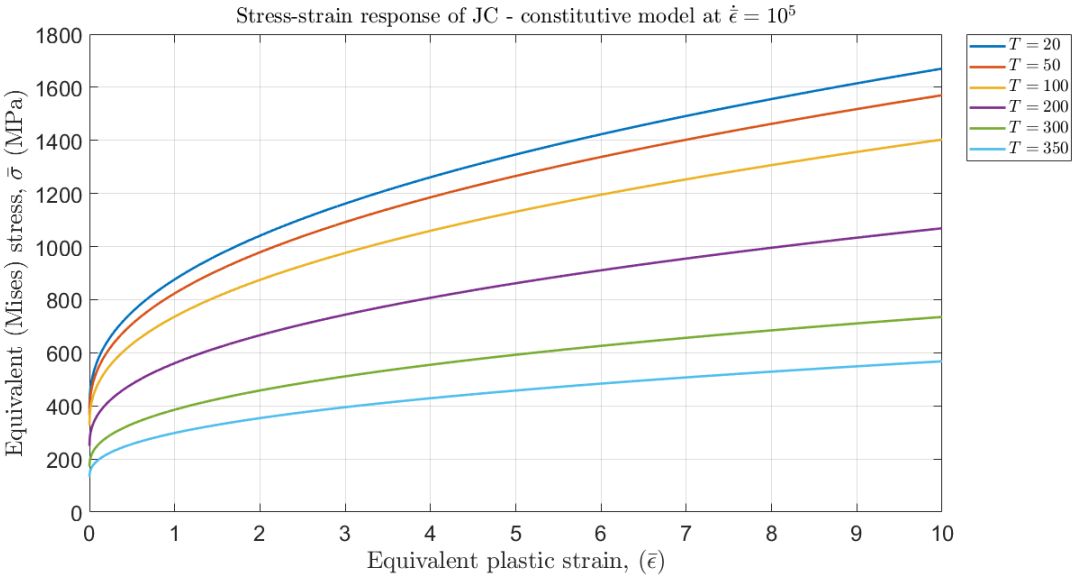

Figure 3.9: $\bar{\sigma}$ vs $(\bar{\epsilon})$ response of A2024 using JC-constitutive model at various temperature (T) for fixed $\dot{\bar{\epsilon}} = 10^5$ s^{-1}.

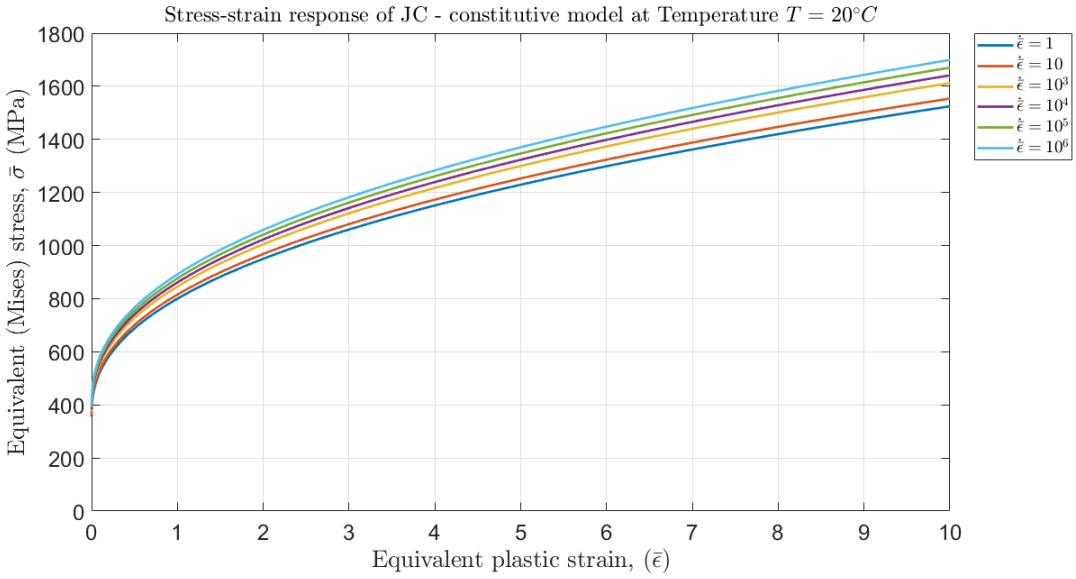

Figure 3.10: $\bar{\sigma}$ vs $(\bar{\epsilon})$ response of A2024 using JC-constitutive model at various strain rates $(\dot{\bar{\epsilon}})$ for fixed temperature $T = 20°$C.

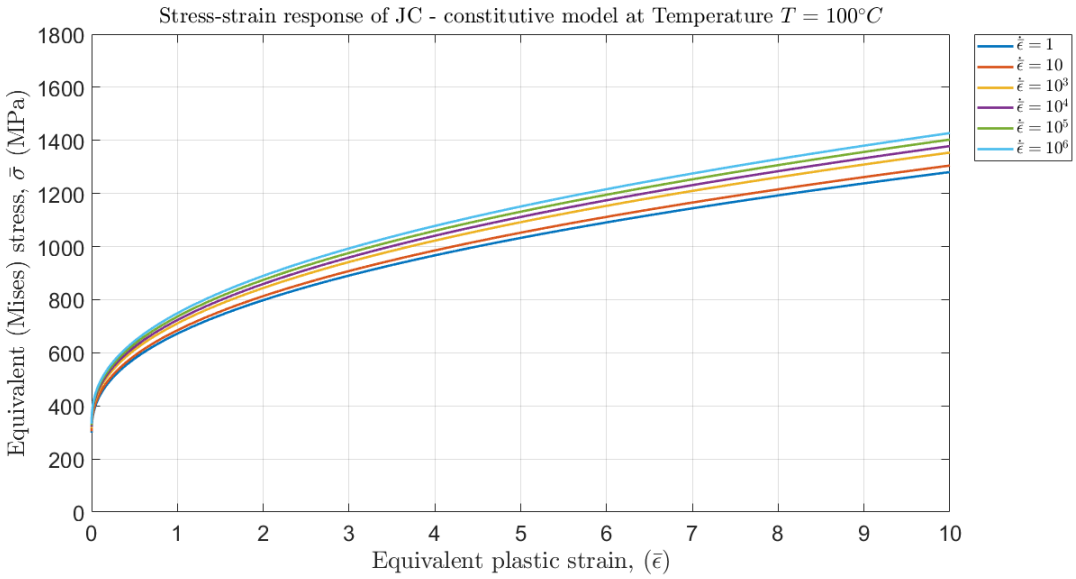

Figure 3.11: $\bar{\sigma}$ vs $(\bar{\epsilon})$ response of A2024 using JC-constitutive model at various strain rates $(\dot{\bar{\epsilon}})$ for fixed temperature $T = 100°$C.

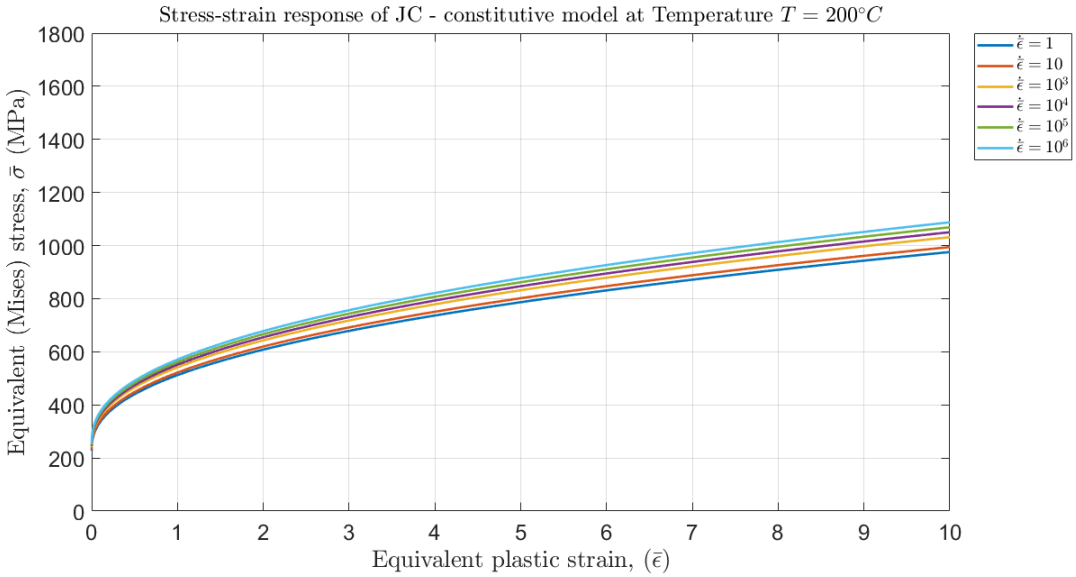

Figure 3.12: $\bar{\sigma}$ vs $(\bar{\epsilon})$ response of A2024 using JC-constitutive model at various strain rates $(\dot{\bar{\epsilon}})$ for fixed temperature $T = 200°$C.

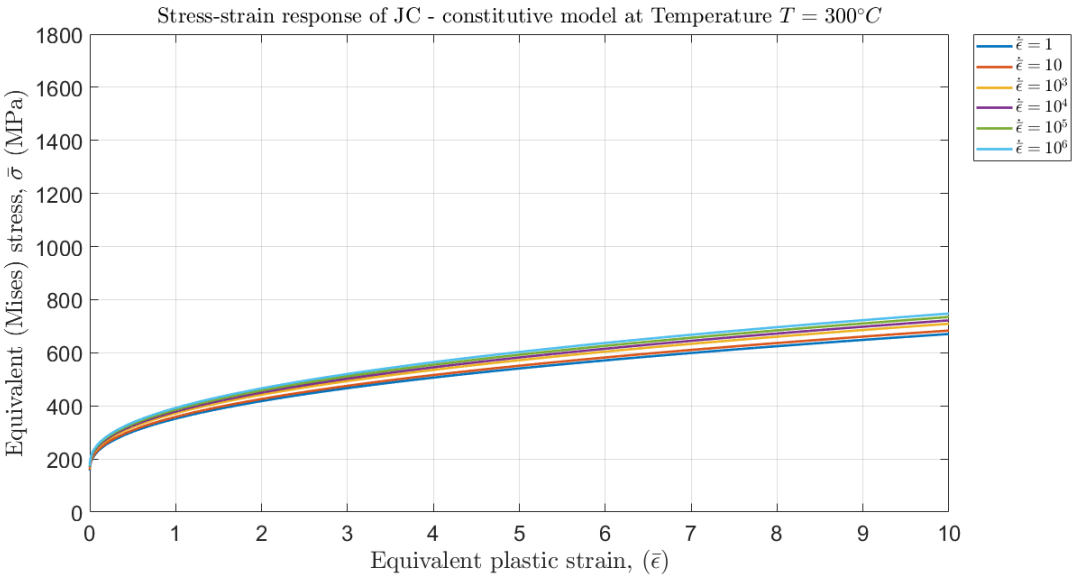

Figure 3.13: $\bar{\sigma}$ vs $(\bar{\epsilon})$ response of A2024 using JC-constitutive model at various strain rates $(\dot{\bar{\epsilon}})$ for fixed temperature $T = 300°$C.

3.5 Johnson-Cook damage model

Machining is a phenomenon resulting from damage and fracture of material. Chip formation occurs as a result of damage and fracture of material due to action of the cutting tool. Ductile fracture occurs due to two main mechanisms, first one is due to nucleation, growth and coalescence of voids and second is shear fracture due to shear band localization as shown in fig. 3.14. Li et. al. showed in [83] with experiments and computational simulations that several factors such as pressure stress, stress triaxiality, the Lode parameter, equivalent plastic strain, shear stress and non-uniform plastic deformation modes influence the damage evolution due to void nucleation/growth/coalescence and shear band localization. It is these factors that determine whether the deformation mode is shear dominant or maximum principal stress dominant deformation and thus the mode of ductile fracture can be dimple fracture, shear fracture or mixed mode fracture. Hooputra et al. [84] developed an approach for predicting damage initiation in metals based on these two mechanisms. In addition, Bai and Wierzbicki [85] showed, based on experimental results for aluminum alloys and other metals concluded that in addition to stress triaxiality and strain rate, ductile fracture can also depend on the third invariant of deviatoric stress which is related to Lode angle. Teng and Wierzbicki[81] investigated six ductile fracture model in order to identify the most suitable fracture criterion for high velocity perforation problems. In this work, Johnson-Cook Damage Model (JC damage mdoel) [86] in conjunction with Johnson cook constitutive model was used to model machining as a process resulting from damage in a material. The JC damage model considers that the overall damage in a material occurs in two steps [87]: Damage Initiation and Damage Evolution.

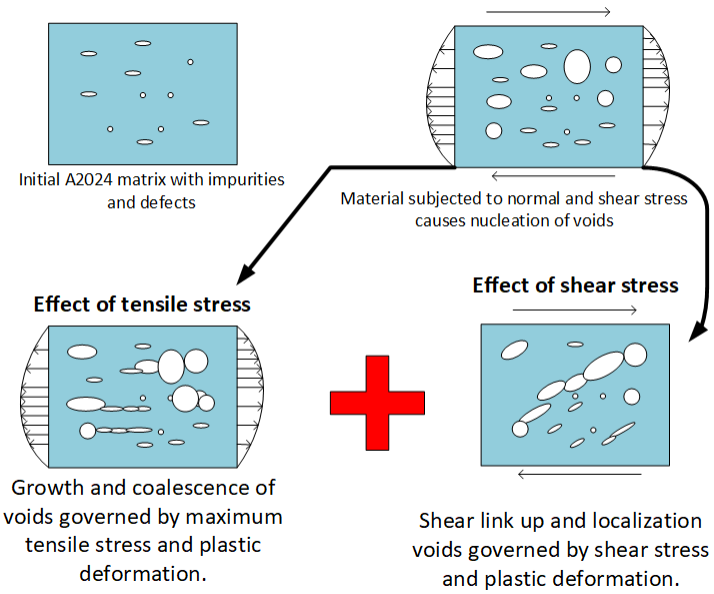

Figure 3.14: Mechanisms of ductile fracture

3.5.1 Damage initiation

The Johnson-Cook dynamic failure model is used for modeling damage initiation. According to this criterion, the equivalent plastic strain at the onset of damage and hence the overall accumulation of damage is a function of stress triaxiality, strain rate and temperature. The JC-damage model, based on the values of equivalent plastic strain at the integration points in a finite element, assumes that damage initiates when the damage parameter, ω, defined as

$$\omega = \sum \frac{\Delta \bar{\epsilon}}{\bar{\epsilon}_d} \tag{3.42}$$

Table 3.3: Johnson-Cook Damage model parameters for Aluminum alloy Al2024-T351.

$D1$	$D2$	$D3$	$D4$	$D5$
0.13	0.13	1.5	0.011	0

equals one. Here, summation is performed over all time increments in the FE analysis. The equivalent plastic strain $\bar{\epsilon}_d$ at the onset of damage initiation is given by [86]:

$$\bar{\epsilon}_d = \left[D_1 + D_2 \exp\left(D_3 \frac{p}{\bar{\sigma}}\right)\right]\left[1 + D_4 \ln\left(\frac{\dot{\bar{\epsilon}}}{\dot{\epsilon}_0}\right)\right] \times \left[1 + D_5 \bar{T}\right] \tag{3.43}$$

here,

$$\bar{T} = \begin{cases} 0, & T < T_{trans} \\ \dfrac{T - T_{trans}}{T_{melt} - T_{trans}}, & T_{trans} < T < T_{melt} \\ 1, & T > T_{melt} \end{cases} \tag{3.44}$$

D_1 to D_5 are failure parameters measured at or below transition temperature T_{trans}. The Johnson-Cook Parameters considered in this paper are tabulated in Table 3.3. These values adopted from [81] and the same parameters were also used by [82]. The value of D_5 is zero which shows that temperature does not have any effect on damage of Aluminum [82].

Once the damage initiation criterion is satisfied, the material stiffness is progressively degraded according to the specified damage evolution model, eventually leading to complete damage of the material. It is worth noting that many past attempts at modeling machining do not consider damage evolution.

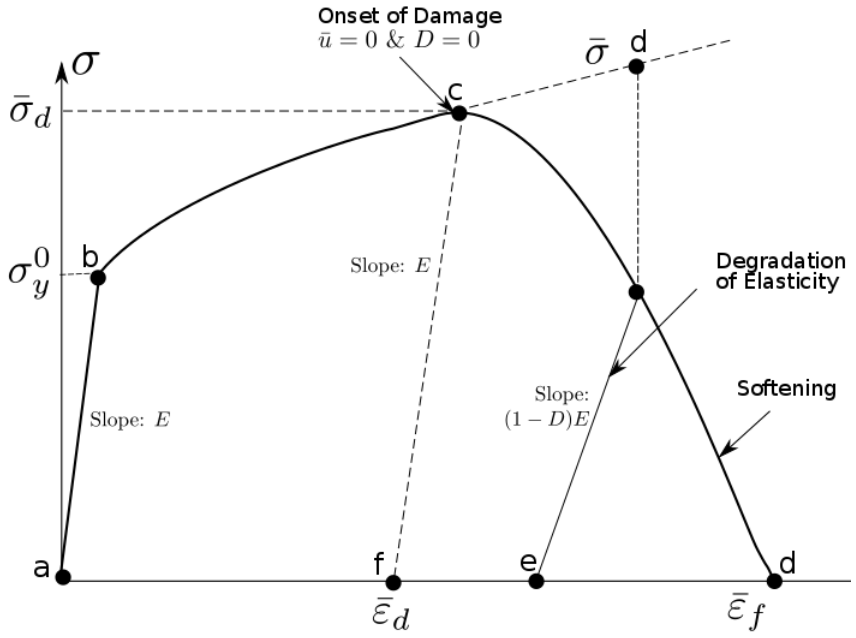

Figure 3.15: Stress-strain curve

3.5.2 Damage Evolution

The Damage evolution model describes, the rate of degradation of the material stiffness once the corresponding damage initiation criterion has been reached. The Fig. 3.15 shows typical stress-strain response of a material undergoing damage. The material response is initially linear from point a to b followed by isotropic hardening and inelastic deformation from b to c. At point c, the damage initiation criterion is satisfied (i.e., $\omega \geq 1$). Beyond point c the damage manifest itself into two forms: softening of the yield stress and degradation of the elasticity due to which the load carrying capacity of material is remarkably decreased. Most of the deformation beyond point c in uniaxial test specimen occurs in the neck region. Such a response from c to d is governed by evolution of degradation of stiffness in the region of strain localization. In the context of damage mechanics c to d can be viewed as the degraded response of the curve c to d' that the material would have followed in the absence of damage [87].

In Fig. 3.15 $\bar{\epsilon}_d$ and $\bar{\sigma}_d$ is equivalent plastic strain and yield stress respectively at onset of damage. D is overall damage variable defined such that when $D = 1$, the stiffness of the element is completely degraded. The equivalent plastic strain at this point is denoted by $\bar{\epsilon}_f$.

Unlike continuum mechanics where the constitutive model is normally expressed in terms of stress and strain relationship, in a material where damage occurs due to strain localization, the stress-strain relationship no longer accurately represents the material's behavior. Continuing to use the stress-strain relation introduces a strong mesh dependency based on strain localization, such that the energy dissipated decreases as the mesh is refined. In Abaqus, damage evolution (softening response) is governed by a stress-displacement relation in order to alleviate strong mesh dependencies. The implementation of this stress-displacement concept in a finite element model requires the definition of a characteristic length, L, associated with an integration point to alleviate mesh dependency. it is a typical length of a line across an element for a first-order element; it is half of the same typical length for a second-order element. Hillerborg's fracture energy model [88] is coupled with the JC-damage model for this purpose.

3.5.3 Hillerborg model

Hillerborg's fracture model has some similarities with the Barenblatt's cohesive force model, where the amount of energy absorbed per unit crack area in opening the crack from 0 to u is given by

$$G_c = \int_0^{\bar{u}} \bar{\sigma} d\bar{u}. \tag{3.45}$$

Hillerborg's fracture energy [88] is used to reduce mesh dependency by creating a stress-displacement response after damage is initiated. Using brittle fracture concepts, Hillerborg defined the energy required to open a unit area of crack, G_f, as a material

parameter. The "crack" here corresponds to micro-cracked zones created after damage initiation with some material ligaments remaining for stress transfer. Once all the ligaments are broken, the crack would propagate and the stored energy is released to form new surfaces.

Crack propagation occurs when the energy release rate is equal to or greater than critical energy release rate, G_f which represents area under curve $\sigma(\bar{u})$ in stress-displacement relation as shown in Figs. 3.16a and 3.17a. The figures show that the curve for $\sigma(\bar{u})$ may be chosen in different ways to apply Hillerborg's fracture model depending upon response of the material under damage. In this work, the critical energy release rate, used as a criterion for chip separation and serration is given by

$$G_f = \int_{\bar{\epsilon}_d}^{\bar{\epsilon}_f} L\bar{\sigma}_y d\bar{\epsilon} = \int_0^{\bar{u}_f} \bar{\sigma}_y d\bar{u} \tag{3.46}$$

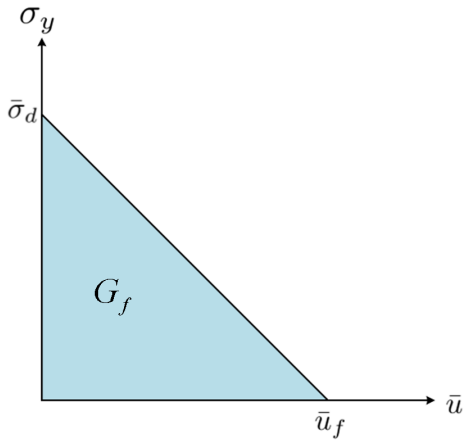

(a) Flow stress vs Equivalent plastic displacement in linear damage model

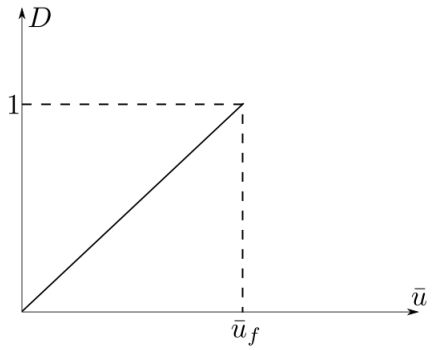

(b) Damage variable vs Equivalent plastic displacement in linear damage model

Figure 3.16: Linear damage model: variation of $\bar{\sigma^y}$ and D with the equivalent plastic displacement

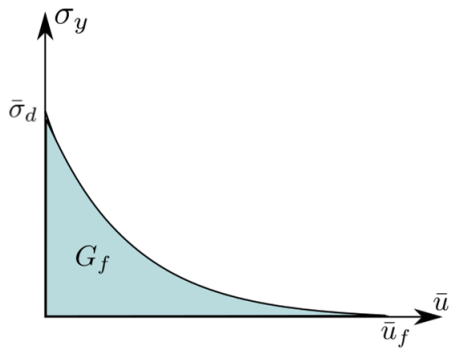

(a) Flow stress vs Equivalent plastic displacement in exponential damage model

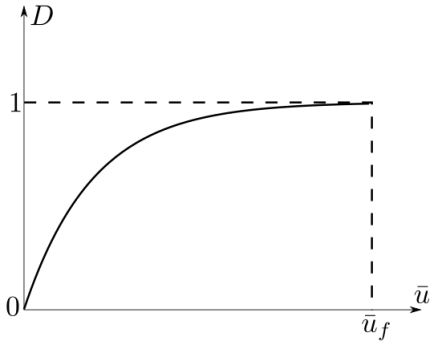

(b) Damage variable vs Equivalent plastic displacement in exponential damage model

Figure 3.17: Exponential damage model: variation of $\bar{\sigma^y}$ and D with the equivalent plastic displacement

In Eqn. 3.46, the equivalent plastic displacement, $\bar{u}$, is a fracture work conjugate of yield stress $\bar{\sigma}_y$ after the onset of damage. Before damage initiation (at point C in Fig. 3.15) $\dot{\bar{u}} = 0$, whereas after damage initiation $\dot{\bar{u}} = L\dot{\bar{\epsilon}}$ with L being a characteristic length of the element.

If a linear form of Hillerborg's fracture model as shown in Figure. 3.16a is chosen, the critical energy release rate or fracture energy in terms of the equivalent plastic displacement at failure is given by

$$G_f = \frac{1}{2}\bar{u}_f\bar{\sigma}_d \quad \text{or} \quad \bar{u}_f = \frac{2G_f}{\bar{\sigma}_d}. \tag{3.47}$$

A scalar stiffness degradation variable (SDEG) D is used in Abaqus to quantify the damage evolution based on increment of equivalent plastic displacement. For a linear model, it is given by

$$\dot{D} = \frac{L\dot{\bar{\epsilon}}}{\bar{u}_f} = \frac{\dot{\bar{u}}}{\bar{u}_f} \tag{3.48}$$

The above result is based on the assumption that the yield stress of the material remains at σ_d (see Fig 3.15) as D evolves. From Eqns 3.47 and 3.48, the incremental change in D is computed from

$$\dot{D} = \frac{L\dot{\bar{\epsilon}}}{(2G_f/\bar{\sigma}_d)} = \frac{\dot{\bar{u}}}{\bar{u}_f} \tag{3.49}$$

The accumulated overall damage variable is computed as a sum of all increments for each element:

$$D_n = D_{n-1} + \dot{D} = \frac{\bar{u}_{n-1} + \dot{\bar{u}}}{\bar{u}_f} = \frac{\bar{u}_n}{\bar{u}_f} \tag{3.50}$$

When $D_n = 1$ in an element, the element is considered to be completely degraded and it is removed from the model. A typical representation for damage variable vs equivalent plastic displacement response in linear evolution is shown in Fig. 3.16b.

If an exponential form of damage model is chosen as shown in Fig. 3.17a, The critical energy release rate is given by:

$$G_f = \int_0^{\bar{u_f}} \bar{\sigma}_y d\bar{u}. \tag{3.51}$$

The scalar stiffness degradation variable (SDEG) is given by:

$$D = 1 - \exp\left(- \int_0^{\bar{u}} \frac{\bar{\sigma_y} d\bar{u}}{G_f} \right) \tag{3.52}$$

In Eqn. (3.52), the numerator within the integral, $\bar{\sigma_y} d\bar{u}$ is the stored strain energy dissipated in each increment of fracture evolution. Since D approaches 1 when $\bar{u}$ approaches infinity, in ABAQUS, D is taken to be one when the total dissipated energy for each element approaches $0.99G_f$. A typical material response in case of exponential damage evolution is shown in Figs. 3.17a and 3.17b. Again, when $D = 1$ in an element, the element is removed from the model.

CHAPTER 4: CRITICAL ENERGY RELEASE RATE FOR CHIP SEPARATION

Finite element simulation, requires a criterion to simulate chip separation from the bulk when the tool moves and interacts with workpiece. As mentioned in earlier chapters, the chip separation criterion should reflect closely the physics and mechanics of chip formation to achieve reliable results. Atkins model highlighted that during the analysis of machining processes, the energy required to generate new surfaces which is known as critical energy release rate (or fracture toughness) should be taken into account. Hence, a suitable chip separation criterion can be based on damage and fracture of materials. The chip separation criterion should be determined experimentally in such a way that the effects of high strain rates and temperatures involved in machining are considered. Moreover, It is very important that the selected chip separation criterion is universal for a given material and its value should not change with changing cutting parameters.

In this work, the critical energy release rate (G_f) is used as chip separation criterion in Lagrangian finite element modeling of orthogonal cutting. Moreover, similar criterion can also be considered to model discontinuous chips where, chip serration and chip breakage is also considered as a process in which new surfaces are created. A very important question in this approach is the method to determine fracture energy for a given material and cutting parameters. Two separate criteria for chip separation and serration based on energy required to create new surfaces (critical energy release rate: G_f) which are calculated from Hillerborg Fracture model are used. First, we note that the total amount of energy or external work in a cutting process is consumed in: (a) Plastic work, (b) Frictional work between too-chip interactions, (c) Energy spent on forming new surfaces (material separation due to ductile fracture)

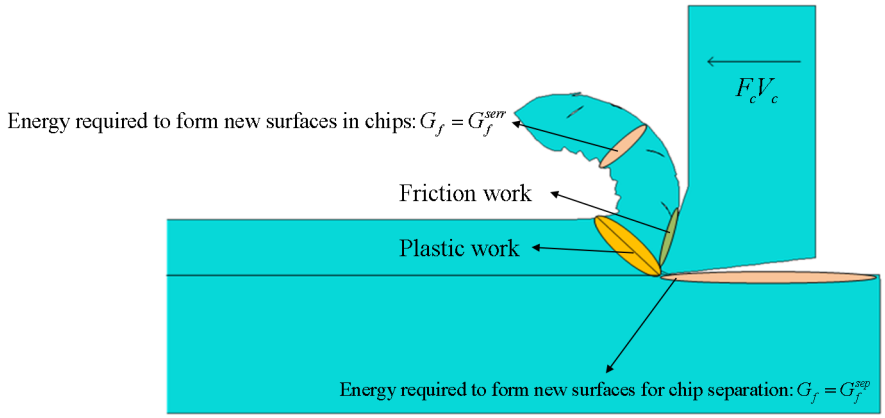

Figure 4.1: Distribution of external work in machining

when chips are generated and (d) Energy spent in forming new surfaces for chip serration or chip breakage ([69], [89], [90]). The energy defined in (c) is G_f^{sep} and that in (d) is G_f^{serr}. These are the critical/threshold quantities needed for Hillerborg fracture energy G_f in the chosen damage evolution model for element deletion in the chip and workpiece (see Fig. 4.2).

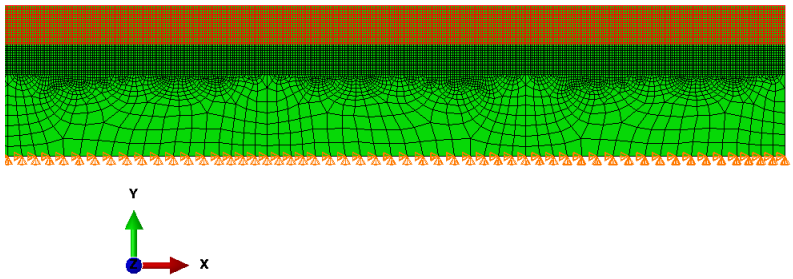

(a) The element deletion criterion based on G_f^{serr} is used in the meshed workpiece region

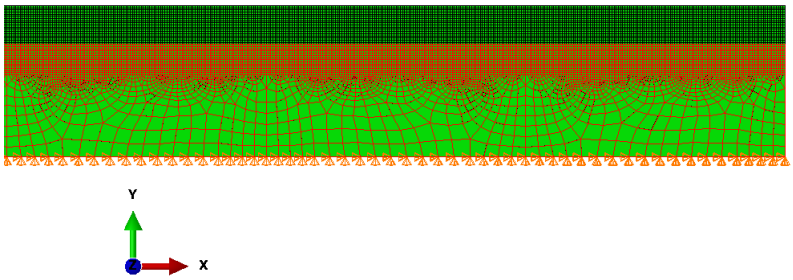

(b) The element deletion criterion based on G_f^{sep} is used in the meshed workpiece region.

Figure 4.2: The element deletion criteria used for chip separation and chip serration (or breakage)

Mabrouki et. al. in [82] considered that the Hillerborg fracture energy G_f in damage evolution model is a function of Young's modulus E and Poisson's ratio ν and expressed it as conventional LEFM formula for critical energy release rate or fracture toughness given by:

Mode-I and Mode-II fracture plane strain condition:

$$(G_f)_{I,II} = \left(\frac{1-\nu^2}{E}\right)(K^2_{Ic,IIc}) \tag{4.1}$$

Mabrouki et al. [82] were the first ones to use two different threshold values for chip separation and serration. They used the Hillerborg fracture energy G_f [88] in the

damage evolution model and set the threshold values as

$$(G_f)_{I,II} = \left(\frac{1-\nu^2}{E}\right)(K^2_{Ic,IIc}). \tag{4.2}$$

In the above, the subscripts I, II represent Mode-I and Mode-II fracture. These expressions are obviously based on the linear elastic fracture mechanics. The chip separation was considered as a case of Mode-I fracture and chip serration as a case of Mode-II fracture. Consequently, rate and thermal effects are not considered while determining the threshold value for criteria used. Furthermore, $(G_f)_I > (G_f)_{II}$ since $K_{cI} > K_{cII}$. This is not in agreement with the observations of (a). Zhang et. al. [40] that the fracture toughness of the chip can be twice as high as that of workpiece and (b). Bing et. al [70] that the fracture toughness of chip is higher than bulk material. A consequence of basing the critical values of G_f on LEFM (as above) is that due to the lower values of G_f for the element deletion in the chip than that in front of the tool tip where cutting takes place, the elements within the chips are deleted prematurely. This can have a major impact on the chip shape predictions as well as on element distortions in FE simulations.

In this work, we consider machining as a problem of ductile fracture mechanics with the recognition that the energies required to form new surfaces during material separation [69] and during chip serration or breakage need not be the same ([70], [40], [91]). Therefore, different threshold values for chip separation and chip serration are used in the present work. The Johnson-cook damage initiation and damage evolution model that takes into account the mechanism for ductile failure due to nucleation, growth and coalescence of voids along with shear band localization is considered. In addition, since there are two damage models available in ABAQUS, namely linear and exponential, the effect of using these different models on chip morphology, cutting forces, stress, and other field variables is also analyzed.

4.1 Determination of threshold value for G_f^{sep} using William's model

It is important to determining fracture toughness using machining experiments for any given material because in that way the strain hardening, strain rate and thermal softening effects on its value would be captured accurately. Patel et. al. developed a cutting test method in [71] and [2] and derived an analysis scheme for determination of fracture toughness G_c from cutting test data. This method referred to as William's method is used to determine the threshold value of critical energy release rate or fracture toughness G_f^{sep} required as a criterion for chip separation following the damage initiation.

Similar to Atkin's approach, William's model is based on energy balance and uses Merchant's force minimization criterion to determine shear plane angle ϕ. William's model poses the problem of machining by appreciating that the energy required to generate new surfaces in machining should be included in the analysis. Moreover, the traditional view of ignoring fracture energies due to absence of visible crack in front of the crack tip was criticized by Patel et. al. in [71] and they showed in [90] and [92] that in case of machining ductile materials, cutting tool may touch the crack tip and hence the need of crack to precede the tool is obviated.

William's method requires experimental measurement of force in cutting direction denoted by F_c and in transverse direction denoted by F_t for a given width of cut w . This scheme also involves plotting machining force versus uncut chip thickness which gives a positive intercept at zero uncut chip thickness. Using this intercept the fracture toughness of material in machining could be determined.

The Figure. 4.3, shows a schematic diagram of a work material being cut by a tool of rake angle α with a cutting speed V_c. The uncut chip thickness of the work material is a_c and the chip thickness after material separation is $a_c h$. There is some clearance angle to reduce friction in cutting. The shear plane is formed at angle ϕ to the plane of cut surface and a shear force denoted by F_s and normal force F_n acts on the shear

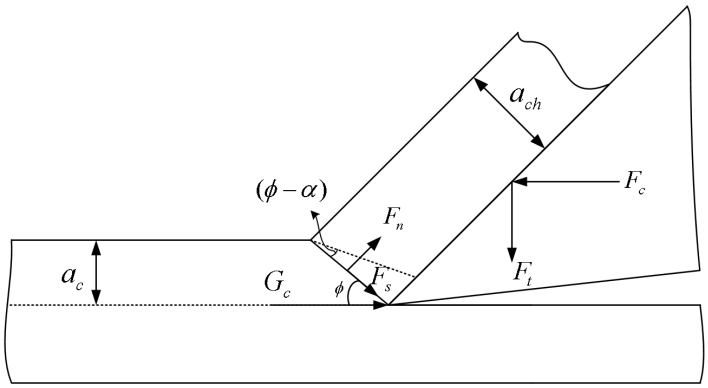

Figure 4.3: Schematic Diagram of force analysis in machining

plane. It should be noted that F_s and F_n are generally obtained by resolving cutting force component F_c and transverse force component F_t along the shear and normal directions respectively. In Merchant's analysis, when energy required to generate new surfaces was ignored, the following equations were derived:

$$F_s = F_c \cos\phi + F_t \sin\phi \tag{4.3}$$

$$F_n = F_c \sin\phi + F_t \cos\phi \tag{4.4}$$

The primary force in machining is the cutting force F_c, which additionally generates transverse force F_t on the chip as shown in Figure. 4.3. In this analysis the tool is assumed to fit behind the chip and it touches the end of shear plane where chip is separated from the bulk. consequently, the tool is a primary source of external energy which is delivered into fracture process. The equilibrium of forces on shear plane needs to consider reaction force "wG_c" acting at tool tip, to model and consider fracture toughness of the material G_c in the analysis.

To considering an energy balance of the system, assume that the tool moves a distance dx, then an increment of external work is given by Equation. 4.5. This

external work is dissipated into plastic work in the shear plane dU_{plas}, frictional work at tool chip interaction dU_{fric} and fracture work or energy released to create new surface while chip is separated from the bulk dU_{fract}. The energy balance of the system is given by Equation. 4.6, where the total dissipated energy is denoted by dU_{diss}.

$$dU_{ext} = F_c dx \tag{4.5}$$

$$dU_{ext} = dU_{diss} = dU_{plas} + dU_{fric} + dU_{fract} \tag{4.6}$$

The Shear force S on the tool-chip interface is given by:

$$S = [(F_c - wG_c)\sin\alpha + F_t\cos\alpha] \tag{4.7}$$

S moves a distance dx_{ch} along the tool rake face when tool moves a horizontal distance of dx. Considering plane strain conditions we have

$$a_{ch}dx_c = a_c dx \tag{4.8}$$

Let AB be the length of shear plane as shown in Figure. 4.3

$$AB = \frac{a_c}{\sin\phi} = \frac{a_c h}{\cos(\phi - \alpha)} \tag{4.9}$$

The increment of frictional work dU_{fric} is given by:

$$dU_{fric} = Sdx_c = [(F_c - wG_c)\sin\alpha + F_t\cos\alpha]\frac{\sin\phi}{\cos(\phi - \alpha)}dx \tag{4.10}$$

Considering, du_s as displacement of a point along the shear plane, then for a tool

movement of dx,

$$du_s = dx[\cos\phi + \sin(\phi)\tan(\phi - \alpha)] = \frac{\cos\alpha}{\cos(\phi - \alpha)}dx \tag{4.11}$$

the increment in plastic work is given by:

$$dU_{plas} = F_s\frac{\cos\alpha}{\cos(\phi - \alpha)}dx \tag{4.12}$$

The energy balance from Equation. 4.6 is given by:

$$F_c dx = [(F_c - wG_c)\sin\alpha + F_t\cos\alpha]\frac{\sin\phi}{\cos(\phi - \alpha)}dx + F_s\frac{\cos\alpha}{\cos(\phi - \alpha)}dx + wG_c dx \tag{4.13}$$

Considering fracture toughness G_c in the force analysis, from the Schematic diagram in Figure. 4.3, the shear force on shear plane is given by:

$$F_s = (F_c - wG_c)\cos\phi - F_t\sin\phi \tag{4.14}$$

In the above analysis, Patel et. al. [71] assumed initially that the shear plane is formed at some critical shear stress, σ_s which obeys Tresca yield criterion such that $\sigma_s = \sigma_y/2$, where σ_y is the yield tensile stress. It should be noted that the effective yield stress in the shear plane in cutting process is much greater than $\sigma_y/2$ due to work and rate hardening. However, since this test method includes experiments with machining, the σ_s obtained from experimental results considers hardening effect as well and Patel et. al. showed that the results for σ_s calculated from William's method agrees to experimenally fitted stress starin curve [71].

Now the length of shear plane is given by $a_c/sin\phi$ and hence Shear force F_s on

shear plane considering Tresca Yield criterion is given by:

$$F_s = \frac{\sigma_y}{2} \frac{w a_c}{\sin \phi} \tag{4.15}$$

from Equation. 4.14 and 4.15 the force balance on shear plane is given by:

$$\frac{\sigma_y}{2} \frac{w a_c}{\sin \phi} = \left(\frac{F_c}{w} - G_c \right) \cos \phi - \frac{F_t}{w} \sin \phi \tag{4.16}$$

Thus, from William's model Equation. 4.16 can be rearranged as

$$\left(\frac{F_c}{w} - \frac{F_t}{w} \tan \phi \right) = \frac{\sigma_y a_c}{2} \left(\tan \phi + \frac{1}{\tan \phi} \right) + G_c \tag{4.17}$$

From the experiment of orthogonal cutting, Along with measuring F_c/w and F_t/w, chip thickness a_{ch} should be measured after inlaying and polishing the chips. The shear plane angle is then given by the famous shear plane model developed by Oxley and Welsh in [21].

$$\tan \phi = \frac{\cos \alpha}{\frac{a_{ch}}{a_c} - \sin \alpha} \tag{4.18}$$

Using the above model, fracture toughness G_c could be measured from the experimental data. In Equation 4.20 $(\frac{F_c}{w} - \frac{F_t}{w} \tan \phi)$ vs $(\frac{a_c}{2})(\tan \phi + \frac{1}{\tan \phi})$ gives a linear plot with Y-intercept giving the fracture toughness or critical energy release rate G_c. The slope of the curve gives yield stress as per Tresca criterion, however determining stress from William's model is not a purpose of this work.

Patel et. al [71] considered that effect of friction at tool-workpiece interface is already captured in this model through direct measurement of cutting and transverse force. They showed that in case of zero friction and no adhesion at tool work piece

interface the shear plane angle is given by:

$$\tan\phi = \frac{cos\alpha}{1 - sin\alpha} \tag{4.19}$$

The Equation. 4.19 on comparing with Equation. 4.18 corresponds to $a_{ch} = a_c$. Hence it could be concluded that the change in chip thickness after material separation is an effect of friction forces and it effects the shear plane angle formed.

4.2 Calculation: Fracture Toughness for Aluminum A2024 using William's model

In order to use William's model for determining fracture toughness of a material, we need data which is carefully obtained from machining experiments. Since no experiments were done in this work, the data for machining is adopted from work done by Kobayashi et. al. [93] for Fracture toughness calculation of Aluminum A2024. It is difficult to obtain consistent and accurate cutting forces and shear plane angles (from chip deformation ratio), from machining experiments [94]. Kobayashi et. al. [93] investigated orthogonal machining tests at various cutting speeds, rake angle and feeds for steel and Aluminum alloys and correlated metal cutting data with compression data in which they used distortion energy theory for ductile materials.

$$\left(\frac{F_c}{w} - \frac{F_t}{w}\tan\phi\right) = \frac{\sigma_y a_c}{2}\left(\tan\phi + \frac{1}{\tan\phi}\right) + G_c \tag{4.20}$$

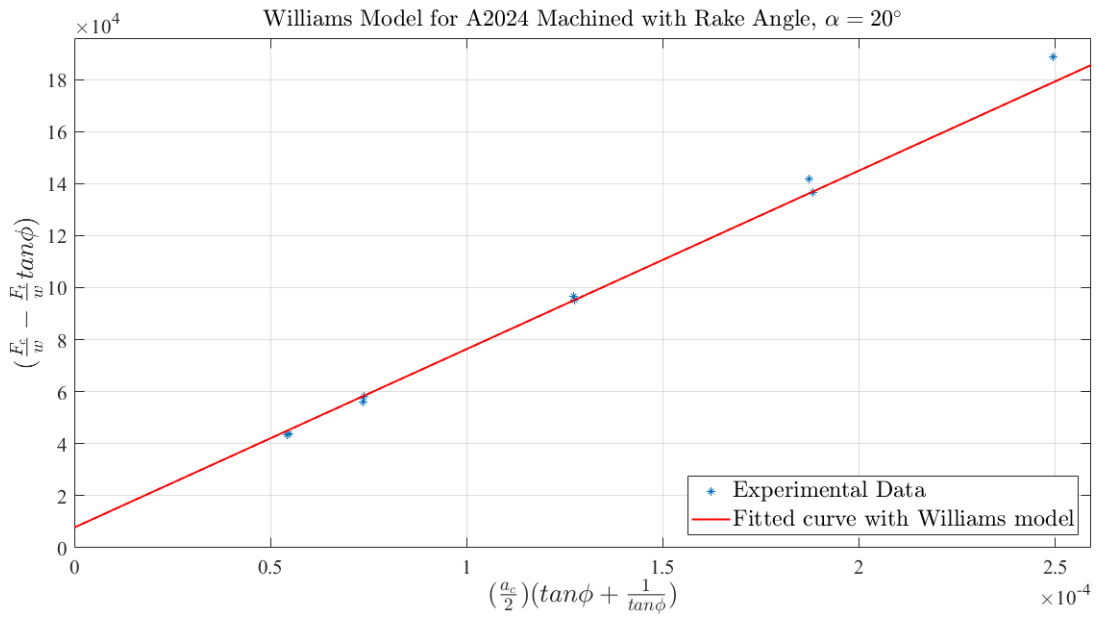

Figure 4.4: $(\frac{F_c}{w} - \frac{F_t}{w}\tan\phi)$ vs $(\frac{a_c}{2})(\tan\phi + \frac{1}{\tan\phi})$ plot for Aluminum alloy A2024 machined at rake angle, $\alpha = 20°$

Table 4.1: Machining data for orthogonal cutting of Aluminum alloy A2024 for rake angle 20°

Run no.	α (Rad)	F_c (N)	F_t (N)	a_c (mm)	$\frac{a_c}{a_{ch}}$	ϕ (rad)
999	0.35	275.78974	80.06799	$50.546e^{-3}$	0.571	0.58818
1000	0.35	275.78974	80.06799	$50.546e^{-3}$	0.583	0.60039
1007	0.35	342.51306	80.06799	$69.850e^{-3}$	0.606	0.62308
1008	0.35	346.96128	71.17155	$69.850e^{-3}$	0.602	0.61959
1001	0.35	529.33837	48.93044	$124.206e^{-3}$	0.659	0.67370
1002	0.35	524.89015	53.37866	$124.206e^{-3}$	0.655	0.67021
1003	0.35	720.61190	0.00000	$186.690e^{-3}$	0.737	0.74526
1004	0.35	698.37079	4.44822	$186.690e^{-3}$	0.711	0.72257
1006	0.35	911.88543	-44.48222	$249.174e^{-3}$	0.810	0.80634

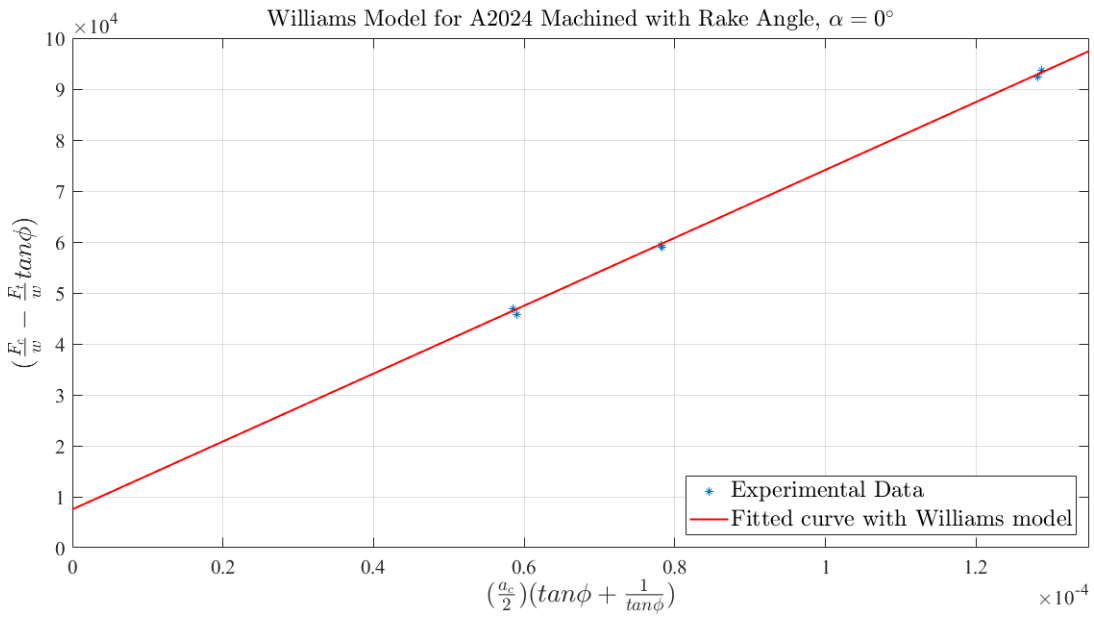

Figure 4.5: $(\frac{F_c}{w} - \frac{F_t}{w}\tan\phi)$ vs $(\frac{a_c}{2})(\tan\phi + \frac{1}{\tan\phi})$ plot for Aluminum alloy A2024 machined at rake angle , $\alpha = 0°$

Table 4.2: Machining data for orthogonal cutting of Aluminum alloy A2024 for rake angle 0°

Run no.	α (Rad)	F_c (N)	F_t (N)	a_c (mm)	$\frac{a_c}{a_{ch}}$	ϕ (rad)
997.00	0.00	320.27196	155.68776	50.54600	0.56500	0.51487
998.00	0.00	324.72018	151.23953	$50.546e^{-3}$	0.57500	0.52185
994.00	0.00	400.33994	160.13598	$69.85e^{-3}$	0.61800	0.55327
995.00	0.00	400.33994	164.58420	$69.85e^{-3}$	0.61600	0.55152
993.00	0.00	618.30280	186.82531	$124.206e^{-3}$	0.76500	0.65275
996.00	0.00	618.30280	191.27353	$124.206e^{-3}$	0.77800	0.66148

The cutting data for orthogonal machining of A2024 at various uncut chip thickness conducted by Kobayashi et. al. using a tool of rake angle, $\alpha = 20°$ is tabulated in Table. 4.1. Similarly, from the cutting test data for orthogonal machining of A2024 using a tool with rake angle, $\alpha = 0°$ is tabulated in Table. 4.2.

Using these data in Equation. 4.20 from William's model and plotting ($\frac{F_c}{w} - \frac{F_t}{w}\tan\phi$) vs ($\frac{a_c}{2}$)($\tan\phi + \frac{1}{\tan\phi}$) in MATLAB, gives a linear plot with Y-intercept giving the value for fracture toughness of A2024 as shown in Figure. 4.4 and 4.5. The value of fracture Toughness obtained for Aluminum alloy A2024 at rake angle $\alpha = 20°$ $G_c = 7782 J/m^2$ and at rake angle $\alpha = 0°$ $G_c = 7534$ J/m^2.

Patel et. al. [2] considered cutting test data of Aluminum A2024 for rake angle, α ranging from 5° to 40° from [95]. The Fracture toughness determined for A2024, using William's model for each rake angle is tabulated in Table. 4.3. They concluded that G_c is virtually constant over the whole range of rake angle, α and its value is $G_c = 7600$ J/m^2 which is close to the fracture calculated in this work. A constant value of energy required to generate new surfaces G_c for all rake angles make it a favorable candidate for chip separation criterion in finite element simulations.

Table 4.3: Fracture Toughness measured by Patel et. al. in [2] for A2024.

α (Deg)	5	10	15	20	25	30	35	40
G_c(J/m^2)	8450	8540	8240	8510	5090	6420	8630	6670

Since no experimental method is yet available for determining G_f^{serr}, in this work, a series of values for G_f^{serr} are used until the the numerical results are in agreement with the experimental observations. In addition, the appropriateness of linear and exponential Hillerborg exponential models for chip separation and serration is also studied. Both these aspects are discussed in next chapter.

4.3 Assumptions and Approximations in determining fracture energy from machining test methods

It should be noted that Atkins model is yet a simple model and have considered lot of assumptions such as constant coefficient of friction. Moreover, he did not consider the effects of tool edge radius which significantly affects friction and gives rise to ploughing forces while cutting. Karpat in [96] considered effect of the cutting tool

edge radius and included it in the Atkins model to study its influence on material separation and fracture energy. As Atkins model showed that material shear yield stress and fracture energy can be calculated as a function of uncut chip thickness, Karpat modified this solution methodology to include cutting tool edge radius as well. Astakhoov et. al. proposed an approach to calculate cutting force based on the model of energy partition according to which the cutting power was partitioned into four major parts: Power spent on plastic deformation of the material being removed, power spent on tool-chip interface, power spent on tool-workpiece interface and power spent on formation of new surfaces.

CHAPTER 5: DAMAGE MODELS FOR CHIP SEPARATION AND SERRATION

5.1 Selection of damage model

Chip separation and chip serration are two phenomenon resulting from two different damage mechanisms. The mechanism of serrated chip formation is different from chip separation and both are not well understood. Previous attempts to investigate serrated chip formation mechanisms led to various theories explaining the transition of chip shape from continuous to serrated before fracture. The adiabatic shear instability theory proposed by Cook et. al. [97] for the serrated chip formation states that serrated chip is due to thermoplastic instability occurring within the primary shear zone. Such an instability can occur when thermal softening dominates hardening and ultimately results in adiabatic shear band formation. Another theory that explains serrated chip formation is periodic formation of cracks which initiate from the free surface of the chip and propagate towards tool tip. Wang and Liu [91], based on the observations of chip micro-structure under high magnification electron microscope showed that both adiabatic stress and periodic crack theory are insufficient to explain the serrated chip formation process and lacked generality. They proposed in [91] that serrated chips are formed as a result of mixed mode ductile fracture and adiabatic shear localization. The damage evolution in serrated chips is due to many factors such as void coalescence, crack propagation and fusing due to uniformly distributed stress and high temperatures [98]. Thermal softening in adiabatic shear bands decreases damage evolution rate, slows down the crack propagation by increasing ductility and thereby increasing fracture toughness of the material. Clearly, the models for chip separation and chip serration need to be such that these mechanisms that influence damage evolution are taken into account.

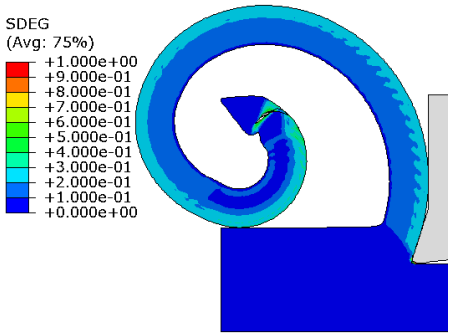

Figure 5.1: Linear Damage model for chip separation and serration; $V_c = 800$ m/min.

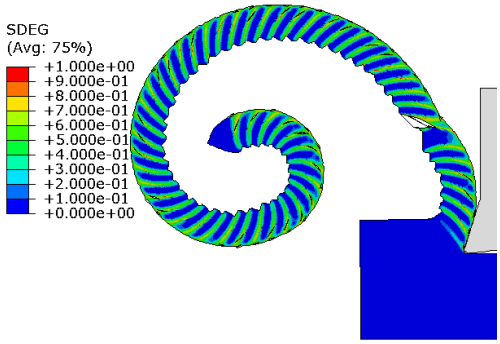

Figure 5.2: Linear damage model for chip separation and exponential damage model for chip serration; $V_c = 800$ m/min.

In this section an appropriate damage model for each mechanism is identified by comparing the numerical results with experimental results. Two forms of Hillerborg's fracture models, as shown in Fig 3.16a and Fig. 3.17a namely linear and exponential are available in Abaqus for modeling damage evolution. In order to study the effect of the choice of damage evolution laws for chip separation and chip serration, it is assumed that $G_f^{sep} = 8000$ J/m^2, $G_f^{serr} = 18000$ J/m^2 and $V_c = 800$ m/min.

The results indicate that when a linear damage model for chip separation (G_f^{sep}) and an exponential damage model for chip serration (G_f^{serr}) are assumed, the results for chip morphology, cutting force and other field variables are in agreement with experimental results in [82] as shown in Figures. **??**, 5.3, 5.4, 5.2 and 5.7.

In this work, area under the curve $\sigma(\bar{u})$, which represents critical energy release

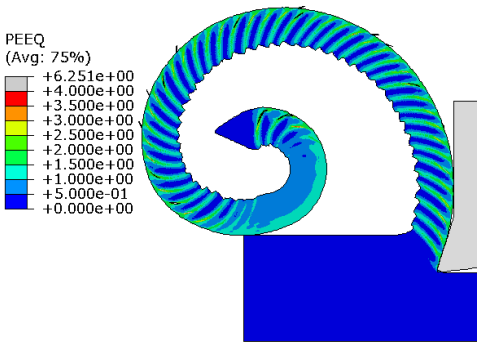

Figure 5.3: Equivalent plastic strain $V_c = 200$ m/min.

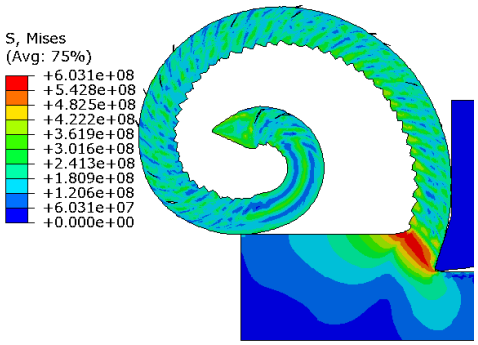

Figure 5.4: Effective stress (Mises stress); $V_c = 200$ m/min.

rate is used as criterion for chip separation (G_f^{sep}) and chip serration (G_f^{serr}). Both the models differ in terms of damage evolution as shown in Fig. 3.16b and Fig. 3.17b, where the slope of the curve gives stiffness degradation rate w.r.t the change in equivalent plastic displacement, $\bar{u}$. It should be noted that the slope is constant in linear model whereas it is varying in exponential model for a given value of equivalent plastic displacement, $\bar{u}$.

In the exponential model, initially the rate of stiffness degradation (slope) is high and decreases gradually. The damage evolution curve asymptotically approaches $D = 1$. This behavior is appropriate for simulating adiabatic shear localization. The elements of G_f^{serr} assigned with exponential damage model, loses considerable stiffness initially, thereby undergoing severe plastic deformation that increases temperature. Following this, the stiffness degradation rate in the elements decreases as the damage

parameter approaches 1 and hence the damage evolution is decreased resulting in increased ductile behaviour. Such a mechanism results in adiabatic shear localization and chip serration is observed in numerical results as shown in Fig. 5.2. At ultra high cutting speeds or uncut chip thickness or lower rake angles, sufficient external energy is available to satisfy the criterion G_f^{serr} and initiate fracture form the chip free surface as shown in Figs 5.2, 5.10 and 5.13. The serration and fracture behavior observed in these figures are consistent with the observations made in [91] and [98].

The usage of a linear damage model for chip serration G_f^{serr} resulted in continuous chip morphology as shown in Fig. 5.1 even at high cutting speeds. This is due to the constant stiffness degradation rate of the linear model and therefore, adiabatic shear localization cannot be achieved. Since experiments show that serrated chips are observed for high cutting speeds, linear damage model for chip serration is therefore considered to be inappropriate.

On the other hand, for chip separation, an exponential damage law is not appropriate for two reasons: (a). shear localization has not been observed in the workpiece material ahead of the tool-tip, and (b). element deletion occurs when $D = 1$ with the exponential damage law. However, the elements ahead of the cutting tool deform significantly much before $D = 1$ is reached and consequently, severe element distortions and convergence issues occur. With the linear damage model, D attains a value of one much before severe element distortions occur and therefore, the chip separation process can be modeled without convergence issues.

5.2 Determination of threshold value for G_f^{serr}

Based on the results from the previous section, a linear damage evolution in chip separation and an exponential damage evolution in chip serration are assumed in the following. The threshold value for G_f^{sep} is taken from experiments as mentioned earlier. In general, the threshold value for G_f^{serr} will be higher than G_f^{sep} since localization leads to increased ductility in the shear bands and therefore, $\bar{u}_f$ will be higher in the

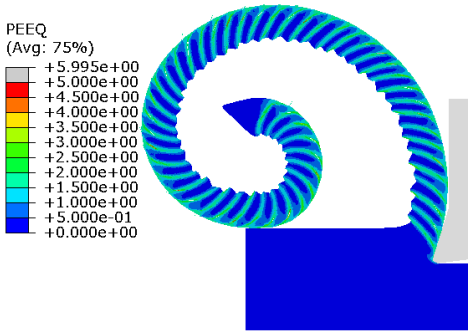

Figure 5.5: $V_c = 200$ m/min; $G_f^{sep} = 8000$ J/m^2; $G_f^{serr} = 18000$ J/m^2.

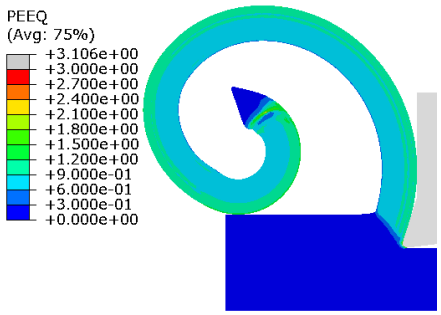

Figure 5.6: $V_c = 200$ m/min; $G_f^{sep} = 8000$ J/m^2; $G_f^{serr} = 25000$ J/m^2.

chip from that ahead of the cutting tool. However, a precise estimate for G_f^{serr} is not yet available from experiments. Therefore, in the following, the effect of variation of G_f^{serr} for a fixed $G_f^{sep} = 8000$ J/m^2 is studied by considering three different cutting speeds $V_c = 200$ m/min, $V_c = 800$ m/min and $V_c = 1200$ m/min.

In case 1 with $G_f^{serr} = 18000$ J/m^2, our FE results show that the form of the chip was serrated for cutting speed $V_c = 200$ m/min, $V_c = 800$ m/min and $V_c = 1200$ m/min (Figs. 5.5, 5.7 and 5.10 respectively). The results show localization of plastic deformation in all the three cases with the maximum value of equivalent plastic strain ($\bar{\epsilon}$) occurring in the shear bands (in the chips) and increasing with V_c. Similarly, the damage and degree of serration also increased with increasing cutting speed V_c.

For case 2, on increasing the value of G_f^{serr} to $G_f^{serr} = 25000$ J/m^2, the chip shape for $V_c = 200$ m/min becomes continuous, as shown in Fig. 5.6. In addition, a considerable

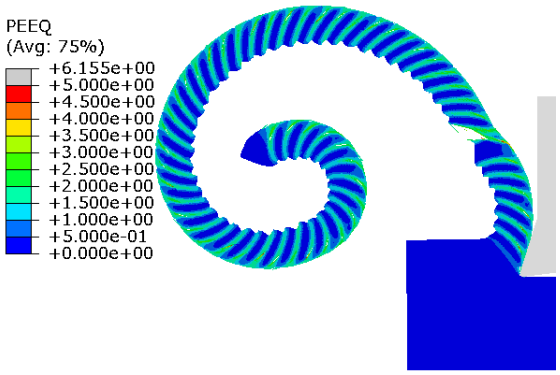

Figure 5.7: $V_c = 800\ m/min$; $G_f^{sep} = 8000$ J/m^2; $G_f^{serr} = 18000$ J/m^2.

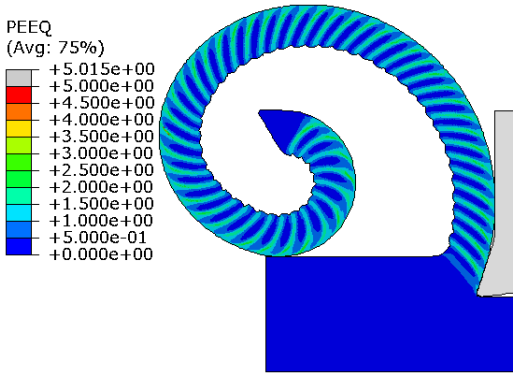

Figure 5.8: $V_c = 800$ m/min; $G_f^{sep} = 8000$ J/m^2; $G_f^{serr} = 25000$ J/m^2.

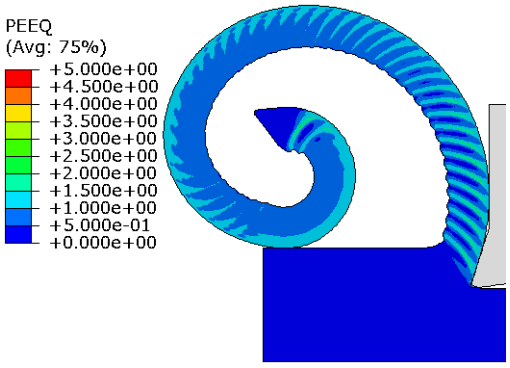

Figure 5.9: $V_c = 800$ m/min; $G_f^{sep} = 8000$ J/m^2; $G_f^{serr} = 28000$ J/m^2.

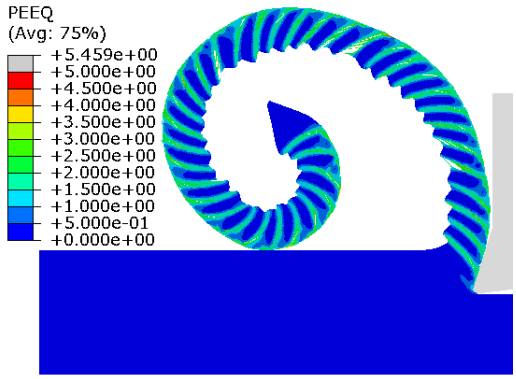

Figure 5.10: $V_c = 1200$ m/min; $G_f^{sep} = 8000$ J/m^2; $G_f^{serr} = 18000$ J/m^2.

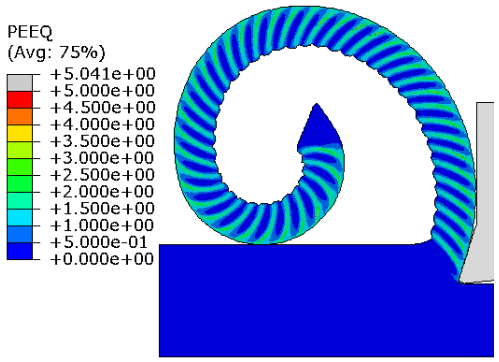

Figure 5.11: $V_c = 1200$ m/min; $G_f^{sep} = 8000$ J/m^2; $G_f^{serr} = 25000$ J/m^2.

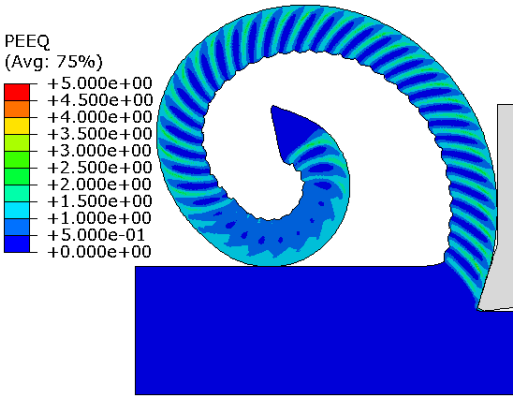

Figure 5.12: $V_c = 1200$ m/min; $G_f^{sep} = 8000$ J/m^2; $G_f^{serr} = 28000$ J/m^2.

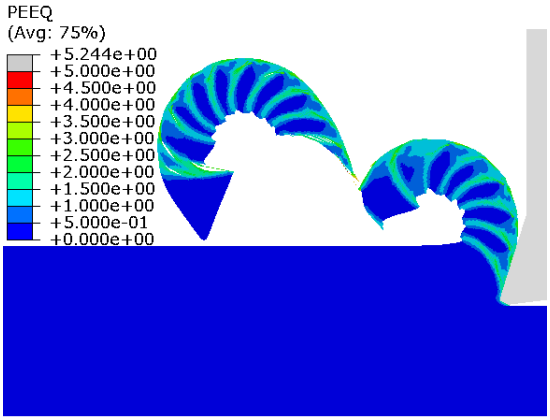

Figure 5.13: $V_c = 1200$ m/min; $G_f^{sep} = 5000$ J/m^2; $G_f^{serr} = 15000$ J/m^2.

reduction in $\bar{\epsilon}$ (< 0.9) within the chip and ≈ 1.3 near tool-chip interface is observed. The chips in case of $V_c = 800$ m/min (Fig. 5.8) and $V_c = 1200$ m/min (Fig. 5.11) are serrated. However, there is a considerable reduction in the degree of serration for both the speeds with $V_c = 1200$ m/min on the slightly higher side.

In case 3, $G_f^{serr} = 28000$ J/m^2 is considered for the two cases $V_c = 800$ m/min and $V_c = 1200$ m/min as shown in Fig. 5.9 and Fig. 5.12 respectively. The chip shape transitioned from serrated to continuous in $V_c = 800$ m/min. However, the chip shape for $V_c = 1200$ m/min is still serrated with a considerable reduction in the degree of serration. The equivalent plastic strain is scattered in the entire chip for $V_c = 800$ m/min and its maximum value decreased to $\bar{\epsilon} = 3.22$ with partial shear band formation. For $V_c = 1200$ m/min, the strain and damage localization are much higher compared to $V_c = 800$ m/min. The degree of serration, shear bands and maximum value of equivalent plastic strain ($\bar{\epsilon} = 3.86$) reduced significantly for both the speeds as compared to case 2.

The observations of this section can be explained based on the fact that a higher value of G_f^{serr} used as Hillerborg's fracture energy physically indicates higher fracture toughness of chip and so it requires higher energy per unit area for the process of serration to crack initiation and propagation to chip breakage. This energy is available

from external work done by the cutting tool. Hence at low cutting speeds, the energy available to chip is not enough for serration or creating new surfaces. For high speeds such as 800 m/min or 1200 m/min, more energy is available and therefore, chip breakage is possible as confirmed in Fig. 5.13.

CHAPTER 6: VALIDATION AND VERIFICATION

In this chapter, the results obtained from finite element simulation of orthogonal machining of A2024-T351 are validated with experimental results available in literature. Based on the results discussed in section 5.1 for selection of damage model, a linear damage evolution model is used for modeling chip separation (G_f^{sep}) and an exponential damage model is used for chip serration (G_f^{serr}). Moreover, the value of critical energy release rate which is used as criterion for chip breakage (G_f^{serr}) is chosen between 18000 J/m^2 to 18500 J/m^2. The chosen value of G_f^{serr} is based on the results from parametric study undertaken for choice of G_f^{serr} in section 5.2. The value of critical energy release rate for chip separation, as calculated using William's model G_f^{sep} is equal to 8000 J/m^2.

6.1 Cutting force correlation

Mabrouki et. al. in [82] experimentally measured cutting force F_c for orthogonal machining of A2024-T351 for the following cutting parameters: cutting speed V_c = 200m/min, uncut chip thickness (feed), a_c = 0.4mm, tool rake angle $\alpha = 17.5^\circ$ and depth of cut w = 4mm. The cutting force obtained from finite element simulation of orthogonal machining of A2024-T351 for similar parameters is shown in Fig. 6.1. The average value of cutting force obtained numerically is $\approx$ 943N which is close to the experimental results presented in [82].

Mabrouki also presented experimentally measured average cutting force for other cutting parameters in [99]. Madag and Piska also presented experimentally measured average value of cutting force for orthogonal machining of A2024-T351 aluminum alloy for similar parameters [100]. They conducted cutting experiments at uncut chip

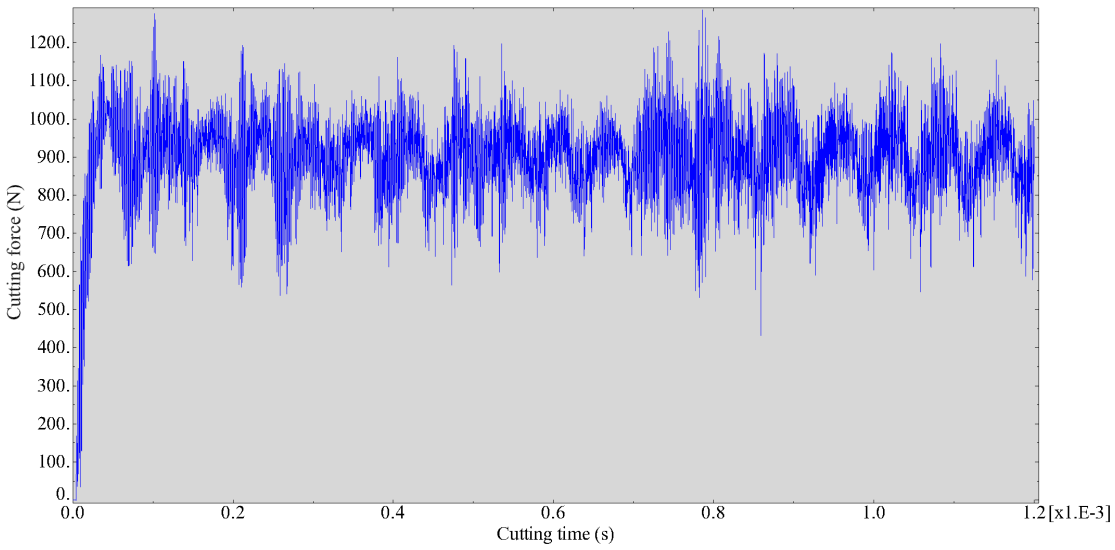

Figure 6.1: Comparison of cutting force F_c with experimental results

thickness $a_c = 0.4$mm for similar tool rake angle and velocities as that chosen by Mabrouki et. al. Madag and Piska compared experimental results with numerical results (SPH) and presented them at the 14^{th} CIRP conference on Modeling of machining operations (CIRP CMMO). A comparison of average cutting force obtained experimentally or numerically is presented in Fig. 6.2a. The numerical results shows a close agreement with experimental result for average cutting force. The Fig. 6.2b shows that the error between experimental and numerical result is less than 10%. A negative error indicates an underestimation of cutting force by FEA as compared to experimental results. A possible explanation for such result is due to the material response modeled by Johnson-Cook constitutive model. The selected parameters for Johnson-cook model could underestimate the sensitivity of work-hardening due to high strain rates in workpiece material. In addition, there are many other factors such as friction modeling which can affect the cutting force in finite element simulation.

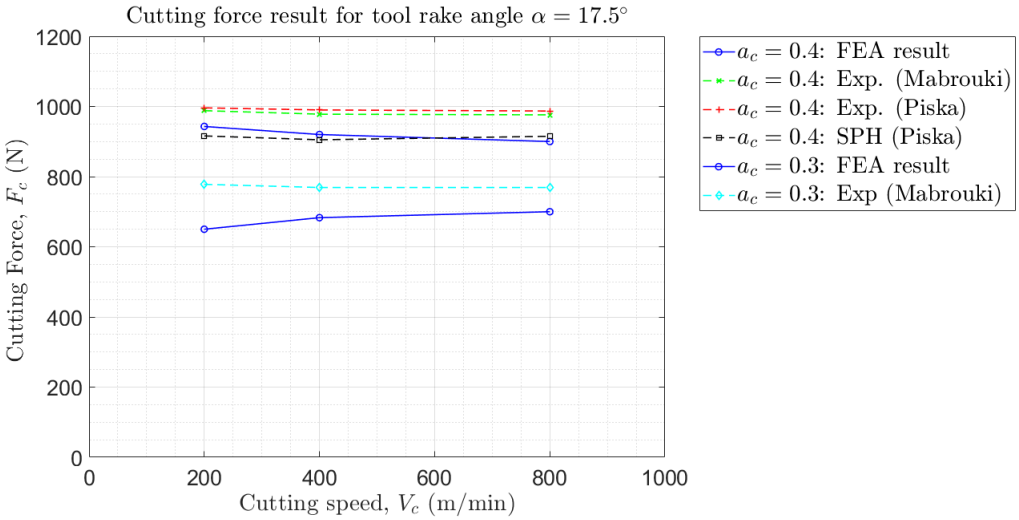

(a) Comparison of average cutting force with numerical and experimental results

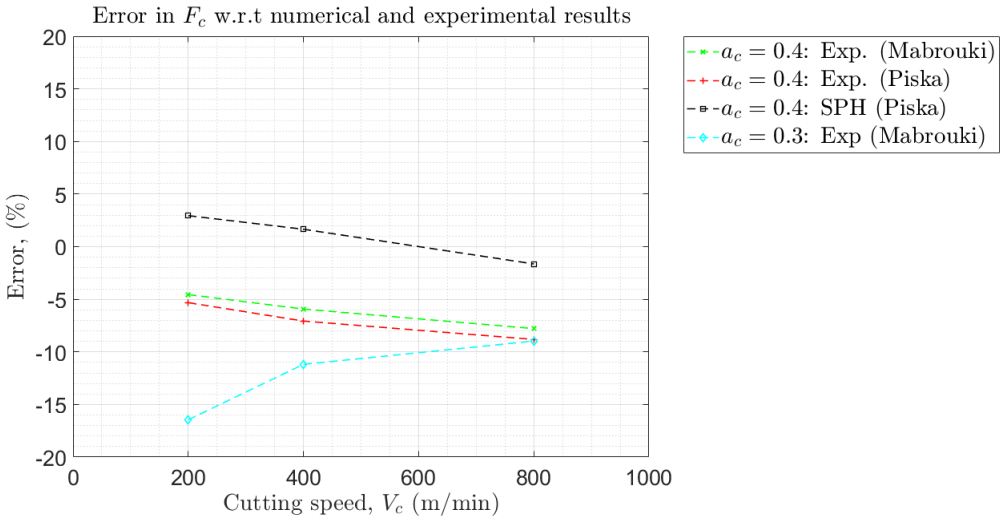

(b) Error in average cutting force

Figure 6.2: Comparison of average F_c with experimental results

Determination of average cutting force from machining experiments for rake angle $\alpha = 0°$ were undertaken by various other researchers for A2024-T3. Daoud et. al. in [101] and Atlati et. al. in [102] conducted experimental study of machining aluminum alloys with various rake angles for a depth of cut $w = 3.14$mm and $w = 4$mm respectively. These experiments were conducted for a range of uncut chip thickness from $a_c = 0.07$mm to $a_c = 0.31$mm and cutting speed varying from $V_c =$

363m/min to $V_c = 1539$m/min. The table 6.1 compares cutting force results obtained from FEA with experiments for Rake angle $\alpha = 0°$. The terms in table table 6.1 with superscript "EXP" represents experimental data from the cited reference in column 1 where as the terms with a superscript "FEA" represents parameter and result from Finite element simulations conducted in this work.

Table 6.1: Correlation of cutting force with experimental results for machining with $\alpha = 0°$

Reference	V_c^{EXP} (m/min)	V_c^{FEA} (m/min)	a_c^{EXP} (mm)	a_c^{FEA} (mm)	F_c^{EXP} (N)	F_c^{FEA} (N)	w (mm)
[101]	387	400	0.25	0.2	581.1	438	3.14
[101]	399	400	0.31	0.3	650.1	626	3.14
[101]	951	800	0.16	0.2	424.2	446	3.14
[101]	963	800	0.25	0.3	564.9	590	3.14
[102]	195	200	0.1	0.2	430	580	4
[102]	390	400	0.1	0.2	405	558	4

The FEA results presented in this section are in close agreement with experimental results. The experimental results indicate that, the cutting force increases with increase in uncut chip thickness or decrease in rake angle. Such a trend in cut force is clearly reflected in FEA results presented in this section.

6.2 Chip morphology correlation

The chip shape obtained as a result of metal cutting depends on the cutting parameters chosen. For instance, a large uncut chip thickness (feed) or a low rake angle results into serrated chips. Moreover, at a very high cutting speed, the chip shape is serrated. Chip breakage is a phenomenon which occurs when parameters producing serrated chips are pushed towards extremities. Figure 6.3 shows that the chip shape obtained from FEA results matches closely with the physical chip shape obtained

from cutting experiments. Figure 6.3a and 6.3b shows chip shape obtained from finite element simulation of orthogonal machining of A2024-T351. These chip shapes are comparable with high magnification image of physical chip presented by Mabrouki et. al. in [82]. It should be noted that the cutting parameters for both the physical chip and the chip shape obtained from finite element simulation are exactly same. Figure 6.3c shows chip shape obtained from orthogonal machining of A2024-T3 with a tool of $\alpha = 0^{\circ}$. The chip shape matches with the physical chip presented by Daoud et. al. in [101].

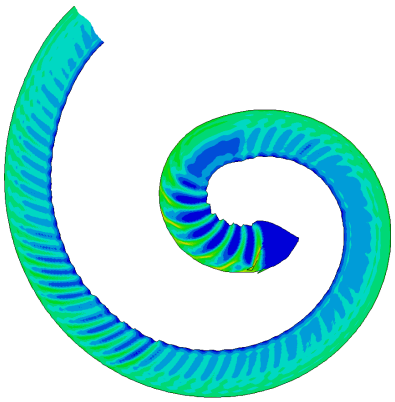

(a) Chip morphology from FEA result for $a_c = 0.4$mm; $\alpha = 17.5°$; $V_c = 200$m/min

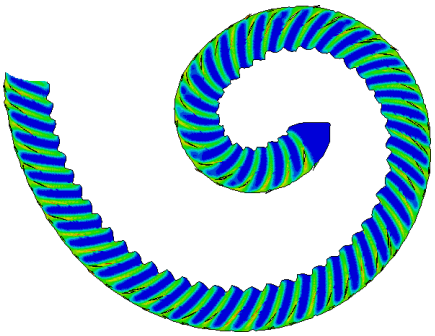

(b) Chip morphology from FEA result for $a_c = 0.4$mm; $\alpha = 17.5°$; $V_c = 800$m/min

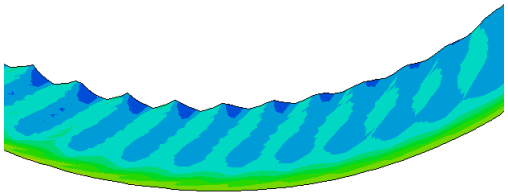

(c) Chip morphology from FEA result for $a_c = 0.2$mm; $\alpha = 0°$; $V_c = 400$m/min

Figure 6.3: Comparison of chip shapes obtained from FEA simulations with experimental results

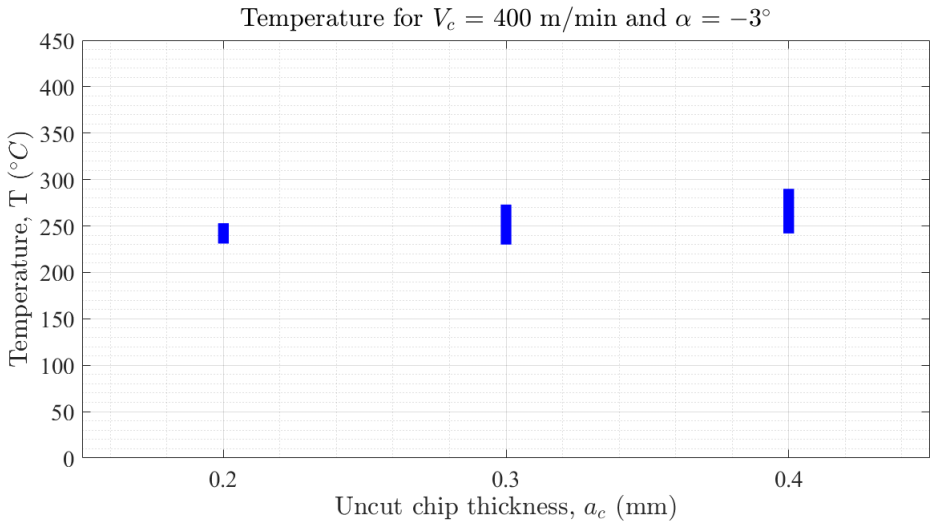

Figure 6.4: Temperature at tool-chip interface obtained from finite element results

6.3 Temperature correlation

In machining operations, mechanical work is converted to heat the plastic deformation involved in chip formation and through friction between the tool and workpiece. Experimental measurement of temperatures in literature shows that high temperatures are observed at tool chip interface due to friction and heat conduction to the cutting tools [103]. Stephenson et. al experimentally measured temperatures at tool chip interface during orthogonal machining (turning) of aluminum alloy A2024 in [103]. They used tool-work thermocouple method to measure average interfacial temperature. Moreover, the thermocouple circuit was insulated from machining tool using a bakelite tool holder and calibrated using the torch method.

The tool used for machining A2024 had side rake, back rake and lead angle of $-5°$, $0°$ and $10°$ respectively. The cutting speed V_c = 365.1 m/min and feed of 0.165 mm/rev was used in their experiment. Their result shows that the interfacial temperature ranges from 200°C to 450°C.

The temperature range obtained from finite element (FE) simulations of orthogonal machining of A2024 are shown in fig. 6.4. The results are presented for cutting speed,

$V_c = 400$ m/min and tool rake angle, $\alpha = -3^\circ$ for various uncut chip thickness. The cutting parameters are not exactly same as what used by Stephenson et. al. in their experiments. However, the closest set of parameters is chosen for comparison between finite element simulation and experimental results. The range of temperature predicted by FE simulations at tool - chip interface is in the same ball park region but little lower than the experimental results.

The table 6.2 shows comparison of FEA results for temperature with experimental results presented by Daoud in [101].

Table 6.2: Comparison of temperature with experimental results for machining with tool rake angle, $\alpha = 0^\circ$

Reference	V_c^{EXP} (m/min)	V_c^{FEA} (m/min)	a_c^{EXP} (mm)	a_c^{FEA} (mm)	T^{EXP} (N)	T^{FEA} (N)	w (mm)
[101]	387	400	0.25	0.2	323.5	249	3.14
[101]	399	400	0.31	0.3	220.3	262	3.14
[101]	951	800	0.16	0.2	282.4	268	3.14
[101]	963	800	0.25	0.3	256.5	289	3.14

CHAPTER 7: DISCUSSION OF THE RESULTS

The previous chapters discussed various aspects of the finite element modeling for orthogonal machining of A2024-T351 by considering it as a problem of fracture mechanics. Johnson-Cook damage model was used to account for damage initiation. whereas for modeling damage evolution, the Hillerborg fracture model coupled with JC-damage model is used [87]. Based on results from section 5.1 a linear damage model was used for simulating chip separation and an exponential damage model was used for simulating chip serration. Critical energy release rate which represents area under the $\bar{\sigma}$ vs $\bar{u}$ curve in the Hillerborg fracture model was used as a criteria for chip separation and chip serration or breakage. The threshold value for modeling chip separation as calculated using William's model $G_f^{sep} = 8000$ J/m^2 was used where as the threshold value for modeling chip serration and breakage $G_f^{serr} \approx 18000$ to 18500 J/m^2 was used (refer section 5.2).

The Johnson-Cook constitutive model was used for simulating thermo-visco-elasto-plastic response of workpiece material. The tool - chip interaction was simulated using Zorev's stick-slip friction model. In this model, the friction stress in slip zone was modeled using a stress based friction model instead of conventional approach of using a coulomb's friction model.

Various parameters considered for analyzing orthogonal machining process using finite element method are presented in table 7.1. Various results obtained from this parametric study are discussed in this chapter.

Table 7.1: Parametric study for orthogonal machining of A2024-T251

Rake angle, $\alpha = -3°$, $\alpha = 0°$, $\alpha = 17.5°$			
uncut chip thickness, a_c	cutting speed, V_c		
0.4	200	400	800
0.3	200	400	800
0.2	200	400	800

7.1 Chip morphology

Fig. 7.1 displays various types of chip shapes obtained from machining of A2024-T351 using various cutting parameters. The results presented here for chip morphology indicates that the chip obtained from machining of A2024-T351 could be broadly categorized into two types: a). Continuous (Smooth) chip b). serrated (or segmented) chip.

A continuous chip is obtained when machining operation is undertaken using decent cutting parameters such as a low uncut chip thickness, a_c, a low cutting speed, V_c along with using a positive tool rake angle, α. When the cutting parameters are pushed towards extreme limits such as increasing the cutting speed or uncut chip thickness and reducing the tool rake angle, the chip shape gradually transits from continuous to serrated. Such a behavior is well reflected in the results presented in fig. 7.1. For instance, The chip shape with $\alpha = 17.5°$ is continuous when $a_c = 0.3$ mm and $V_c = 200$ m/min. However, when α is reduced to $0°$ or $-3°$ the chip shape obtained is serrated. It is observed that for high cutting speeds and uncut chip thickness, the serrated chip tends to break when tool rake angle is 0 or negative. The cutting parameters not only affects the chip shape locally but also governs the chip curl radius after it is separated from the bulk material. The complete chip shape could be observed in fore-coming sections presented in this chapter.

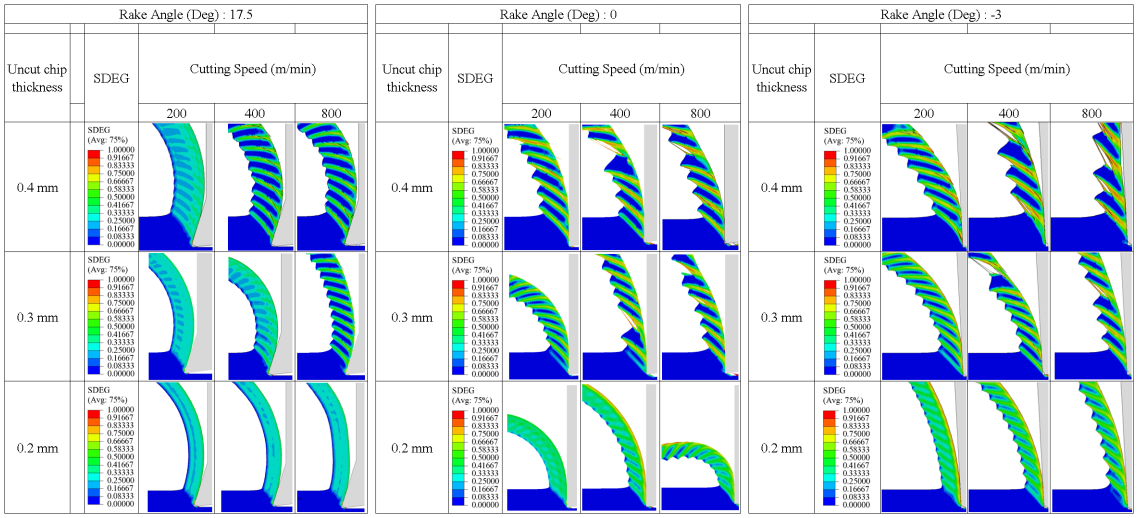

Figure 7.1: Chip morphology obtained from finite element simulation of orthogonal machining of A2024-T351

7.2 Equivalent plastic strain ($\bar{\epsilon}$) results

As discussed in previous chapter, the formation of serrated chips is explained by adiabatic shear localization and mixed mode ductile fracture. The equivalent plastic strain is an important field variable to govern such a mechanism. A high value of $\bar{\epsilon}$ results in adiabatic shear localization and ductile fracture. Moreover, the Hillerborg damage model used in this work for modeling chip separation and serration is based on equivalent plastic displacement which is directly related to equivalent plastic strain through the element characteristic length. This indicates that a higher value of $\bar{\epsilon}$ in chip means higher energy release rate is obtained which makes it a very important field variable in the process to satisfy chip separation and serration criteria. The equivalent plastic strain is given by

$$\bar{\epsilon} = \int_0^t \sqrt{\frac{2}{3}\dot{\epsilon}_{ij}^p \dot{\epsilon}_{ij}^p} dt \tag{7.1}$$

here, ϵ_{ij}^p are the components of plastic strain tensor.

The fig. 7.2 shows comparison of equivalent plastic strain (PEEQ) results obtained from FE simulation of machining using different tool rake angles. Similarly, the fig. 7.3 and 7.4 shows comparison of $\bar{\epsilon}$ for machining at different uncut chip thickness a_c and different cutting speed V_c respectively. The results for serrated chip shape indicate that there is localized adiabatic shear instability due to high plastic deformation. This leads to formation of shear bands where high value of $\bar{\epsilon}$ is observed. However, there is no shear band formation in case of continuous chip as shown in fig. 7.4c and fig. 7.3c and the value of $\bar{\epsilon}$ is low as compared to serrated chips because of low plastic deformation. Moreover, a high value of $\bar{\epsilon}$ is also observed at tool-chip interface zone due to friction. It is observed in the results that unlike serrated chips, the value of $\bar{\epsilon}$ in a continuous chip is uniform (constant) through out the chip except at tool -chip

interface zone, where its value is higher.

The fig. 7.5, fig. 7.6, fig. 7.7 and fig. 7.8 plots various $\bar{\epsilon}$ range in shear bands and tool - chip interface zone for various cutting parameters. The results indicate that for the cases where value of $\bar{\epsilon}$ is higher than 0.2 in chip, serrated chips are observed.

The value of $\bar{\epsilon}$ in shear bands increases with an increase in cutting speed, V_c or increase in uncut chip thickness, a_c or when the tool rake angle α is reduced. Such an increase in $\bar{\epsilon}$ results in adiabatic shear localization, leading to formation of serrated chips. The increase in degree of serration also follows similar trend.

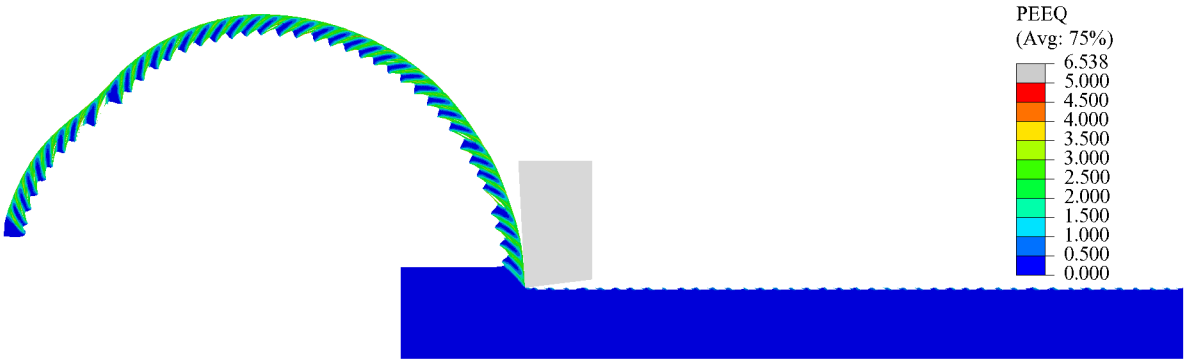

(a) PEEQ results for rake angle $\alpha = -3°$; $a_c = 0.3$ mm; $V_c = 800$ m/min

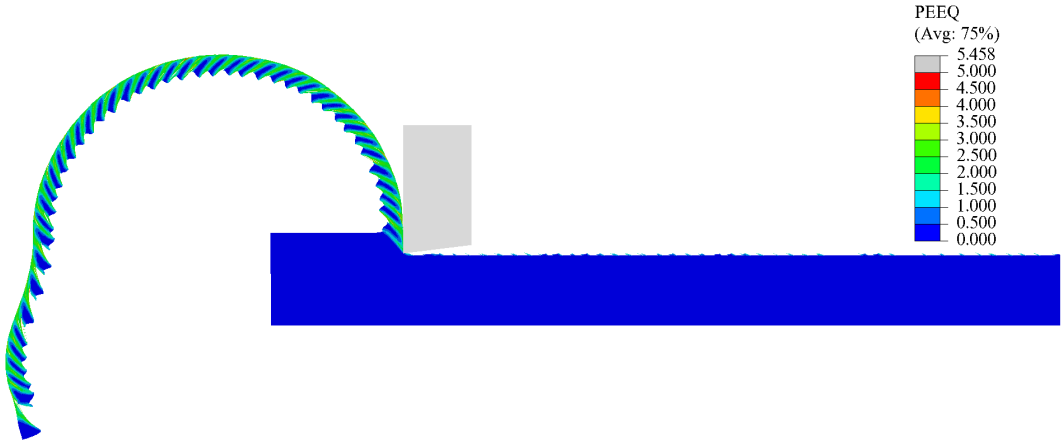

(b) PEEQ results for rake angle $\alpha = 0°$; $a_c = 0.3$ mm; $V_c = 800$ m/min

(c) PEEQ results for rake angle $\alpha = 17.5°$; $a_c = 0.3$ mm; $V_c = 800$ m/min

Figure 7.2: comparison of equivalent plastic strain results obtained from FE simulation of orthogonal machining conducted using various tool rake angles, α

(a) PEEQ results for uncut chip thickness $a_c = 0.4$ mm; $\alpha = 17.5°$; $V_c = 400$ m/min

(b) PEEQ results for uncut chip thickness $a_c = 0.3$ mm; $\alpha = 17.5°$; $V_c = 400$ m/min

(c) PEEQ results for uncut chip thickness $a_c = 0.2$ mm; $\alpha = 17.5°$; $V_c = 400$ m/min

Figure 7.3: comparison of equivalent plastic strain results obtained from FE simulation of orthogonal machining conducted for various uncut chip thickness, a_c

(a) PEEQ results for cutting speed $V_c = 800$ m/min; $\alpha = 17.5°$; $a_c = 0.3$ mm

(b) PEEQ results for cutting speed $V_c = 400$ m/min; $\alpha = 17.5°$; $a_c = 0.3$ mm

(c) PEEQ results for cutting speed $V_c = 200$ m/min; $\alpha = 17.5°$; $a_c = 0.3$ mm

Figure 7.4: comparison of equivalent plastic strain results obtained from FE simulation of orthogonal machining conducted for various cutting speeds, V_c

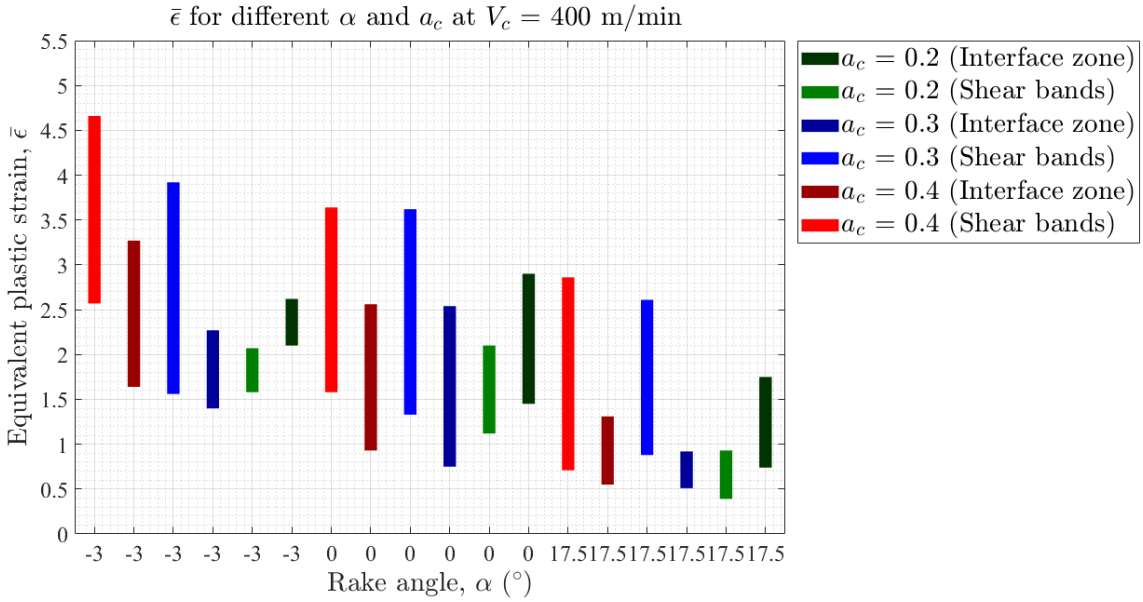

Figure 7.5: Equivalent plastic strain results obtained from FE simulation of orthogonal machining at cutting speed $V_c = 400$ m/min and various values of α and a_c

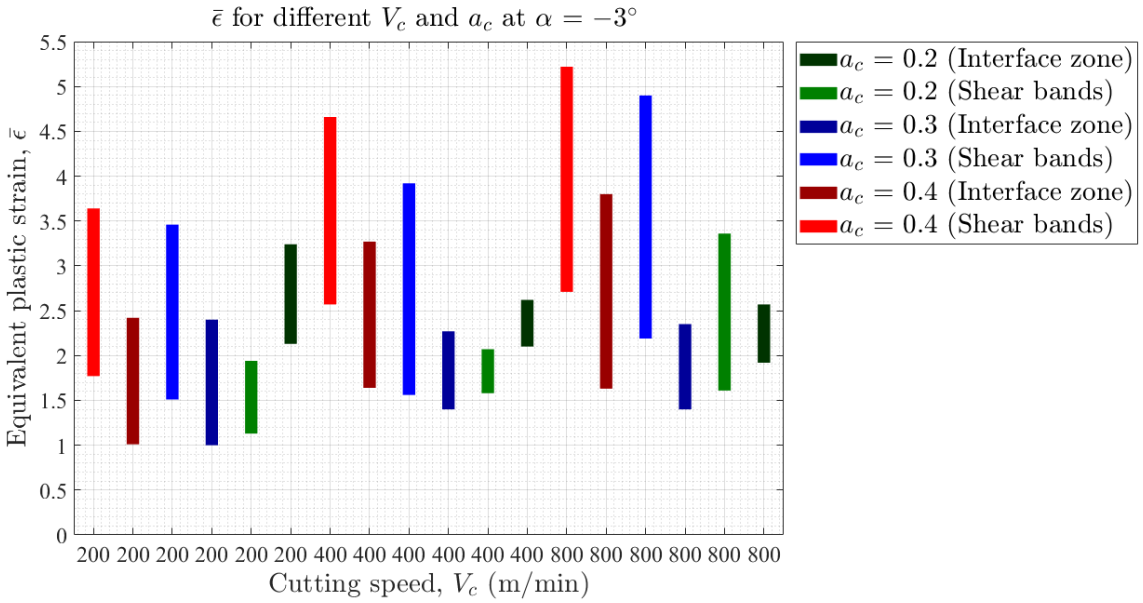

Figure 7.6: Equivalent plastic strain results obtained from FE simulation of orthogonal machining with tool rake angle $\alpha = -3°$ and various values of a_c and V_c

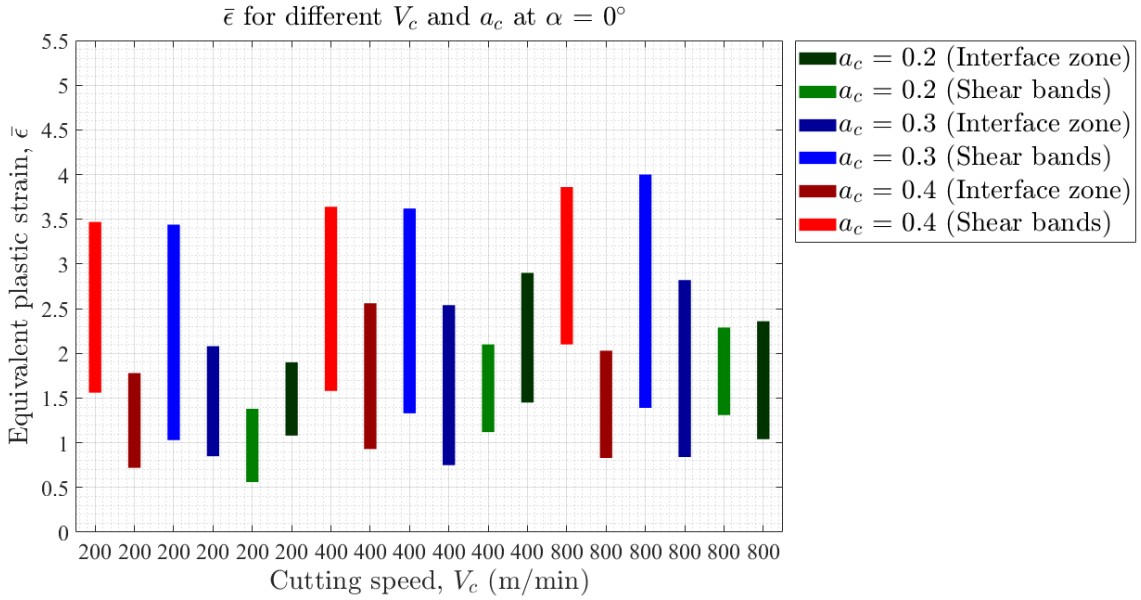

Figure 7.7: Equivalent plastic strain results obtained from FE simulation of orthogonal machining with tool rake angle $\alpha = 0°$ and various values of a_c and V_c

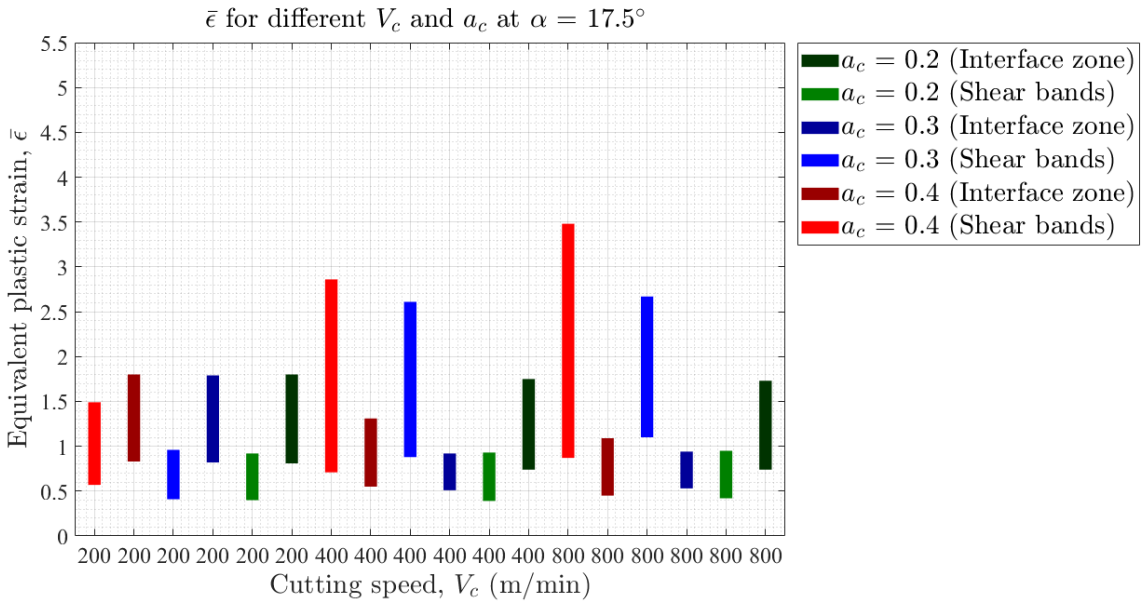

Figure 7.8: Equivalent plastic strain results obtained from FE simulation of orthogonal machining with tool rake angle $\alpha = 17.5°$ and various values of a_c and V_c

7.3 Equivalent stress ($\bar{\sigma}$)

In this work, Johson-Cook constitutive model is used which is based on mises yield criterion. Moreover, the criteria and fracture model for chip separation and serration depends on the curve of equivalent stress ($\bar{\sigma}$) vs equivalent displacement ($\bar{\epsilon}$). Therefore $\bar{\sigma}$ is also an important field variable to explain machining and various chip morphology. The equivalent stress or mises yield stress is given by

$$\bar{\sigma} = \sqrt{\frac{3}{2} S_{ij} S_{ij}} \tag{7.2}$$

here, S_{ij} are the components of deviatoric stress tensor.

The fig. 7.9, fig. 7.10 and fig. 7.11 compares equivalent stress for variation in tool rake angle (α), uncut chip thickness (a_c) and cutting velocity (V_c) respectively. These results indicate that in machining operation, highest stress is present in primary shear zone. As discussed earlier, the stress in primary shear zone is driven by competition between thermal softening and strain rate hardening.

When serrated chips are formed as shown in fig. 7.9, fig. 7.10 and fig. 7.11, the stress is shear bands is very low. However, It was observed that $\bar{\epsilon}$ was very high in these shear bands. High plastic deformation increases the temperature in shear bands resulting in thermal softening of the material and a low value of equivalent stress. Such a result with low flow stress and high equivalent plastic strains represents increase in ductility of the material locally. Consequently, adiabatic shear localization occurs to give serrated chips.

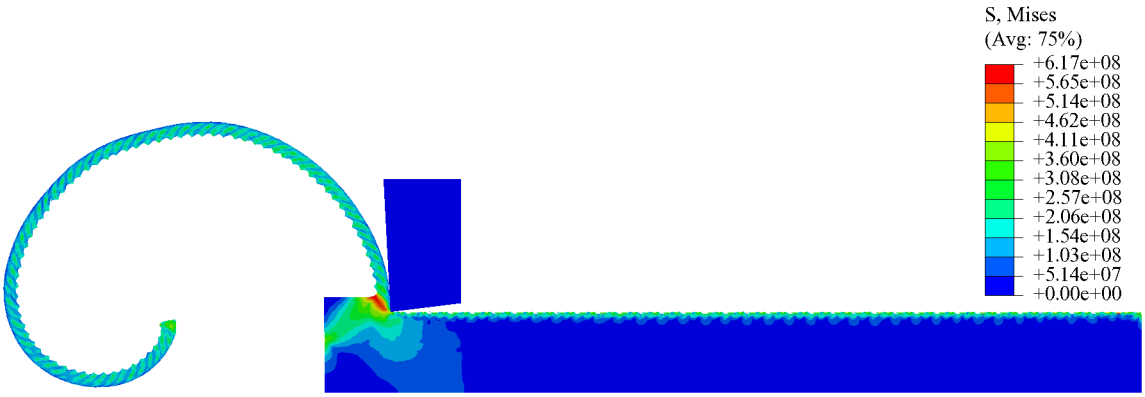

(a) equivalent stress results for rake angle $\alpha = -3°$; $a_c = 0.2$ mm; $V_c = 800$ m/min

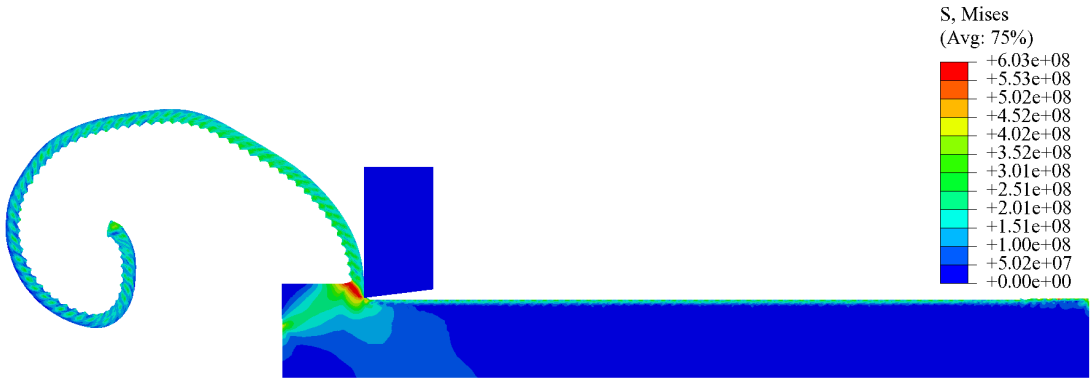

(b) equivalent stress results for rake angle $\alpha = 0°$; $a_c = 0.2$ mm; $V_c = 800$ m/min

(c) equivalent stress results for rake angle $\alpha = 17.5°$; $a_c = 0.2$ mm; $V_c = 800$ m/min

Figure 7.9: comparison of equivalent stress results obtained from FE simulation of orthogonal machining conducted using various tool rake angles, α

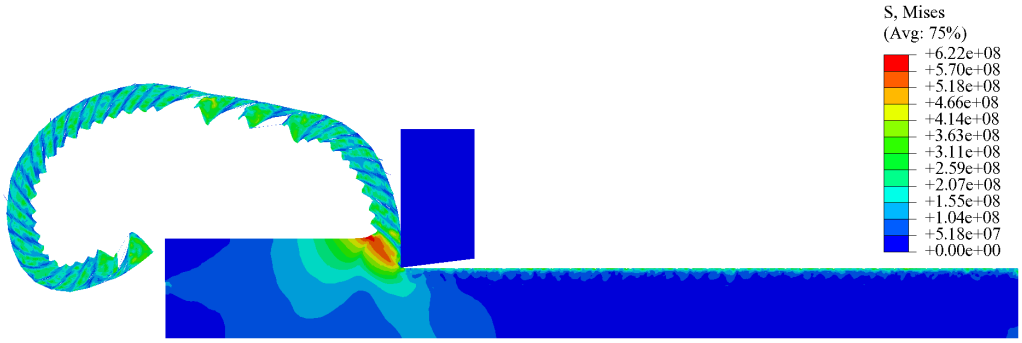

(a) equivalent stress results for uncut chip thickness $a_c = 0.4$ mm; $\alpha = 0°$; $V_c = 200$ m/min

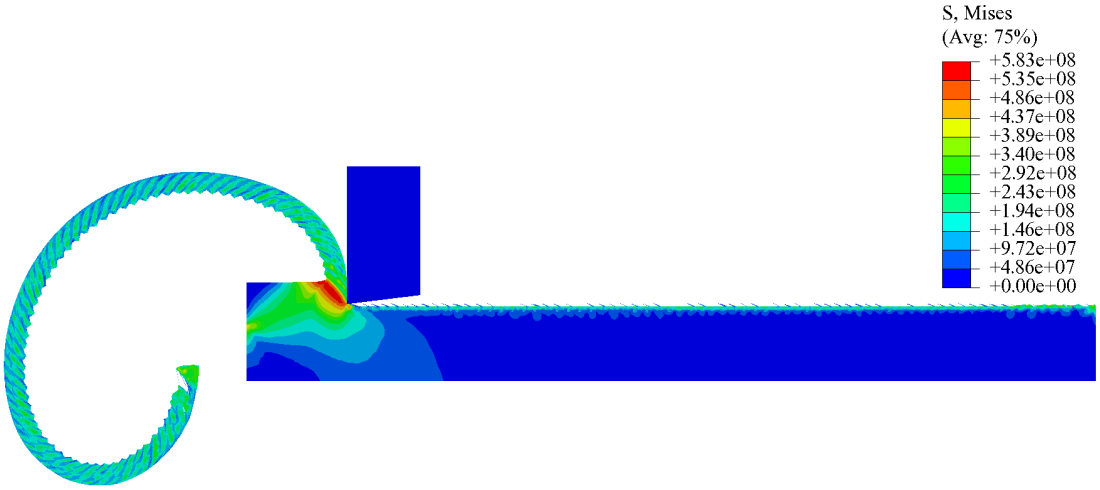

(b) equivalent stress results for uncut chip thickness $a_c = 0.3$ mm; $\alpha = 0°$; $V_c = 200$ m/min

(c) equivalent stress results for uncut chip thickness $a_c = 0.2$ mm; $\alpha = 0°$; $V_c = 200$ m/min

Figure 7.10: comparison of equivalent stress results obtained from FE simulation of orthogonal machining at various uncut chip thickness, a_c

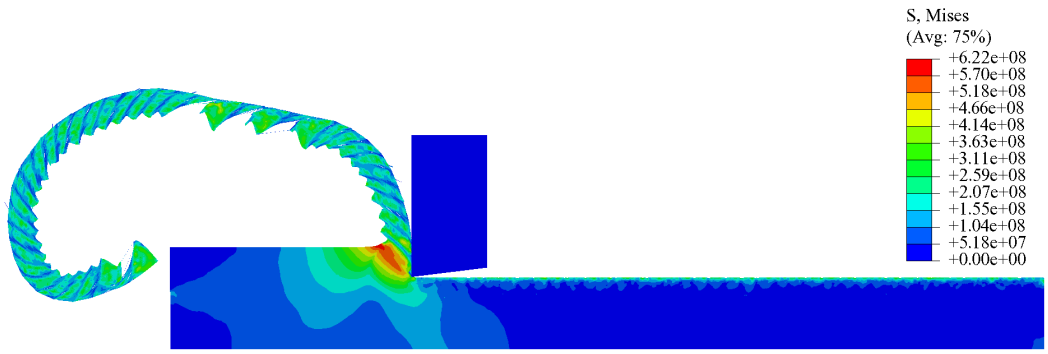

(a) Equivalent stress results for cutting speed $V_c = 200$ m/min; $\alpha = 0°$; $a_c = 0.4$ mm

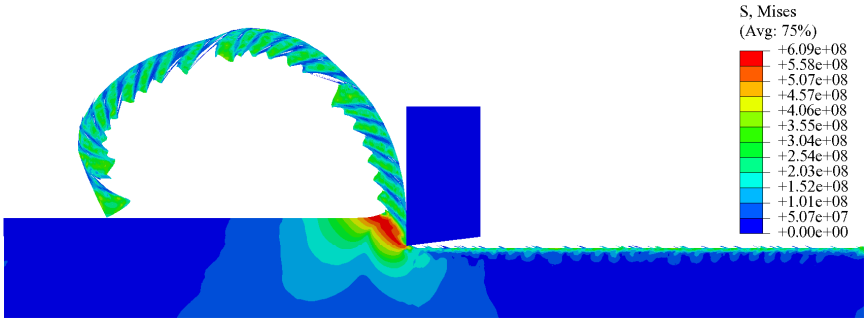

(b) Equivalent stress results for cutting speed $V_c = 400$ m/min; $\alpha = 0°$; $a_c = 0.4$ mm

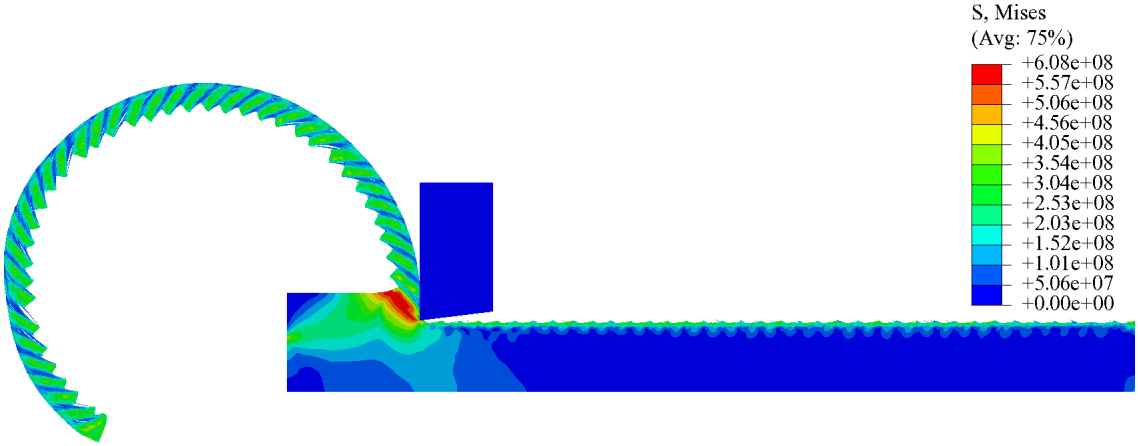

(c) Equivalent stress results for cutting speed $V_c = 800$ m/min; $\alpha = 0°$; $a_c = 0.4$ mm

Figure 7.11: comparison of equivalent stress results obtained from FE simulation of orthogonal machining at various cutting speed, V_c

When the cutting parameters are pushed towards extremities such as high uncut chip thickness a_c or low tool rake angles, there is an increase in normal stress $S11$, $S22$ and $S33$ at the chip free surface shown in fig. 7.12, fig. 7.13 and fig. 7.14

respectively. These normal stress components are tensile in nature near the crack tip (in shear band) and compressive around that region. Such a stress state instigates crack initiation and propagation from the chip free surface. The crack initiation in chip is also observed low cutting speeds when the tool rake angle α is low or negative and uncut chip thickness a_c is high.

These results are in agreement with and support the serrated chip formation based on mixed mode ductile fracture and adiabatic shear localization presented in [91].

The fig. 7.15, fig. 7.16, fig. 7.17 and fig. 7.18 compares stress range in primary and secondary shear zone for all cutting parameters considered in this work. The value of yield stress in primary shear zone is around 600 MPa which is in agreement with the stress - strain curves presented in section 3.4 for high strain rate and temperatures. However, for low uncut chip thickness such as $a_c = 0.2$ mm, the stress in primary shear zone is little below 600 MPa. The results indicate that when serrated chips are formed, the shear bands run through the entire chip thickness and the secondary shear zone is not exclusively formed. In other words, high stress values are observed in entire chip except for shear localized zones (shear bands). However, when continuous chips are formed, the stress in entire chip is uniform with formation of secondary shear zone exclusively. The value of stress in secondary shear zone is higher than the rest of chip because of high tool chip friction. In addition, the thickness of secondary shear zone increases in continuous chips with increase in friction.

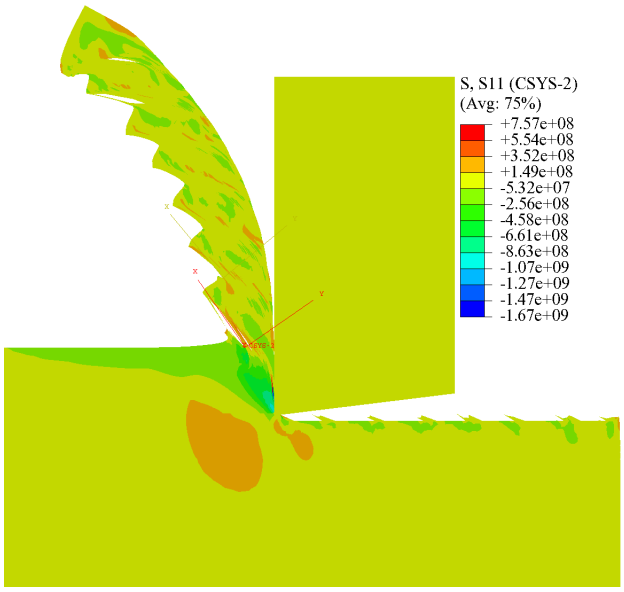

Figure 7.12: S11 normal stress at crack tip w.r.t CSYS-2 for cutting speed $V_c = 800$ m/min; $\alpha = 0°$; $a_c = 0.4$ mm

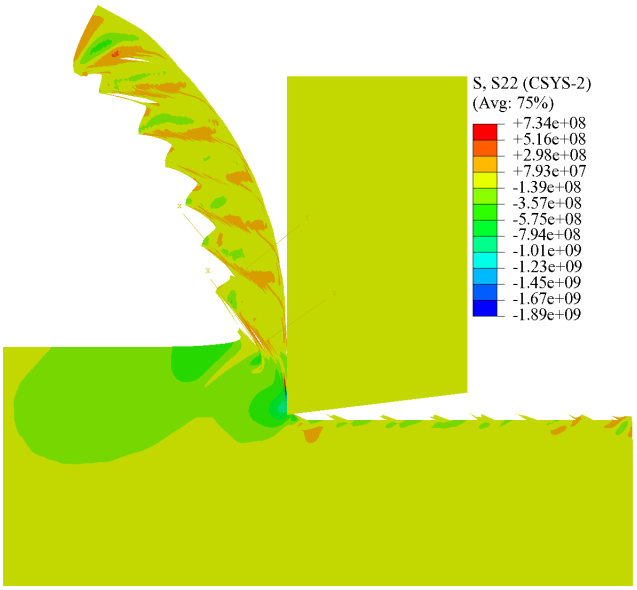

Figure 7.13: S22 normal stress at crack tip w.r.t CSYS-2 for cutting speed $V_c = 800$ m/min; $\alpha = 0°$; $a_c = 0.4$ mm

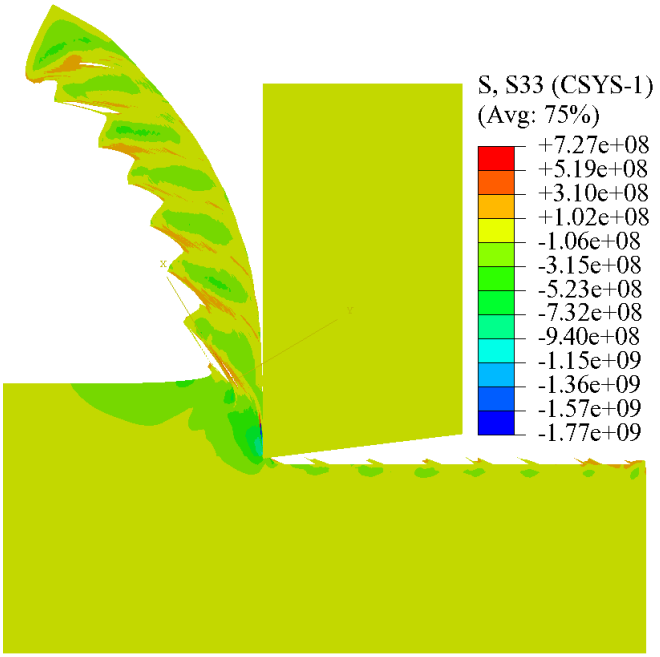

Figure 7.14: S33 normal stress at crack tip w.r.t CSYS-2 for cutting speed $V_c = 800$ m/min; $\alpha = 0°$; $a_c = 0.4$ mm

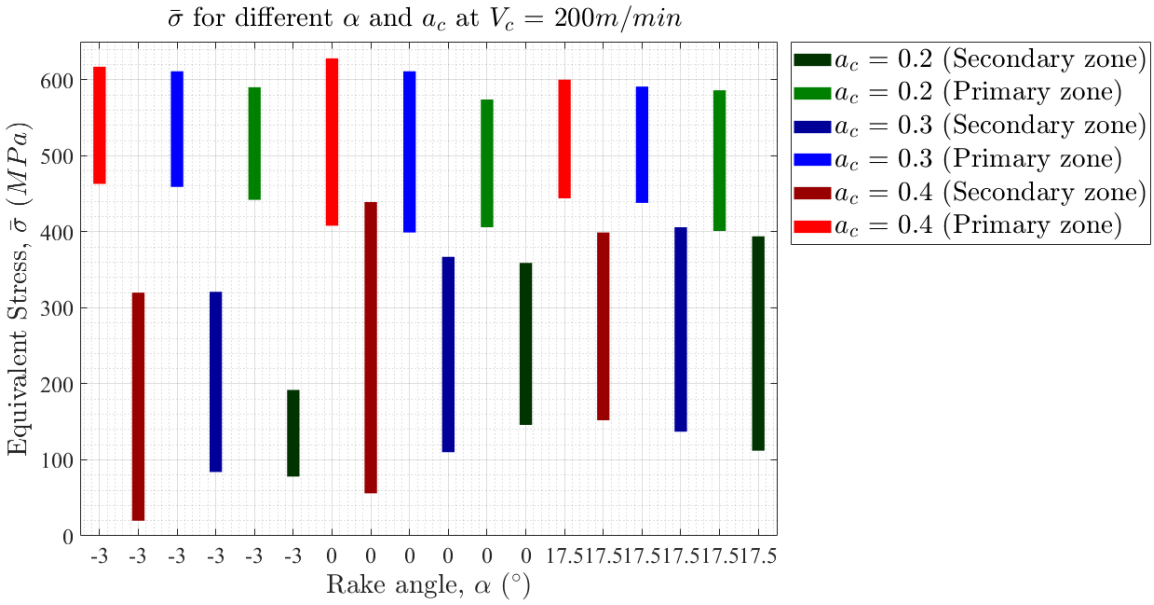

Figure 7.15: Equivalent stress results obtained from FE simulation of orthogonal machining at cutting speed $V_c = 200$ m/min and various values of α and a_c

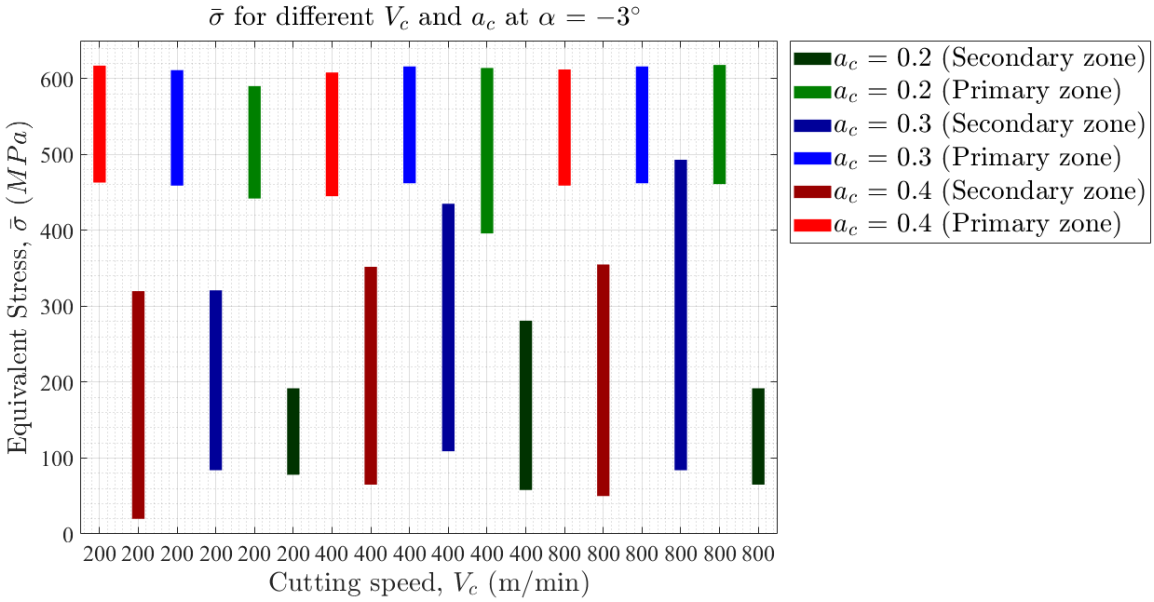

Figure 7.16: Equivalent stress results obtained from FE simulation of orthogonal machining with tool rake angle $\alpha = -3°$ and various values of a_c and V_c

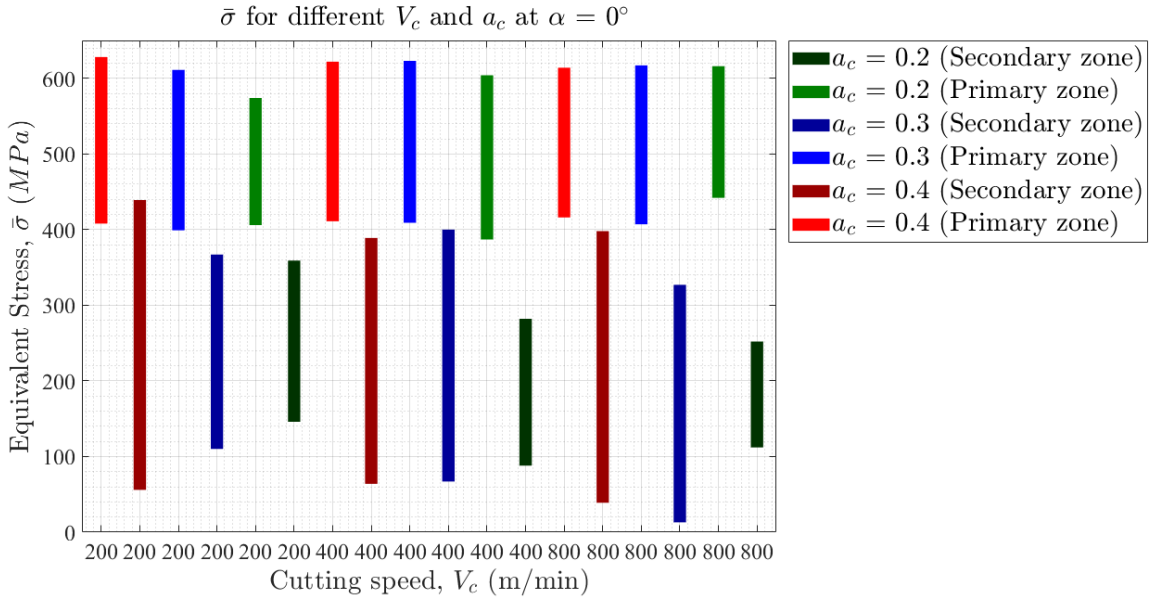

Figure 7.17: Equivalent stress results obtained from FE simulation of orthogonal machining with tool rake angle $\alpha = 0°$ and various values of a_c and V_c

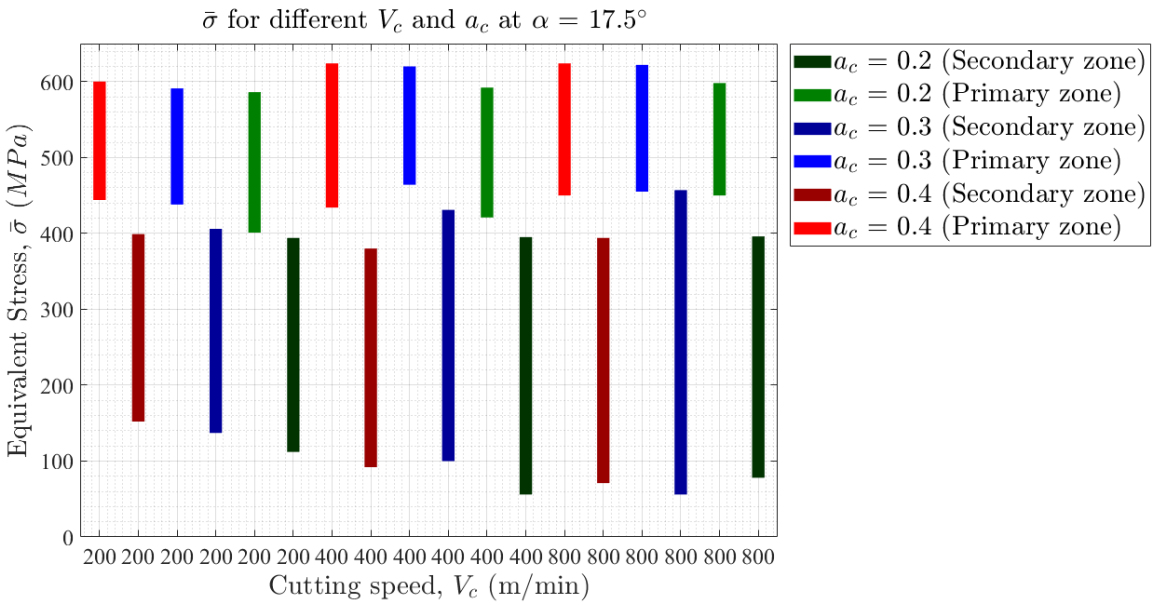

Figure 7.18: Equivalent stress results obtained from FE simulation of orthogonal machining with tool rake angle $\alpha = 17.5°$ and various values of a_c and V_c

7.4 Cutting force

The cutting force multiplied by tool displacement gives external work. This external work is dissipated in form of plastic work, frictional work and energy released to form new surfaces during chip formation and chip breakage. hence, it is very important to understand the cutting force requirement for machining with various cutting parameters. The fig. 7.19 and fig. 7.20 shows cutting force results obtained from orthogonal machining simulations of A2024-T251 at V_c = 200 m/min, α = 17.5°, a_c = 0.4 mm and at V_c = 200 m/min, α = 17.5°, a_c = 0.3 mm respectively. These results were captured as finite element output for every 1E-7 s. It should be noted that stable time increment in all simulations was of the order 1E-9 s. However, obtaining cutting force output at all time increments was computationally expensive. The average cutting force in fig. 7.19 is 943 N and it is 650 N in fig. 7.20. The chip shape obtained for the case with a_c = 0.4 (fig. 7.19) mm is serrated and hence it is observed that there is lot of oscillation in cutting force because of shear band formation resulting from shear localization. Whereas for the case with a_c = 0.3 mm (fig. 7.20) shows relatively less oscillation in cutting force as the chip shape is smooth and continuous.

Fig. 7.21, fig. 7.22 and fig. 7.23 shows comparison of average cutting force at various cutting speeds measured for machining simulations with all tool rake angles α and at all uncut chip thickness a_c considered in the parametric study. The results clearly indicates that the average cutting force requirement increases with increase in uncut chip thickness a_c as well as with decrease in tool rake angle α. Generally it is observed from the results that the required cutting force decreases slightly with increase in cutting speed V_c for machining simulation with a given tool rake angle α and uncut chip thickness a_c.

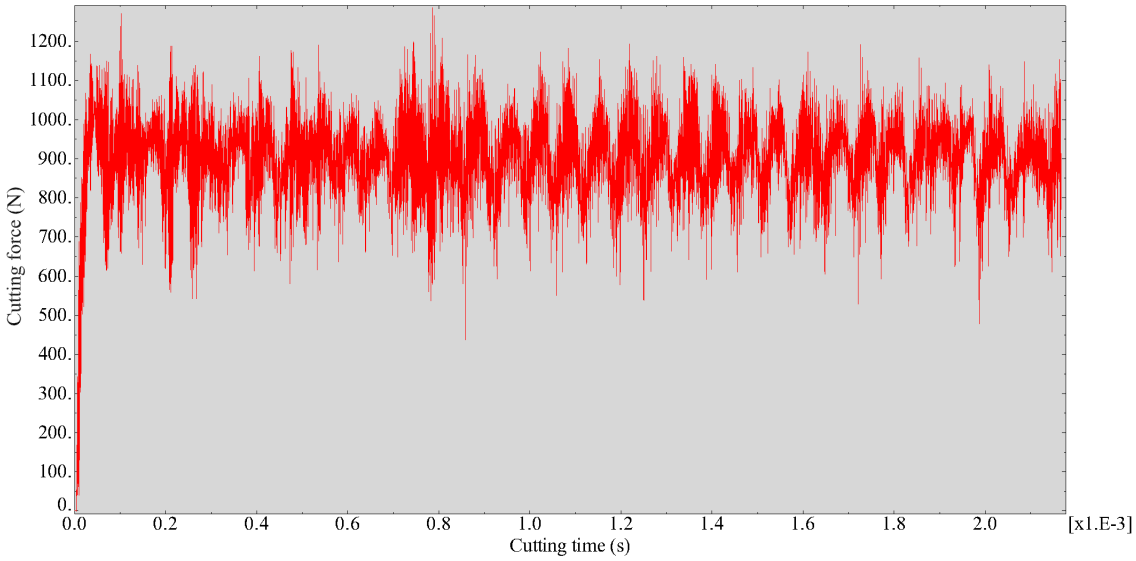

Figure 7.19: Cutting force results obtained from FE simulation of machining of A2024-T351 at $V_c = 200$ m/min, $\alpha = 17.5°$ and $a_c = 0.4$ mm

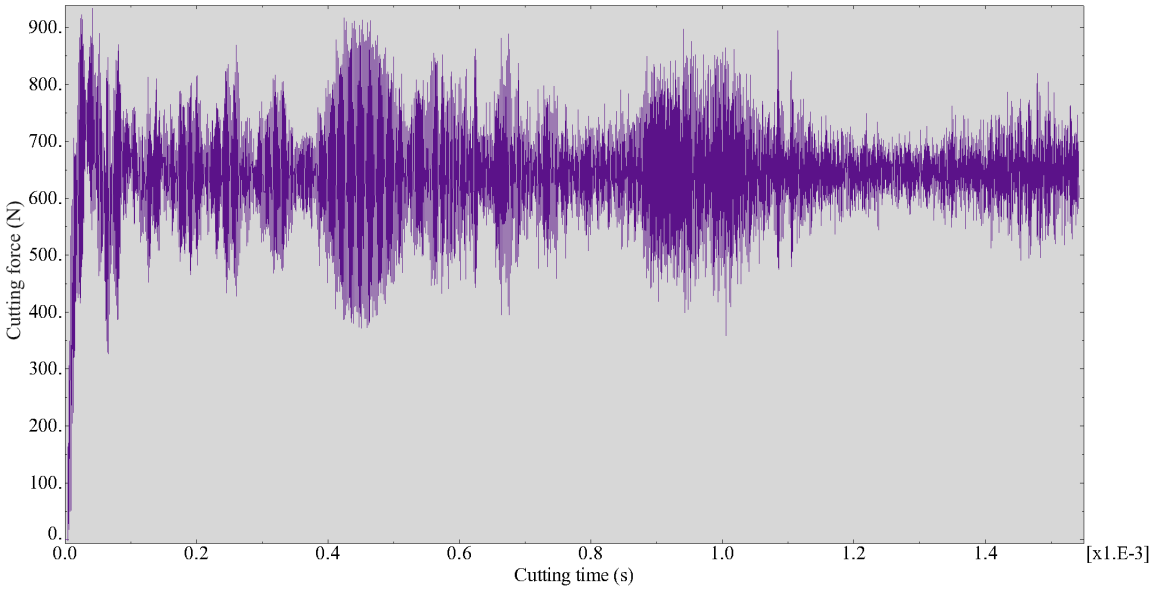

Figure 7.20: Cutting force results obtained from FE simulation of machining of A2024-T351 at $V_c = 200$ m/min, $\alpha = 17.5°$ and $a_c = 0.3$ mm

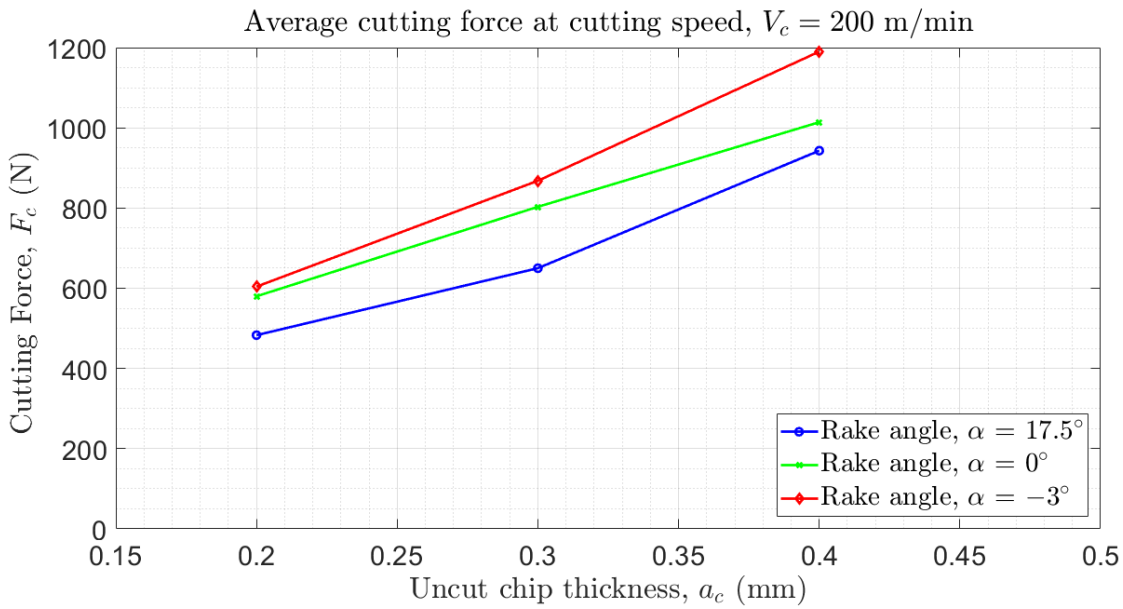

Figure 7.21: Average cutting force results obtained from FE simulation of orthogonal machining at cutting speed $V_c = 200$ m/min for various values of a_c and α

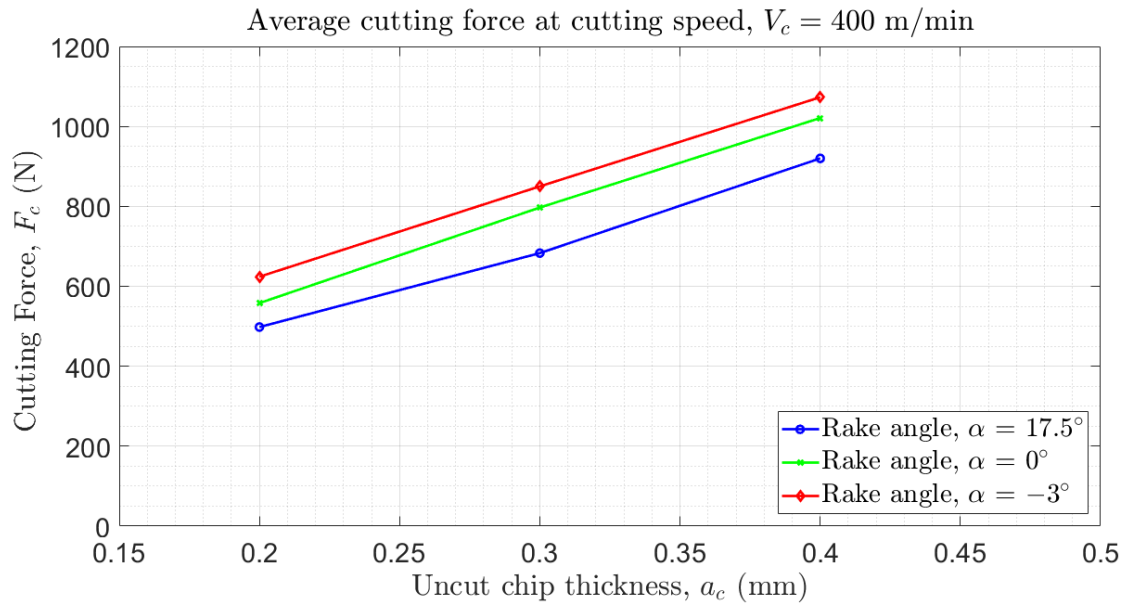

Figure 7.22: Average cutting force results obtained from FE simulation of orthogonal machining at cutting speed $V_c = 400$ m/min for various values of a_c and α

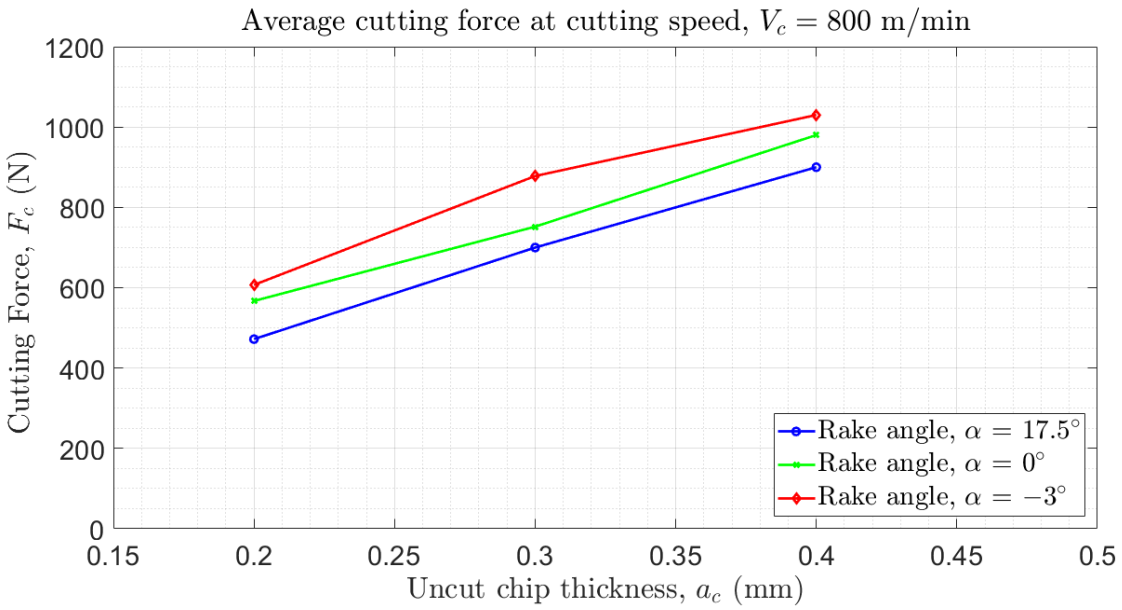

Figure 7.23: Average cutting force results obtained from FE simulation of orthogonal machining at cutting speed V_c = 800 m/min for various values of a_c and α

7.5 Temperature

In machining, two mechanisms that mainly contribute to rise in temperature are heat generated due to plastic work in primary shear zone and friction at tool-chip interface. Temperature results primarily depend on the cutting parameters used for machining along with the thermal properties of the tool and workpiece. In this section, the trends in temperature in primary and secondary shear zones are discussed.

The Fig. 7.24 shows temperature distribution in orthogonal machining of A2024 with tools having different rake angles. Other parameters such as uncut chip thickness and cutting speed are kept constant with their values equal to a_c = 0.4 mm and V_c = 800 m/min respectively.

The Fig. 7.24a shows results for orthogonal machining simulation with a tool of rake angle $\alpha = -3°$. The temperature range in primary shear zone is from 36°C to 261°C where as the temperature distribution range in secondary shear zone is from 250°C to 308°C.

Fig. 7.24b shows temperature distribution results from machining simulation with tool having rake angle $\alpha = 0°$. The temperature range in primary shear zone is from 32°C to 253°C where as in secondary shear zone it is from 245°C to 297°C.

The Fig. 7.24c shows temperature distribution obtained from machining simulation with a tool having rake angle $\alpha = 17.5°$. The temperature range in primary and secondary shear zone is from 28°C to 201°C and 180°C to 238°C respectively.

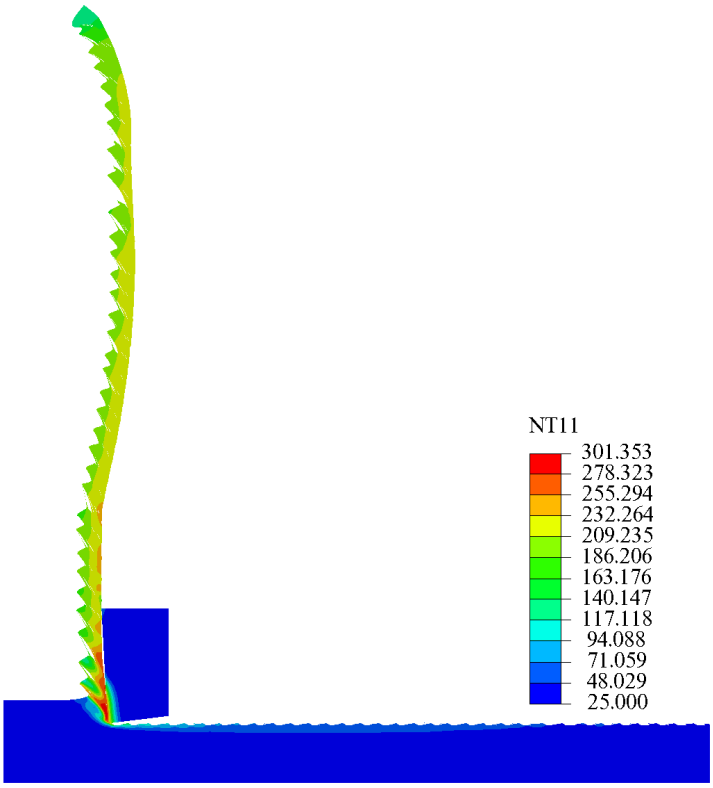

(a) Temperature distribution for rake angle $\alpha = -3°$; $a_c = 0.4$ mm; $V_c = 800$ m/min

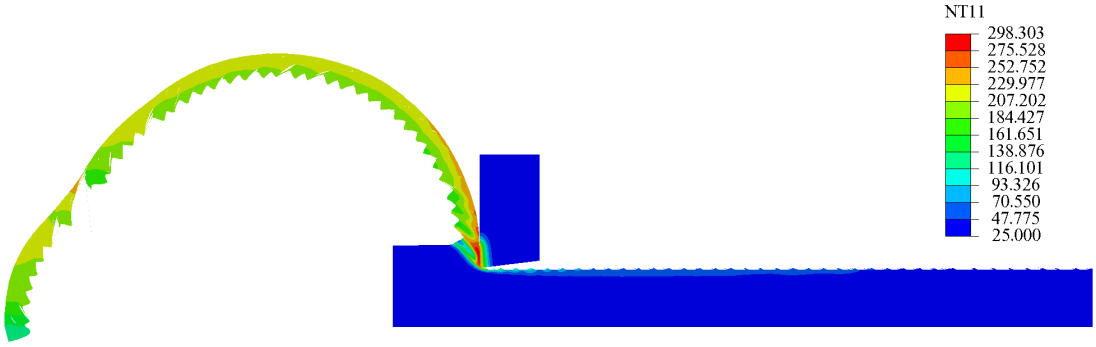

(b) Temperature distribution for rake angle $\alpha = 0°$; $a_c = 0.4$ mm; $V_c = 800$ m/min

(c) Temperature distribution for rake angle $\alpha = 17.5°$; $a_c = 0.4$ mm; $V_c = 800$ m/min

Figure 7.24: comparison of temperature distribution results obtained from FE simulation of orthogonal machining conducted using various tool rake angles, α

Figure 7.25 shows result for temperature distribution obtained from FE simulation conducted for machining at different uncut chip thickness, a_c. Other parameters such as tool rake angle and cutting velocity are kept unvaried and their values are $\alpha = 0°$ and $V_c = 400$ m/min respectively.

Figure 7.25a shows the temperature distribution results for $a_c = 0.4$ mm. The temperature range in primary and secondary shear zones is from 30°C to 229°C and 225°C to 269°C respectively.

Similarly the temperature range in primary and secondary shear zone for $a_c = 0.3$ mm as shown in fig. 7.25b is from 27°C to 217°C and 232°C to 262°C respectively.

The temperature range in primary and secondary shear zone for $a_c = 0.2$ as shown in fig. 7.25c is from 28°C to 211°C and 227°C to 249°C respectively.

It is observed from the results that the values of maximum temperature decreases in both primary and secondary shear zone with decrease in the value of uncut chip thickness, a_c. Such a trend is temperature results is observed in experimental results presented in literature.

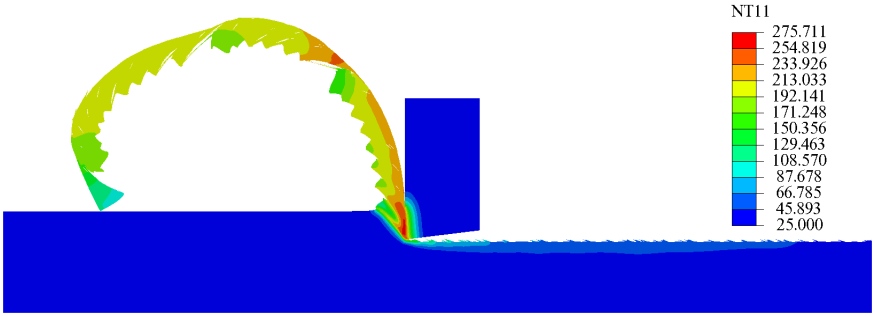

(a) Temperature distribution for uncut chip thickness $a_c = 0.4$ mm; $\alpha = 0°$; $V_c = 400$ m/min

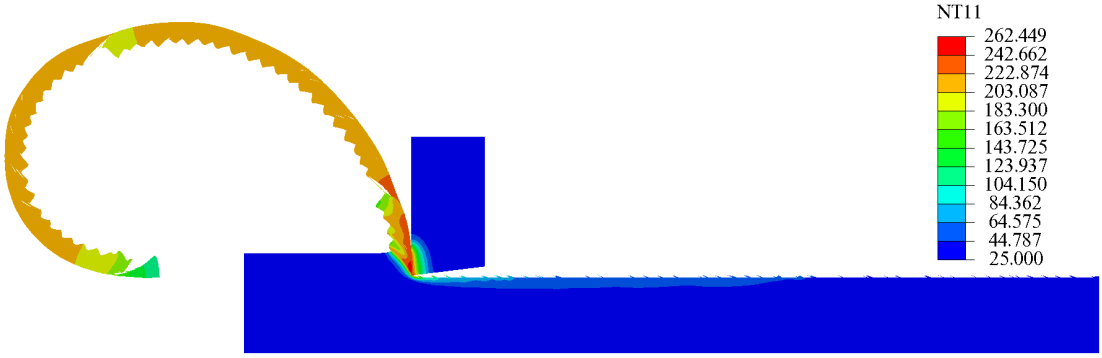

(b) Temperature distribution for uncut chip thickness $a_c = 0.3$ mm; $\alpha = 0°$; $V_c = 400$ m/min

(c) Temperature distribution for uncut chip thickness $a_c = 0.2$ mm; $\alpha = 0°$; $V_c = 400$ m/min

Figure 7.25: comparison of temperature distribution results obtained from FE simulation of orthogonal machining at various uncut chip thickness, a_c

The fig. 7.26 shows result for temperature distribution obtained from FE simulation conducted for machining at different cutting speed, V_c. Other parameters such as tool rake angle and uncut chip thickness are kept unvaried such that their values are $\alpha = -3°$ and $a_c = 0.2$ mm respectively. Fig. 7.26a are the temperature distribution results for $V_c = 800$ m/min. The temperature range in primary and secondary shear

zones is from 30°C to 236°C and 240°C to 274°C respectively.

Similarly the temperature range in primary and secondary shear zone for $V_c = 400$ m/min as shown in fig. 7.26b is from 33°C to 226°C and 231°C to 253°C respectively.

The temperature range in primary and secondary shear zone for $V_c = 200$ m/min as shown in fig. 7.26c is from 30°C to 210°C and 208°C to 227°C respectively.

These results indicate that the temperature in primary and secondary shear zone decreases with decrease in cutting speed for a given rake angle and uncut chip thickness. Such a trend in temperature distribution is consistent with experimental results presented in literature.

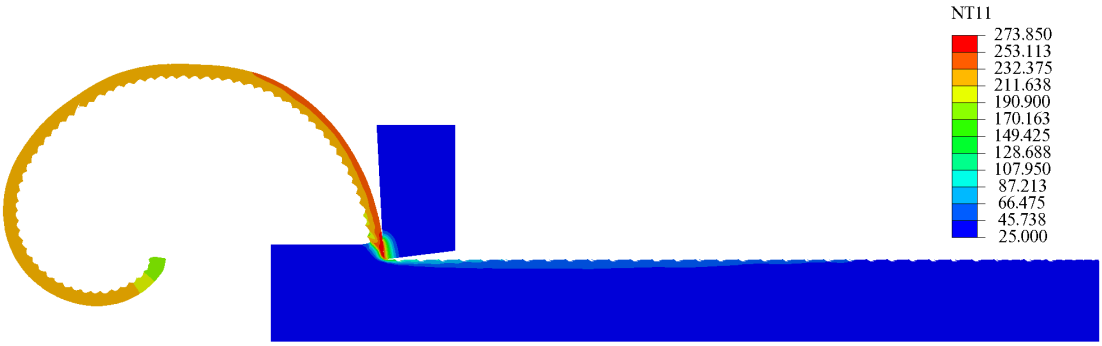

(a) Temperature distribution for cutting speed $V_c = 800$ m/min; $\alpha = -3°$; $a_c = 0.2$ mm

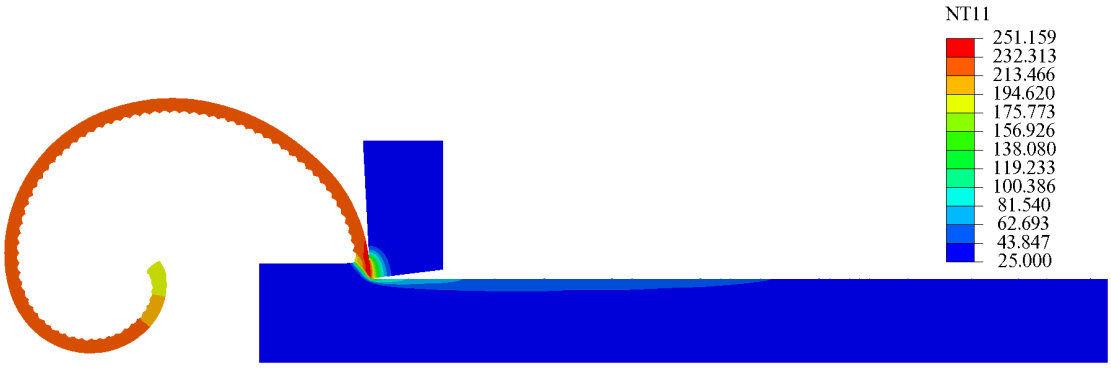

(b) Temperature distribution for cutting speed $V_c = 400$ m/min; $\alpha = -3°$; $a_c = 0.2$ mm

(c) Temperature distribution cutting speed $V_c = 200$ m/min; $\alpha = -3°$; $a_c = 0.2$ mm

Figure 7.26: comparison of temperature distribution results obtained from FE simulation of orthogonal machining at various cutting speed, V_c

The temperature rise in primary shear zone is mainly attributed to plastic work where as the temperature rise in secondary shear zone is mainly attributed to heat

generated due to friction. Temperature distribution in primary and secondary shear zone obtained from FE simulation of orthogonal machining of A2024 using tool rake angles $\alpha = -3°$, $\alpha = 0°$ and $\alpha = 17.5°$ are shown in fig. 7.28, fig. 7.29 and fig. 7.30 respectively. The results for temperature distribution in primary and secondary shear zone are plotted for various uncut chip thickness a_c and cutting speed V_c considered for parametric study in this work. The fig. 7.27 shows comparison of temperature in primary and secondary shear zone for all three rake angles, various uncut chip thickness and a fixed velocity $V_c = 800$ m/min.

The results indicate that the temperature rise in secondary shear zone for all the cases is higher than the temperature rise in primary shear zone. Unlike primary shear zone, the entire secondary shear zone is found to be in higher temperature range having a small difference between the minimum and maximum temperature. Moreover, although the maximum value for temperature is primary shear zone is limited to a very small zone near the tool tip, where material fracture occurs to separate chip from the bulk material. This indicates that, the maximum temperature in primary shear zone is also due to the fracture work. Most of the areas in primary shear zone remains in the mid zone temperature range for all the cases plotted in fig. 7.28, fig. 7.29, fig. 7.30 and fig. 7.27. Figures 7.31, 7.32 and 7.33 shows maximum temperature rise in primary shear zone for various cutting parameters. Thus, the temperature rise due friction at tool - chip interface is higher in machining as compared to the temperature rise in primary shear zone due to plastic work. Such a result is also consistent with experimental results presented in literature, for instance [104].

The parametric study indicates that in both primary and secondary shear zones, temperature increases with increase in cutting velocity V_c when all other cutting parameters are kept constant. Similar trend of increase in temperature is observed with increase in uncut chip thickness a_c with other parameters remaining unchanged. How-

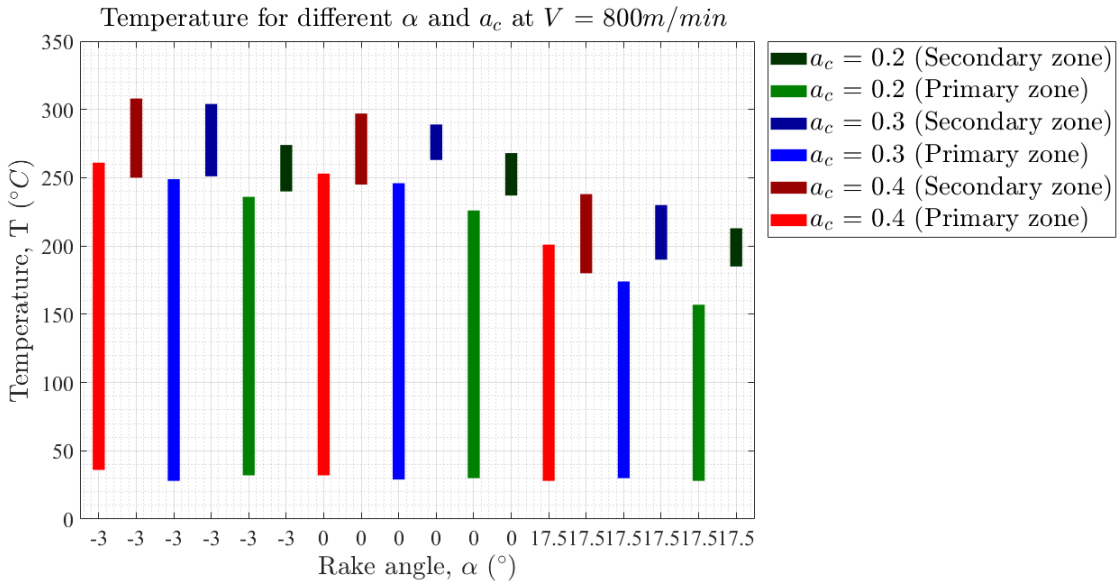

Figure 7.27: Temperature distribution results over entire FE simulation time for orthogonal machining at cutting speed V_c = 800 m/min and various values of α and a_c

ever, for same set of cutting parameters the temperature in primary and secondary shear zones reduces when tool rake angle is increased.

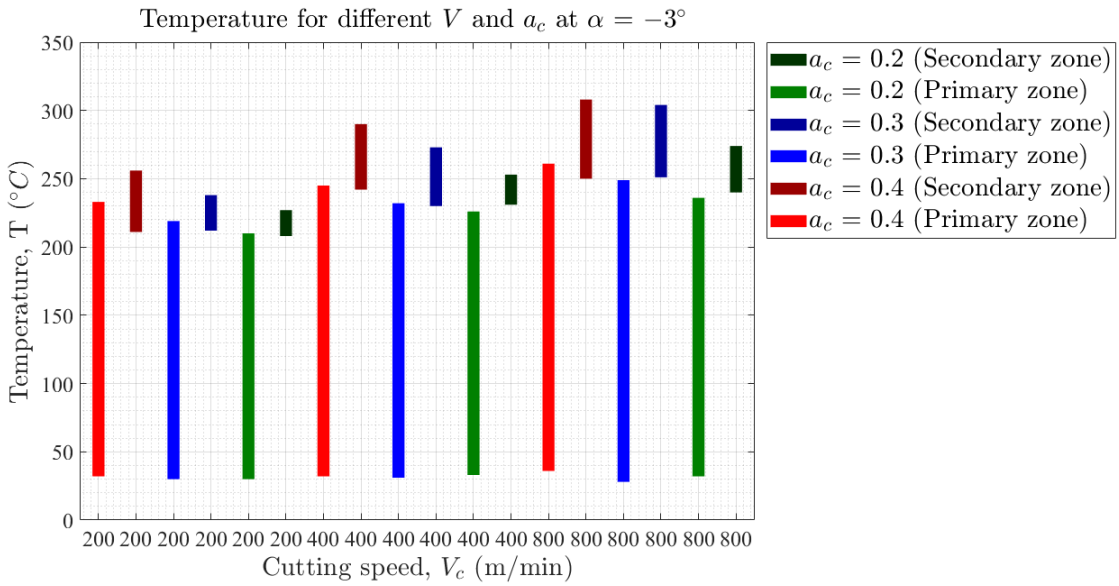

Figure 7.28: Temperature distribution results over entire FE simulation time for orthogonal machining with tool rake angle $\alpha = -3°$ and various values of a_c and V_c

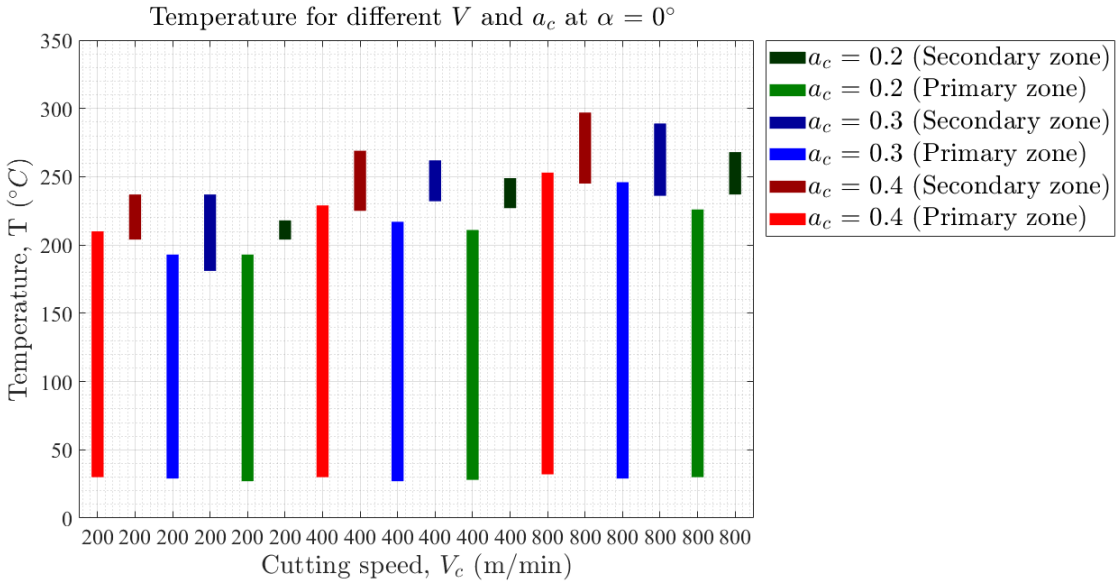

Figure 7.29: Temperature distribution results over entire FE simulation time for orthogonal machining with tool of rake angle $\alpha = 0°$ and various values of a_c and V_c

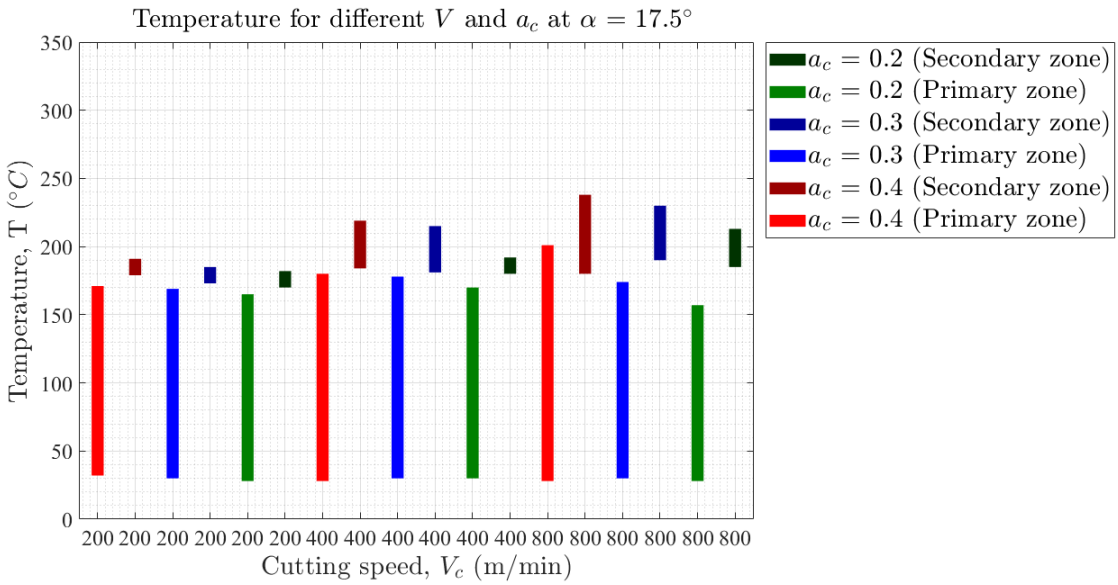

Figure 7.30: Temperature distribution results over entire FE simulation time for orthogonal machining with tool of rake angle $\alpha = 17.5°$ and various values of a_c and V_c

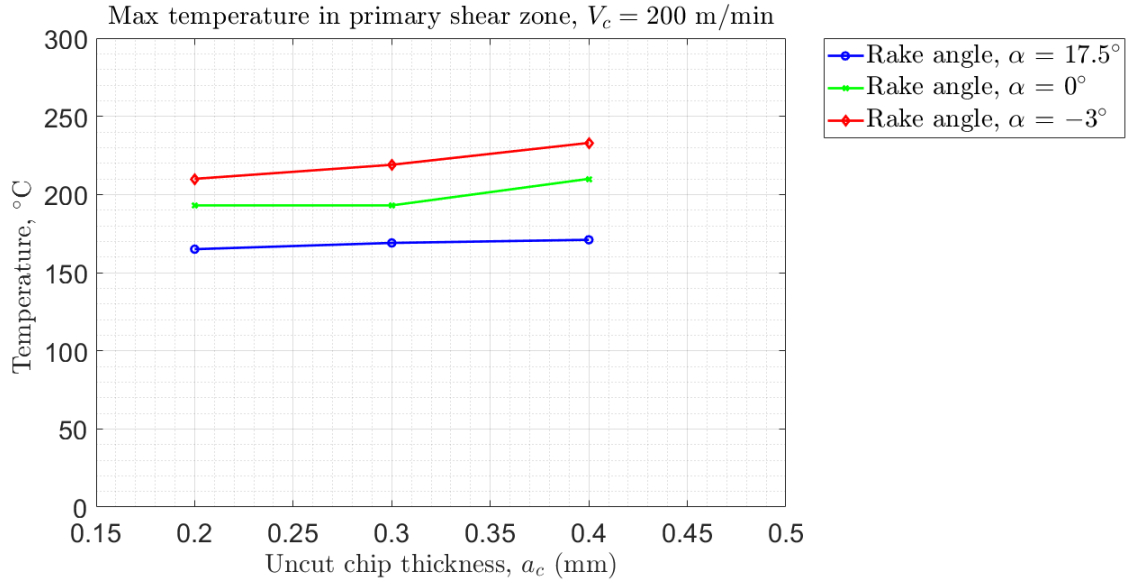

Figure 7.31: Maximum temperature in primary shear zone for different α and a_c at cutting speed $V_c = 200$

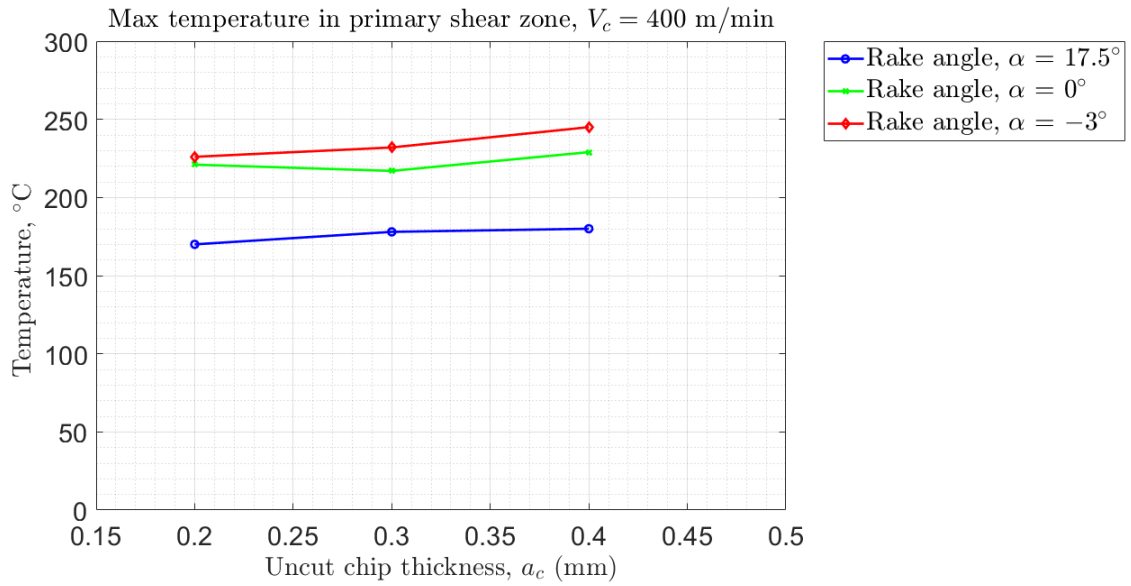

Figure 7.32: Maximum temperature in primary shear zone for different α and a_c at cutting speed $V_c = 200$

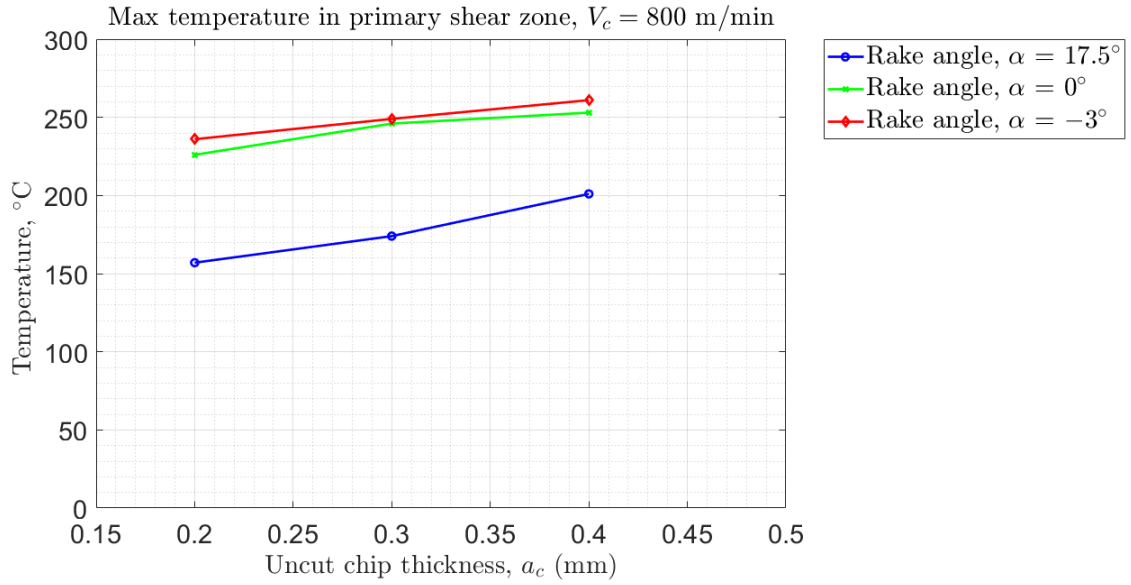

Figure 7.33: Maximum temperature in primary shear zone for different α and a_c at cutting speed $V_c = 200$

CHAPTER 8: CONCLUSIONS

8.1 Choice of fracture model and threshold value for G_f^{sep} and G_f^{serr}

The results presented in this work clearly show that the chip shape and other field variables are dependent on the choice of the damage evolution model used and the criteria used for chip separation and chip serration. An exponential damage model is shown to capture chip serration correctly whereas a linear damage model is shown to be appropriate for modeling chip separation. When linear damage evolution law is considered for both chip separation and serration, although chip formation is successfully simulated, the results were found to be considerably different from experimental results.

Another feature of the model is that the threshold values for chip separation and chip serration are based on the fracture toughness of the material. The values for G_f^{sep} can be determined directly from machining experiments so that its dependence on rate and thermal effects can be accounted for. In addition, since G_f^{sep} is independent of rake angle and cutting speeds (see [70] and [2] for experimental support), it can be readily measured with a minimal set of experiments. Unfortunately, although it is recognized in the recent machining literature that G_f^{serr} is different (and higher) than G_f^{sep} for steels and aluminum alloys, G_f^{serr} values are not readily available. For this reason, in the present work, we considered different threshold values for G_f^{serr} and studied it's effect on chip morphology and various other variables. The results indicate that the chip morphology is significantly affected by the threshold value for chip serration with higher values of G_f^{serr} leading to smoother chips. This result is supported by the fact that higher G_f^{serr} indicates high fracture toughness of chip and hence a continuous chip morphology is physically expected.

8.2 Stress, strain and chip morphology

The numerical results show that machining conditions that promote large deformation and high temperatures in primary shear zone lead to shear localization and promote serrated chip formation. With high $\bar{\epsilon}$ and low $\bar{\sigma}$, the tendency of the material to deform plastically increases which represents increase in ductility in the chips. This observation is consistent with the mechanism behind serrated chip formation as suggested in [98]. In addition, the results also indicate occasional crack initiation and propagation from the chip free surface under certain cutting conditions. Here, an increase in normal stresses in shear bands is observed such that the criterion for G_f^{serr} is satisfied to form new surfaces by chip breakage. These results are in agreement with and support the serrated chip formation based on mixed mode ductile fracture and adiabatic shear localization [91].

Continuous chips are formed with cutting conditions such that there is no shear localization or crack initiation. The equivalent plastic strain $\bar{\epsilon}$ is low in the entire chip. For A2024-T351, its value is less than 2 when continuous chips are formed. However, continuous chips may develop a secondary shear zone because of high friction at tool-chip interface. The thickness of this zone increases with increase in friction.

Serrated chips are observed under following cutting conditions:

1. High cutting speeds, V_c
2. Low tool rake angles, α
3. High uncut chip thickness, a_c

Continuous chips are observed under following cutting conditions:

1. Low cutting speeds, V_c
2. High tool rake angles, α

3. low uncut chip thickness, a_c

While the proposed approach appears to be promising, additional experiments and improvements to the existing theories to determine the critical values G_f for separation and serration are needed. The proposed approach can also be significantly improved by replacing the two separate damage evolution laws for chip separation and serration by a more sophisticated and unified damage evolution model that can accurately capture the physics of both the processes.

REFERENCES

[1] T. Hsu, "A study of the normal and shear stresses on a cutting tool," *Journal of engineering for industry*, vol. 88, no. 1, pp. 51–61, 1966.

[2] Y. Patel, B. Blackman, and J. Williams, "Measuring fracture toughness from machining tests," *Proceedings of the Institution of Mechanical Engineers, Part C: Journal of Mechanical Engineering Science*, vol. 223, no. 12, pp. 2861–2869, 2009.

[3] G. Ye, Y. Chen, S. Xue, and L. Dai, "Critical cutting speed for onset of serrated chip flow in high speed machining," *International Journal of Machine Tools and Manufacture*, vol. 86, pp. 18–33, 2014.

[4] M. Cocquilhat, "Experiences sur la résistance utile produite dans le forage," in *Annales des Travaux Publics en Belgique*, vol. 10, p. 199, 1851.

[5] I. Time, "Resistance of metals and wood to cutting," *St. Petersbourg, Russia: Dermacow Press House*, 1870.

[6] A. P. Markopoulos, *Finite element method in machining processes*. Springer Science & Business Media, 2012.

[7] M. H. Tresca, "On further applications of the flow of solids," *Proceedings of the Institution of Mechanical Engineers*, vol. 29, no. 1, pp. 301–345, 1878.

[8] K. Zvorykin, "On the force and energy necessary to separate the chip from the workpiece," *Vetnik Promyslennostie*, vol. 123, 1896.

[9] A. Mallock, "Vi. the action of cutting tools," *Proceedings of the Royal Society of London*, vol. 33, no. 216-219, pp. 127–139, 1882.

[10] V. Piispanen, "Theory of formation of metal chips," *Journal of Applied Physics*, vol. 19, no. 10, pp. 876–881, 1948.

[11] H. Ernst and M. E. Merchant, *Chip formation, friction and finish*. Cincinnati milling machine Company Cincinnati, 1941.

[12] M. E. Merchant, "Mechanics of the metal cutting process. i. orthogonal cutting and a type 2 chip," *Journal of applied physics*, vol. 16, no. 5, pp. 267–275, 1945.

[13] S. Kobayashi and E. Thomsen, "Metal-cutting analysisâii: New parameters," *Journal of Engineering for Industry*, vol. 84, no. 1, pp. 71–79, 1962.

[14] E. Lee and B. Shaffer, "The theory of plasticity applied to a problem of machining," *Journal of applied mechanics*, vol. 18, no. 4, pp. 405–413, 1951.

[15] N. N. Zorev, "Metal cutting mechanics," *PERGAMON, HEADINGTON HILL HALL, OXFORD, ENGLAND. 1966, 526 P*, 1966.

[16] W. Hastings, P. Oxley, and M. Stevenson, "Predicting a material's machining characteristics using flow stress properties obtained from high-speed compression tests," *Proceedings of the Institution of Mechanical Engineers*, vol. 188, no. 1, pp. 245–252, 1974.

[17] H. Kudo, "Some new slip-line solutions for two-dimensional steady-state machining," *International Journal of Mechanical Sciences*, vol. 7, no. 1, pp. 43–55, 1965.

[18] P. Dewhurst, "On the non-uniqueness of the machining process," in *Proc. R. Soc. Lond. A*, vol. 360, pp. 587–610, The Royal Society, 1978.

[19] P. Dewhurst and I. Collins, "A matrix technique for constructing slip-line field solutions to a class of plane strain plasticity problems," *International Journal for Numerical Methods in Engineering*, vol. 7, no. 3, pp. 357–378, 1973.

[20] P. L. B. Oxley and H.-T. Young, "The mechanics of machining: an analytical approach to assessing machinability," Chichester, England: Ellis Horwood Publisher, 1990.

[21] P. Oxley and M. Welsh, "Calculating the shear angle in orthogonal metal cutting from fundamental stress-strain-strain rate properties of the work material," 1964.

[22] E. Usui, A. Hirota, and M. Masuko, "Analytical prediction of three dimensional cutting processâpart 1: basic cutting model and energy approach," *Journal of Engineering for Industry*, vol. 100, no. 2, pp. 222–228, 1978.

[23] J. Mackerle, "Finite-element analysis and simulation of machining: a bibliography (1976–1996)," *Journal of Materials Processing Technology*, vol. 86, no. 1, pp. 17–44, 1999.

[24] J. Mackerle, "Finite element analysis and simulation of machining: an addendum: a bibliography (1996–2002)," *International Journal of Machine Tools and Manufacture*, vol. 43, no. 1, pp. 103–114, 2003.

[25] B. E. Klamecki, *Incipient Chip Formation in Metal Cutting–a Three-dimension Finite Element Analysis*. PhD thesis, University of Illinois at Urbana-Champaign, 1973.

[26] A. Tay, M. Stevenson, and G. de Vahl Davis, "Using the finite element method to determine temperature distributions in orthogonal machining," *Proceedings of the institution of mechanical engineers*, vol. 188, no. 1, pp. 627–638, 1974.

[27] T. Shirakashi and E. Usui, "Simulation analysis of orthogonal metal cutting mechanism," in *Proceedings of the International Conference on Production Engineering*, pp. 535–540, 1974.

[28] S. Akarca, X. Song, W. Altenhof, and A. Alpas, "Deformation behaviour of aluminium during machining: modelling by eulerian and smoothed-particle hydrodynamics methods," *Proceedings of the Institution of Mechanical Engineers, Part L: Journal of Materials: Design and Applications*, vol. 222, no. 3, pp. 209–221, 2008.

[29] J. S. Strenkowski and K.-J. Moon, "Finite element prediction of chip geometry and tool/workpiece temperature distributions in orthogonal metal cutting," *Journal of Engineering for Industry*, vol. 112, no. 4, pp. 313–318, 1990.

[30] J. S. Strenkowski and J. Carol, "An orthogonal metal cutting model based on an eulerian finite element method," in *Manufacturing Processes, Machines and Systems, Proceedings of the 13th NSF Conference on Production Research and Technology*, pp. 261–264, 1986.

[31] T. Childs and K. Maekawa, "Computer-aided simulation and experimental studies of chip flow and tool wear in the turning of low alloy steels by cemented carbide tools," *Wear*, vol. 139, no. 2, pp. 235–250, 1990.

[32] T. Belytschko, W. K. Liu, B. Moran, and K. Elkhodary, *Nonlinear finite elements for continua and structures*. John wiley & sons, 2013.

[33] A. J. Shih, "Finite element simulation of orthogonal metal cutting," *TRANSACTIONS-AMERICAN SOCIETY OF MECHANICAL ENGINEERS JOURNAL OF ENGINEERING FOR INDUSTRY*, vol. 117, pp. 84–84, 1995.

[34] T. Marusich and M. Ortiz, "Modelling and simulation of high-speed machining," *International Journal for Numerical Methods in Engineering*, vol. 38, no. 21, pp. 3675–3694, 1995.

[35] E. Usui and T. Shirakashi, "Mechanics of machiningâfrom descriptive to predictive theory," *On the Art of Cutting Metalsâ75 Years Later*, vol. 7, pp. 13–35, 1982.

[36] Z. Lin and S. Lin, "A coupled finite element model of thermo-elastic-plastic large deformation for orthogonal cutting," *Journal of Engineering Materials and Technology*, vol. 114, no. 2, pp. 218–226, 1992.

[37] J. S. Strenkowski and J. Carroll, "A finite element model of orthogonal metal cutting," *Journal of Engineering for Industry*, vol. 107, no. 4, pp. 349–354, 1985.

[38] K. Komvopoulos and S. Erpenbeck, "Finite element modeling of orthogonal metal cutting," *Journal of engineering for industry*, vol. 113, no. 3, pp. 253–267, 1991.

[39] K. Ueda and K. Manabe, "Rigid-plastic fem analysis of three-dimensional deformation field in chip formation process," *CIRP Annals-Manufacturing Technology*, vol. 42, no. 1, pp. 35–38, 1993.

[40] B. Zhang and A. Bagchi, "Finite element simulation of chip formation and comparison with machining experiment.," *ASME MATER DIV PUBL MD., ASME, NEW YORK, NY(USA), 1992,*, vol. 39, pp. 61–74, 1992.

[41] A. Shih, S. Chandrasekar, and H. Yang, "Finite element simulation of metal cutting process with strain-rate and temperatures effects," *Fundamental Issues in Machining, ASME, PED*, vol. 43, pp. 11–24, 1990.

[42] H. Sasahara, T. Obikawa, and T. Shirakashi, "The prediction of effects of cutting condition on mechanical characteristics in machined layer," in *Advancement of Intelligent Production*, pp. 473–478, Elsevier, 1994.

[43] E. Ceretti, P. Fallböhmer, W. Wu, and T. Altan, "Application of 2d fem to chip formation in orthogonal cutting," *Journal of Materials Processing Technology*, vol. 59, no. 1-2, pp. 169–180, 1996.

[44] L. Olovsson, L. Nilsson, and K. Simonsson, "An ale formulation for the solution of two-dimensional metal cutting problems," *Computers & structures*, vol. 72, no. 4, pp. 497–507, 1999.

[45] R. Rakotomalala, P. Joyot, and M. Touratier, "Arbitrary lagrangian-eulerian thermomechanical finite-element model of material cutting," *International Journal for Numerical Methods in Biomedical Engineering*, vol. 9, no. 12, pp. 975–987, 1993.

[46] M. Movahhedy, M. Gadala, and Y. Altintas, "Simulation of the orthogonal metal cutting process using an arbitrary lagrangian–eulerian finite-element method," *Journal of materials processing technology*, vol. 103, no. 2, pp. 267–275, 2000.

[47] T. Özel and E. Zeren, "Finite element method simulation of machining of aisi 1045 steel with a round edge cutting tool," in *Proceedings of the 8th CIRP International Workshop on Modeling of Machining Operations*, pp. 533–542, 2005.

[48] P. J. Arrazola *et al.*, "Investigations on the effects of friction modeling in finite element simulation of machining," *International Journal of Mechanical Sciences*, vol. 52, no. 1, pp. 31–42, 2010.

[49] M. C. Shaw and J. Cookson, *Metal cutting principles*, vol. 2. Oxford university press New York, 2005.

[50] Z.-C. Lin and W.-C. Pan, "A thermoelastic-plastic large deformation model for orthogonal cutting with tool flank wearâpart i: Computational procedures," *International journal of mechanical sciences*, vol. 35, no. 10, pp. 829–840, 1993.

[51] C. MacGregor and J. Fisher, "A velocity-modified temperature for the plastic flow of metals," *Journal of applied mechanics-transactions of the ASME*, vol. 13, no. 1, pp. A11–A16, 1946.

[52] T. Shirakashi, K. Maekawa, and E. Usui, "Flow stress of low carbon steel at high temperature and strain rate. i: Propriety of incremental strain method in impact compression test with rapid heating and cooling systems," *Bulletin of the Japan Society of Precision Engineering*, vol. 17, no. 3, pp. 161–166, 1983.

[53] E. Usui, K. Maekawa, and T. Shirakashi, "Simulation analysis of built-up edge formation in machining of low carbon steel.," *BULL. JAPAN SOC. PRECISION ENG.*, vol. 15, no. 4, pp. 237–242, 1981.

[54] F. J. Zerilli and R. W. Armstrong, "Dislocation-mechanics-based constitutive relations for material dynamics calculations," *Journal of Applied Physics*, vol. 61, no. 5, pp. 1816–1825, 1987.

[55] Y. Huang and S. Liang, "Cutting forces modeling considering the effect of tool thermal propertyâapplication to cbn hard turning," *International journal of machine tools and manufacture*, vol. 43, no. 3, pp. 307–315, 2003.

[56] A. H. Adibi-Sedeh, V. Madhavan, and B. Bahr, "Extension of oxley's analysis of machining to use different material models," *TRANSACTIONS-AMERICAN SOCIETY OF MECHANICAL ENGINEERS JOURNAL OF MANUFACTURING SCIENCE AND ENGINEERING*, vol. 125, no. 4, pp. 656–666, 2003.

[57] T. Özel and E. Zeren, "A methodology to determine work material flow stress and tool-chip interfacial friction properties by using analysis of machining," *Journal of manufacturing science and Engineering*, vol. 128, no. 1, pp. 119–129, 2006.

[58] Y. Karpat and T. Özel, "Predictive analytical and thermal modeling of orthogonal cutting processâpart i: predictions of tool forces, stresses, and temperature distributions," *Journal of manufacturing science and engineering*, vol. 128, no. 2, pp. 435–444, 2006.

[59] D. Umbrello, R. Mâsaoubi, and J. Outeiro, "The influence of johnson–cook material constants on finite element simulation of machining of aisi 316l steel," *International Journal of Machine Tools and Manufacture*, vol. 47, no. 3-4, pp. 462–470, 2007.

[60] J. Huang and J. Black, "An evaluation of chip separation criteria for the fem simulation of machining," *TRANSACTIONS-AMERICAN SOCIETY OF MECHANICAL ENGINEERS JOURNAL OF MANUFACTURING SCIENCE AND ENGINEERING*, vol. 118, pp. 545–554, 1996.

[61] L. Zhang, "On the separation criteria in the simulation of orthogonal metal cutting using the finite element method," *Journal of Materials Processing Technology*, vol. 89, pp. 273–278, 1999.

[62] B. Zhang and A. Bagchi, "Finite element simulation of chip formation and comparison with machining experiment," *Journal of engineering for industry*, vol. 116, no. 3, pp. 289–297, 1994.

[63] K. Iwata, K. Osakada, and Y. Terasaka, "Process modeling of orthogonal cutting by the rigid-plastic finite element method," *Journal of Engineering Materials and Technology*, vol. 106, no. 2, pp. 132–138, 1984.

[64] G. L. Mitchum, *A technique for predicting chip formation in orthogonal metal cutting using a Lagrangian finite element model.* PhD thesis, North Carolina State University, 1987.

[65] M. G. Cockcroft and D. J. Latham, *A simple criterion of fracture for ductile metals.* 1966.

[66] E. Ceretti, P. Fallboehmer, W. Wu, and T. Altan, "Simulation of high speed milling: application of 2d fem to chip formation in orthogonal cutting," *ERC NSM, Ohio State University*, 1995.

[67] E. Ceretti, M. Lucchi, and T. Altan, "Fem simulation of orthogonal cutting: serrated chip formation," *Journal of Materials Processing Technology*, vol. 95, no. 1, pp. 17–26, 1999.

[68] M. C. Shaw, "Metal cutting principles 3rd edition," 1957.

[69] A. Atkins, "Modelling metal cutting using modern ductile fracture mechanics: quantitative explanations for some longstanding problems," *International Journal of Mechanical Sciences*, vol. 45, no. 2, pp. 373–396, 2003.

[70] B. Wang, Z. Liu, and Q. Yang, "Investigations of yield stress, fracture toughness, and energy distribution in high speed orthogonal cutting," *International Journal of Machine Tools and Manufacture*, vol. 73, pp. 1–8, 2013.

[71] Y. Patel, B. Blackman, and J. Williams, "Determining fracture toughness from cutting tests on polymers," *Engineering Fracture Mechanics*, vol. 76, no. 18, pp. 2711–2730, 2009.

[72] M. H. Ali, M. Ansari, B. A. Khidhir, B. Mohamed, and A. Oshkour, "Simulation machining of titanium alloy (ti-6al-4v) based on the finite element modeling," *Journal of the Brazilian Society of Mechanical Sciences and Engineering*, vol. 36, no. 2, pp. 315–324, 2014.

[73] M. H Quinney, "The latent energy remaining in a metal after cold working," *Proc. R. Soc. Lond. A*, vol. 143, no. 849, pp. 307–326, 1934.

[74] N. Zorev, "Inter-relationship between shear processes occurring along tool face and shear plane in metal cutting," *International research in production engineering*, vol. 49, pp. 42–49, 1963.

[75] P. Wallace and G. Boothroyd, "Tool forces and tool-chip friction in orthogonal machining," *Journal of Mechanical Engineering Science*, vol. 6, no. 1, pp. 74–87, 1964.

[76] X. Yang and C. R. Liu, "A new stress-based model of friction behavior in machining and its significant impact on residual stresses computed by finite element method," *International Journal of Mechanical Sciences*, vol. 44, no. 4, pp. 703–723, 2002.

[77] H. Chandrasekaran and D. Kapoor, "Photoelastic analysis of tool-chip interface stresses," *Journal of Engineering for Industry*, vol. 87, no. 4, pp. 495–502, 1965.

[78] S. Kato, K. Yamaguchi, and M. Yamada, "Stress distribution at the interface between tool and chip in machining," *Journal of Engineering for Industry*, vol. 94, no. 2, pp. 683–689, 1972.

[79] P. S. Follansbee, "The hopkinson bar," *Metals handbook*, vol. 8, no. 9, pp. 198–217, 1985.

[80] M. LeBlanc and D. Lassila, "Dynamic tensile testing of sheet material using the split-hopkinson bar technique," *Experimental Techniques*, vol. 17, no. 1, pp. 37–42, 1993.

[81] X. Teng and T. Wierzbicki, "Evaluation of six fracture models in high velocity perforation," *Engineering Fracture Mechanics*, vol. 73, no. 12, pp. 1653–1678, 2006.

[82] T. Mabrouki, F. Girardin, M. Asad, and J.-F. Rigal, "Numerical and experimental study of dry cutting for an aeronautic aluminium alloy (a2024-t351)," *International Journal of Machine Tools and Manufacture*, vol. 48, no. 11, pp. 1187–1197, 2008.

[83] H. Li, M. Fu, J. Lu, and H. Yang, "Ductile fracture: experiments and computations," *International journal of plasticity*, vol. 27, no. 2, pp. 147–180, 2011.

[84] H. Hooputra, H. Gese, H. Dell, and H. Werner, "A comprehensive failure model for crashworthiness simulation of aluminium extrusions," *International Journal of Crashworthiness*, vol. 9, no. 5, pp. 449–464, 2004.

[85] Y. Bai and T. Wierzbicki, "A new model of metal plasticity and fracture with pressure and lode dependence," *International journal of plasticity*, vol. 24, no. 6, pp. 1071–1096, 2008.

[86] G. R. Johnson and W. H. Cook, "Fracture characteristics of three metals subjected to various strains, strain rates, temperatures and pressures," *Engineering fracture mechanics*, vol. 21, no. 1, pp. 31–48, 1985.

[87] *Abaqus documentation (2017)*, 2017.

[88] A. Hillerborg, M. Modéer, and P.-E. Petersson, "Analysis of crack formation and crack growth in concrete by means of fracture mechanics and finite elements," *Cement and concrete research*, vol. 6, no. 6, pp. 773–781, 1976.

[89] A. Atkins, "Toughness and cutting: a new way of simultaneously determining ductile fracture toughness and strength," *Engineering fracture mechanics*, vol. 72, no. 6, pp. 849–860, 2005.

[90] J. Williams, Y. Patel, and B. Blackman, "A fracture mechanics analysis of cutting and machining," *Engineering Fracture Mechanics*, vol. 77, no. 2, pp. 293–308, 2010.

[91] B. Wang and Z. Liu, "Serrated chip formation mechanism based on mixed mode of ductile fracture and adiabatic shear," *Proceedings of the Institution of Mechanical Engineers, Part B: Journal of Engineering Manufacture*, vol. 228, no. 2, pp. 181–190, 2014.

[92] G. Williams, Y. Patel, and B. R. Blackman, "An analysis of cutting and machining using fracture mechanics concepts," in *ECF17, Brno 2008*, 2013.

[93] S. Kobayashi, R. Herzog, D. Eggleston, and E. Thomsen, "A critical comparison of metal-cutting theories with new experimental data," *Journal of Engineering for Industry*, vol. 82, no. 4, pp. 333–347, 1960.

[94] R. W. Ivester and M. Kennedy, *Comparison of machining simulations for 1045 steel to experimental measurements*. Society of Manufacturing Engineers, 2000.

[95] D. Eggleston, R. Herzog, and E. Thomsen, "Observations on the angle relationships in metal cutting," *ASME Journal of Engineering for Industry*, vol. 81, pp. 263–279, 1959.

[96] Y. Karpat, "Investigation of the effect of cutting tool edge radius on material separation due to ductile fracture in machining," *International Journal of Mechanical Sciences*, vol. 51, no. 7, pp. 541–546, 2009.

[97] N. Cook, I. Finnie, and M. Shaw, "Discontinuous chip formation," *Trans. ASME*, vol. 76, no. 2, p. 153, 1954.

[98] G. Liyao, W. Minjie, and D. Chunzheng, "On adiabatic shear localized fracture during serrated chip evolution in high speed machining of hardened aisi 1045 steel," *International Journal of Mechanical Sciences*, vol. 75, pp. 288–298, 2013.

[99] M. Asad, F. Girardin, T. Mabrouki, and J.-F. Rigal, "Dry cutting study of an aluminium alloy (a2024-t351): a numerical and experimental approach," *International Journal of Material Forming*, vol. 1, no. 1, pp. 499–502, 2008.

[100] M. Madaj and M. Píška, "On the sph orthogonal cutting simulation of a2024-t351 alloy," *Procedia CIRP*, vol. 8, pp. 152–157, 2013.

[101] M. Daoud, W. Jomaa, J. Chatelain, and A. Bouzid, "A machining-based methodology to identify material constitutive law for finite element simulation," *The International Journal of Advanced Manufacturing Technology*, vol. 77, no. 9-12, pp. 2019–2033, 2015.

[102] S. Atlati, B. Haddag, M. Nouari, and M. Zenasni, "Analysis of a new segmentation intensity ratio âsirâ to characterize the chip segmentation process in machining ductile metals," *International Journal of Machine Tools and Manufacture*, vol. 51, no. 9, pp. 687–700, 2011.

[103] D. Stephenson, T.-C. Jen, and A. Lavine, "Cutting tool temperatures in contour turning: transient analysis and experimental verification," *Journal of Manufacturing Science and Engineering*, vol. 119, no. 4A, pp. 494–501, 1997.

[104] G. Chen, C. Ren, P. Zhang, K. Cui, and Y. Li, "Measurement and finite element simulation of micro-cutting temperatures of tool tip and workpiece," *International Journal of Machine Tools and Manufacture*, vol. 75, pp. 16–26, 2013.